ABSTRACT

Title of Dissertation: URBAN HEAT PROJECTIONS AND ADAPTATIONS IN A CHANGING CLIMATE: WASHINGTON D.C. AS A CASE STUDY

Yating Zhang, Doctor of Philosophy, 2019

Dissertation directed by: Professor Bilal M. Ayyub
Department of Civil and Environmental Engineering

Carbon emission from human activities has changed the Earth's overall climate and intensified extreme weather and climate events. Climate risks are regionally uneven due to different vulnerability levels of populations, infrastructures, and natural resources. Assessing local-scale risk is important in supporting climate preparation, adaptation planning, and policy development for cities to overcome climate change.

This dissertation developed the Asynchronous Regional Regression Model (ARRM) that statistically downscales data of Coupled Model Intercomparison Project Phase Five (CIMP5) into locations of observing stations, employed the Weather Research and Forecasting (WRF) model that dynamically downscales data of Community Earth System Model version one (CESM1) into fine-grid results, and proposed a framework to assess adaptation strategies for vulnerable infrastructure systems incorporating the probabilistic risk approach. Based on those models and methods, this dissertation projected the trend and level of the urban heat island (UHI) effect and heat waves in the rest of the 21st century for Washington D.C. and its surrounding areas, evaluated mitigation options for heat waves, and assessed adaptation strategies for electrical power systems in such area.

Projections based on the higher greenhouse gas (GHG) concentration scenario, Representative Concentration Pathway (RCP) 8.5, indicate a growing trend of heat waves at Washington D.C. in the rest of the century. The amplitude of heat waves may grow by 5.7°C, and frequency and duration may increase by more than twofold by the end of the century. The UHI effect may increase in summer and decrease in winter. The lower scenario, RCP 2.6, leads to slight decay of heat waves after a half-century of increase, and a minor change in the UHI effect.

Five heat wave mitigation strategies based on cool roofs, green roofs, and reflective pavements were evaluated in three future time periods. Results indicated that applying cool roofs and green roofs in the city scale can effectively reduce heat wave amplitude and duration, whereas the effectiveness of reflective pavements is negligible. However, reflective pavements can be more cost-effective than green roofs because of their low initial and maintenance costs.

Electrical power systems are particularly vulnerable to extreme heat. Results indicated that power outage risk caused by temperature rise may increase seventyfold

in the Washington metro area by the end of the century. If summer peak load on the electrical grid is cut by three quarters, there would be a twentyfold increase instead. This reduction is achievable by installing solar panels on building roofs, which can add an average generation capacity of 13.02 GW to the existing power system. Increasing the use of rooftop photovoltaics (PV) can increase the level of benefits.

URBAN HEAT PROJECTIONS AND ADAPTATIONS IN A CHANGING CLIMATE: WASHINGTON D.C. AS A CASE STUDY

by

Yating Zhang

Dissertation submitted to the Faculty of the Graduate School of the
University of Maryland, College Park, in partial fulfillment
of the requirements for the degree of
Doctor of Philosophy
2019

Advisory Committee:
  Professor Bilal M. Ayyub, Chair/Advisor
  Associate Professor Brian M. Philips
  Associate Professor Qingbin Cui
  Assistant Professor Michelle Bensi
  Professor Michael Kearney

Acknowledgements

Throughout the writing of this dissertation, I have received a great deal of support and assistance. I would like to express my gratitude to everyone who provided help and suggestions.

I would first like to thank my advisor, Dr. Ayyub, for his continuous guidance and advice these years. Thank you for providing the opportunities and resources for me to develop teaching, communication, organization, and project management skills. I am very grateful for his patience and persistence in teaching me how to design a research study and how to write a scientific paper.

I am eternally grateful to my committee members, Dr. Philips, Dr. Forman, Dr. Cui, Dr. Bensi, and Dr. Kearney for their advice and criticism.

I also thank my colleagues, Yanjie Zhang, Huiling Hu, Yalda Saadat, and Sally Saleem for their help and encouragement.

Finally, I would like to thank my parents and my husband. They are always being the person I could turn to during those dark and desperate years.

Table of Contents

List of Tables

List of Figures

List of Abbreviations

AOGCM	Coupled atmosphere-ocean general circulation model
ARRM	Asynchronous Regional Regression Model
CESM	Community Earth System Model
CDF	Cumulative distribution function
CMIP	Coupled Model Intercomparison Project
GCM	Global climate model
GHG	Greenhouse gas
LSM	Land surface model
NLCD	National land cover database
PV	Photovoltaics
RCM	Regional climate model
RCP	Representative concentration pathway
TX90p	The percentage of calendar days in which the maximum temperature exceeds the 90th percentile
TN90p	The percentage of calendar days in which the minimum temperature exceeds the 90th percentile
UCM	Urban canopy model
UHI	Urban heat island
WRF	Weather research and forecasting (model)
WSDI	Warm spell duration index

Chapter 1: Introduction

1.1 Climate change

1.1.1 Definition of climate change

Carbon emission from human activities has changed the Earth’s overall climate and intensified extreme weather and climate events (IPCC 2013). Many of the observed changes are unprecedented over decades to millennia since the 1950s, including warmed atmosphere and ocean, diminished snow and ice, risen sea level, and increased concentration of greenhouse gasses (IPCC 2013). Carbon dioxide concentration has increased by 40% since the pre-industrial times, which is primarily attributable to fossil fuel combustion and secondarily to land use change (IPCC 2013). Other greenhouse gases such as methane and nitrous oxide have augmented to levels unprecedented in the last 800,000 years (IPCC 2013). Increased greenhouse gases absorb and re-radiate extra Sun’s energy that is originally reflected back to space, heating the atmosphere and the Earth’s surface.

Climate change is defined as:

> A change in the state of the climate that can be identified (*e.g.*, by using statistical test) by changes in the mean and/or the variability of its properties, and that persists for an extended period, typically decades or longer. Climate change may be due to natural internal processes or external forcings such as

> modulations of the solar cycles, volcanic eruptions and persistent anthropogenic changes in the composition of the atmosphere or in land use (IPCC 1990).

The United Nations Framework Convention on Climate Change (UNFCCC) defines *climate change* as:

> A change of climate which is attributed directly or indirectly to human activity that alters the composition of the global atmosphere and which is in addition to natural climate variability observed over comparable time periods (United Nations 1992).

The major difference between the two definitions is that the Intergovernmental Panel on Climate Change (IPCC) considers natural and anthropogenic impacts on the change of climate, while UNFCCC accounts for human’s contribution alone to such change. However, the four concentration trajectories adopted by IPCC ignore natural factors (*e.g.*, volcano eruption) and focus on anthropogenic influence on future climate change (IPCC 2013). Therefore, IPCC and UNFCCC are consistent in projecting and evaluating climate change and its impacts.

1.1.2 Impacts of climate change

- **Temperature changes**

The global combined land and ocean surface temperature grew by 0.85°C on average over the last 140 years (IPCC 2013). The last three decades, 1983–2012, are likely the warmest 30-year period over the last 1,400 years for the North Hemisphere (IPCC 2013). The annual average temperatures across the contiguous United States have risen by 1°C since the beginning of the 20th century, and additional increment of 2.8–4.8°C is expected by the end of the 21st century (USGCRP 2017).

- **Precipitation changes**

The change in precipitation is seasonally and regionally different. The annual average precipitation across the United States has increased by 4% over the period of 1901–2015 (USGCRP 2017). Precipitation increases largest in fall (10%), then in spring and summer (3.5%), and little change was observed in winter at the national level (USGCRP 2017). The Northeast, Midwest, and Great Plains regions experience increased precipitation, whereas Southwest and Southeast regions suffer from decreased precipitation (USGCRP 2017).

- **Sea level rise**

Sea level rise is driven by ice melting from mountain glaciers and the Antarctic and Greenland ice sheets, and by thermal expansion of ocean because rising temperature raises the volume of seawater. In addition, the change in global land-water storage (*e.g.*, dams, reservoirs, groundwater, inland seas, wetlands) slightly affects the total amount of ocean water. From the year 1901–2010, global mean sea level rose by 0.19 m at an average rate of 1.7 mm/year (IPCC 2013). The rate of sea level rise increased to 2.0 mm/year during 1971–2010, and 3.2 mm/year during 1993–2010 (IPCC 2013).

- **Others**

The increase of temperature accelerates evapotranspiration, resulting in drier soils and fewer runoffs in the long run. The change in precipitation pattern may lead to increased drought in dry regions and intensified floods in wet regions. Climate change also propels ocean acidification, alters land use, and affects the ecosystem in a variety of ways (IPCC 2013; USGCRP 2017; USGCRP 2018).

1.1.3 Methods to study climate change

- **Energy balance models (1950s)**

Energy balance models are the earliest and most basic numerical climate models, which simulate the balance between the energy entering the Earth's atmosphere from the sun and the energy released back to space. The surface temperature of the Earth is the only variable considered in those models.

- **Radiative convective models (1960s – 1970s)**

Later researchers developed radiative-convective models by incorporating the vertical dimension (air convection) into energy balance models. These models can simulate energy transfer through the height of the atmosphere and calculate the temperature and humidity of different layers of the atmosphere.

- **General circulation models/Global climate models (1970s – 1980s)**

The biggest challenge associated with general circulation models is high computation demand. Early general circulation models are designed to characterize the evolution of the dynamic and thermodynamic state of atmosphere or ocean. They can capture air and water flows and heat transfer in the atmosphere and oceans. Latterly, atmosphere and ocean models are coupled and named the coupled atmosphere-ocean general circulation models (AOGCMs). They are able to simulate the exchange of heat and water between the land, atmosphere, and ocean.

- **Earth system models (1990s – present)**

More complicated treatments of sea ice and land surface are then included into AOGCMs, along with sub-models of vegetation, ecosystems, and biogeochemical cycles (National Research Council of the National Academies 2012). These formed the Earth system model, which can simulate the carbon cycle, nitrogen cycle, atmospheric chemistry, ocean ecology, and changes in vegetation and land use. Earth system models greatly improve the understanding of how climate responses to increased greenhouse gas emission.

- **Regional climate models (2000s – present)**

Regional climate models (RCMs) do similar work as global climate models/general circulation models (GCMs) but for a limited area of the Earth. Compared to GCMs, RCMs run more quickly and generate higher resolution results. RCMs (*e.g.*, Weather Research and Forecasting model) can also be used to downscale global climate information to a local scale.

- **Integrated assessment models (2010s – present)**

Integrated assessment models incorporate socioeconomic factors (*e.g.,* population, economic growth, energy use) into climate models, which allow projecting future greenhouse gas emissions, and evaluating policy options that could be deployed to tackle the emission problem. Six integrated assessment models have been developed so far to predict the impacts of climate change on the future world under five socioeconomic development pathways (Riahi *et al*. 2017).

1.1.4 Current status of climate change studies

- **Climate projection**

The coupled model intercomparison project

There are roughly 30 research groups that have developed their own climate models. These models are similar in the structure but different in details, such as physical schemes and the number of vertical layers. To enable comparison between the results of different models, the Coupled Model Intercomparison Project (CMIP) set up those models in the same way and used the same inputs. The Coupled Model

Intercomparison Project Phase Five (CMIP5) was published in the fifth IPCC climate change assessment report (IPCC 2013; IPCC 2014), incorporating the latest and most sophisticated climate model experiments worldwide (Wuebbles *et al.* 2014; Taylor *et al.* 2012). Compared to a single AOGCM, a multiple model ensemble has shown superior performance for historical climate assessment (Pierce *et al.* 2009), because coupling these models can take advantages of their strengths and compensate limitations. Compared to the previous model ensemble CMIP3, CMIP5 model ensemble has an increased spatial resolution, improved parametrizations, and additional trajectories for future assumptions, facilitating simulations for regional climate and projections under complicated future uncertainties (Sheffield *et al.* 2013a; Sheffield *et al.* 2013b; Taylor *et al.* 2012). The latest Coupled Model Intercomparison Project, CMIP6, is on the way and will form the basis of the sixth IPCC assessment report to be released in 2020 (Eyring *et al*. 2016).

Weighted and unweighted multiple model ensemble

The CMIP5 archive contains simulations of 29 institutions and 62 models. Some of the models are similar to the others because they share the same physical schemes and numerical methods. The fifth climate assessment of IPCC (IPCC 2013) and the third national climate assessment (USGCRP 2014) considered each model to be equally likely in depicting future climate change, whereas the fourth national climate assessment (USGCRP 2017) adopted a weighting strategy to coupling models based on their skills and independence. Sanderson *et al.* (2017) indicated that the overall performance of the weighted model ensemble can be better than that of model democracy, especially when selected models are significantly independent of each other. However, there is a tradeoff between model skills and model uniqueness, which may weaken the performance of weighted models. Model skills determine if the simulation is of sufficient accuracy, while model uniqueness ensures that uncertainties and bias are small enough. It should be noted that the weighting varies for varied regions because the capacity of models is different in simulating the climate of different geographical regions.

Representative Concentration Pathways

The inputs for CMIP5 standard model 'r1i1p1' include $NO/NO_2/NH_3$ emissions caused by deposition and fertilization in croplands, anthropogenic land use change, interactive carbon-nitrogen cycling, carbon-nitrogen dynamics, and CH_4 emissions on peatlands (Stocker *et al.* 2013). Four trajectories are devised to address the future uncertainties regarding emissions and concentrations of greenhouse gasses, aerosols, land change, and solar radiations (IPCC 2013). The four trajectories are Representative Concentration Pathways (RCP) 2.6, RCP 4.5, RCP 6.0, and RCP 8.5, corresponding to radiative forcing of 2.6, 4.5, 6.5, and 8.5 W/m^2 by 2100, respectively (IPCC 2013). *Radiative forcing* is defined as the net change in the energy balance of the Earth system because of natural and anthropogenic substances and processes, relative to the reference year of 1750 (IPCC 2013). The four trajectories assume CO_2 concentrations of 421, 538, 670, and 936 ppm by 2100, and greenhouse gas concentrations (CO_2, CH_4, N_2O) of 475, 630, 880, and 1313 ppm by 2100, respectively (IPCC 2013).

Downscaling techniques

Climate change impacts regions and populations unevenly, dependent on geographical, socioeconomic, and technological conditions. Assessing local-scale climate impacts requires high-resolution climate data, and therefore downscaling techniques were utilized to generate local detailed information based on global coarse simulation. ***Downscaling*** **is a procedure to take information known at large scales to make a prediction at local scales.** The dynamical downscaling technique uses the data of GCMs as initial and lateral boundaries of the outermost domain and employs RCMs to calculate climate conditions of nested domains. The nested domains have a much higher resolution compared to parent domains. Increasing the number of nested domains can improve the grid resolution of simulation exponentially. The statistical downscaling technique utilizes statistical approaches to adjust information of GCM to local results, including the use of mean bias correction, mean and variance bias correction, and quantile methods.

- **Climate mitigation and adaptation**

Climate change mitigation intends to reduce greenhouse gas emission and concentration in the atmosphere. Climate change adaptation means to take appropriate action to prevent and minimize damages and to take advantages of opportunities created by such change.

Paris Agreement

The Paris Agreement took effect in 2016 and brought all nations into a common cause to prevent the rise of global temperatures this century above 2°C relative to pre-industrial levels, and to make further efforts to limit the temperature increase to 1.5°C (UNFCCC 2016). The Paris Agreement has acted as a signal to the world that it is time for strong climate actions, and a large number of governments, businesses, and individuals have joined the movement.

Climate plans of Washington D.C.

Washington D.C. including its surrounding suburbs is rated the sixth-largest metropolitan area in the United States with an estimate of six million residents (Census 2019). The local government has started to evaluate and address climate impacts on its community since 2013. The *Sustainable DC Plan* published in 2013 set a goal to reduce 50% and 80% of greenhouse gas emissions in the district by 2032 and 2050 respectively, relative to the emission level of 2006 (DOEE 2013). To achieve this goal, the government made following plans: retrofitting 100% of existing commercial and multi-family buildings to meet requirements of net-zero energy standards; deploying the highest standards of green building design to new construction projects; improving energy efficiency and reducing overall consumption by 50%; increasing the share of renewable energy in energy supply to 50%; increasing the use of public transit to 50% of all commuter trips; and increasing biking and walking to 25% of all commuter trips.

The adaptation plan *Climate Ready DC* released in 2016 highlighted the needs to improve the resilience of energy, water, communication, transportation, and other critical infrastructure systems in response to climate change (DOEE 2016). The plan involves 77 actions/subactions in improving transportation and utility infrastructure to maintain variability during extreme weather events (*e.g.*, heat waves, severe storm, flooding); upgrading existing buildings and designing new buildings and development projects to withstand climate change impacts; strengthening community, social, and economic resilience to make neighborhoods and communities safer and more prepared; and establishing the policies, structures, and monitoring and evaluation procedures to ensure successful implementation of adaptation plans.

The climate and energy plan *Clean Energy DC* published in 2018 adjusted the climate goal to 100% reduction of greenhouse gas emission by 2050 (DOEE 2018). This adjustment shows increased ambition of local governments in mitigating climate change, and rising importance and urgency in doing so. The plan proposed to implementing net-zero energy building code for new construction, retrofitting existing buildings to improve their energy efficiency and reduce their reliance on fossil fuels for heating and cooling, developing renewable portfolio standard in order to steadily increase the use of renewable energy, increasing electricity generation and optimize energy distribution system, and reducing dependence on private vehicles and deploy zero-emission electric vehicles.

1.2 The urban heat island effect

1.2.1 Definition of the urban heat island effect

The urban heat island (UHI) effect describes the phenomenon whereby metropolitan areas are significantly warmer than their surroundings (EPA 2016; Santamouris 2015; Kolokotroni *et al.* 2012). The UHI effect is attributable to the rapid growth of population and large-scale replacement of vegetation with roads and buildings. Asphalt and concrete as building materials absorb more solar radiation and release more sensible heat to the atmosphere compared to the vegetation. Moreover, waste heat from human activities, such as vehicles, factories, and air conditioners, adds warmth to the surrounding environment. The global warming effect due to increased GHG concentration further exacerbates thermal comfort in urban communities (Kenward et al. 2014).

1.2.2 Impacts of the urban heat island effect

The UHI effect has a very significant impact on human life: increasing cooling energy consumption (Konopacki and Akbari 2002), deteriorating comfort levels, increasing pollution concentration (Ebi *et al.* 2008; Leung and Gustafson 2005), threatening human health (Tan *et al.* 2010; Kenward *et al.* 2014), and affecting urban economy.

1.2.3 Methods to project the urban heat island effect

Analyzing the future trend of the UHI effect requires projecting temperatures of urban and rural areas. The following methods were widely used in literature to predict temperatures.

- **Trend extrapolation**

The trend extrapolation method assumes that the recent trend is likely to continue in the future. Trends are sensitive to the choice and length of records and instrument used in the measurement (Wilby *et al.* 2009). If data are of good quality and enough length (*e.g.*, 30 years), it may be valid to extrapolate the trend for up to a decade. Extrapolation is unreliable beyond one decade because of many uncertainties associated with future conditions, such as land use change.

- **Raw GCM or RCM data analysis**

Raw GCM and RCM data can be employed directly to analyze the future trend of climate variables. The data have a coarse spatial resolution, and the grid space may range between 100–500 km. Raw GCM and RCM data are often biased compared to observed data, and therefore bias correction is required before use.

- **Weather generators**

Weather generators use precipitation as the primary variable to estimate other meteorological variables, which is called secondary variables, including maximum and minimum temperature, sunshine or cloudiness, vapor pressure and wind speed

(Kilsby *et al*. 2007). The relationships between secondary variables and daily precipitation are characterized by a range of regression functions, and the relationships are assumed to be constant over time. The performance of weather generators in reproducing observation is dependent on the accuracy in simulating precipitation and the relationship between precipitation and other variables. Most weather generators have been developed to software packages for easy access, such as WGEN (Richardson and Wright 1984), EARWIG (Kilsby *et al*. 2007), LARS-WG (Semenov 2012), and MarkSim GCM (Jones and Thornton 2013).

- **Dynamical downscaling**

The dynamical downscaling method uses RCMs to adjust coarse-grid simulations of GCM to fine-grid results that are suitable for local climate study. RCMs use data provided by GCMs as initial and lateral boundaries and generate results for nested domain based on the solutions of the parent domain. The grid resolution of the nested domain is several times of the present domain. Increasing the number of nested domains can exponentially improve the resolution of simulation. The limitation of dynamical downscaling method is that systematic bias in GCMs and RCMs can degrade the accuracy of climate simulation. This can be solved by removing the bias of GCM data prior to downscaling and correcting the bias of downscaling results using statistical methods.

- **Statistical downscaling**

Compared to dynamical methods, statistical methods are inexpensive computing and easy to use and apply (Chen *et al.* 2012). Statistical methods assume the relationship between the model simulation and observation is stationary, and hence the relationship derived from the historical period can be applied to projecting future conditions (Stoner *et al.* 2013). However, the real relationship can change slightly over time, which may weaken the accuracy of future projections (Barsugli *et al.* 2013). The statistical downscaling technique includes the use of Pseudo method, mean bias correction, quantile method, and bias correction for multiple model ensemble.

Pseudo method

The Pseudo method uses simulated mean climate change between the future and historical periods to represent the potential change of a climate variable as follows:

$$OB_F = OB_H + (\overline{GCM_F} - \overline{GCM_H}) \tag{1.1}$$

where OB_F is the projected observation. OB_H is the historical observation. $\overline{GCM_F}$ is averaged projection of a global climate model. $\overline{GCM_H}$ is averaged historical simulation of a global climate model. The average can be over a day or over a month dependent on data availability. Observations and model simulations should be of the same variable.

Mean bias correction

This method removes the mean bias of model simulation over the historical period assuming that the mean bias does not change over time, which is written as follows:

$$OB_F = GCM_F - (\overline{GCM_H} - \overline{OB_H}) \tag{1.2}$$

where $\overline{OB_H}$ is averaged historical observation. The average can be over a day or over a month dependent on data availability. Observations and model simulations should be of the same variable.

Quantile method

Assuming the quantile relationship between historical observation and simulation is time-invariant, model projected distribution can be corrected using this quantile relationship. The correction alters the probability distribution function (PDF) of model projection and removes all model biases including mean and variance biases. However, this method fails to retain the intervariable dependencies and introduces additional bias in the spatial gradient of variables. In contrast, mean bias correction can retain first-order spatial and intervariable dependencies (White and Toumi 2013).

Bias correction for multiple model ensemble

Assuming the bias of a model ensemble (*e.g.*, CMIP5) does not change over time, the bias of model projection can be removed by subtracting the mean difference between historical simulation ($\overline{GCM_{EH}}$) and observation ($\overline{OB_H}$). Model ensemble cancels out the internal variability of coupled models, resulting in underestimation of variability and extreme climate conditions. To mitigate this defect, an anomaly portion is added to the projection (Equation 1.4). The anomaly portion is derived from one selected model (GCM_F^*) and is calculated as the difference between future weather (*e.g.*, hourly, daily) and averaged future weather over a period (*e.g.*, several months or years).

$$OB_F = \overline{GCM_{EF}} - (\overline{GCM_{EH}} - \overline{OB_H}) + GCM_F^* \tag{1.3}$$

$$GCM_F^* = GCM_F - \overline{GCM_F} \tag{1.4}$$

It is worth noting that the anomaly portion derived from a selected model (GCM_F^*) still contains variance biases. Moreover, such linear adjustment (Equation 1.3) may cause inconsistence between different climate variables (*e.g.*, temperature, humidity, wind) because they are nonlinearly related. Dai *et al*. (2017) indicated that the inconsistency is small and hardly impacts results in the downscaled fields away from the lateral boundaries.

- **Weather classification**

Weather classification methods include analog analysis, cluster analysis, artificial neural network, and self-organizing map (Cavazos 2000; Yin 2011). These methods group historical simulations into several clusters, and link historical observations with the most similar simulation clusters. Future projections generated by GCMs are used as local predictions according to their clusters. Since these methods cannot predict new values that are outside the range of the historical record, a large amount of observation data is required (*e.g.,* 30 years daily data) in order to evaluate all possible weather conditions.

1.2.4 Current status of urban heat island studies

- **Observation and projection**

The fourth national assessment (USGCRP 2018) reported that U.S. cities are now 0.5–4.0 °C warmer during the day and 1.0–2.5 °C warmer at night compared to rural areas. Kenward *et al*. (2014) analyzed summer average temperature of 60 U.S. cities during 2004–2013 and ranked them based on the urban heat island (UHI) intensity, which is measured as the temperature difference between urban and nearby rural areas. Figure 1.1 presents the UHI intensity ranking of 60 U.S. cities, and Figure 1.2 shows the change rate of UHI intensity in the last decade. Cities tended to be warmer than the other places, and the maximum difference appeared in Las Vegas with a magnitude of 4°C/7.3°F (Figure 1.1). In addition, most of the cities suffered from strengthened UHI effect, whereas several cities experienced declined UHI intensity due to the rapid growth of rural areas (Figure 1.2). Kenward *et al*. (2014) attributed the increase of the UHI effect in most cities to climate change. In contrast, Scott *et al.* (2018) analyzed summer temperatures of 54 U.S. cities during 2000–2015 and found that the UHI intensity decreased as temperature rose. They also argued that cities did not experience increased UHI effect, and climate change did not exacerbate the UHI effect. One possible reason for their contradictory finding is that the urbanization of rural areas reduced the temperature difference between city and surrounding areas (Scott *et al.* 2018).

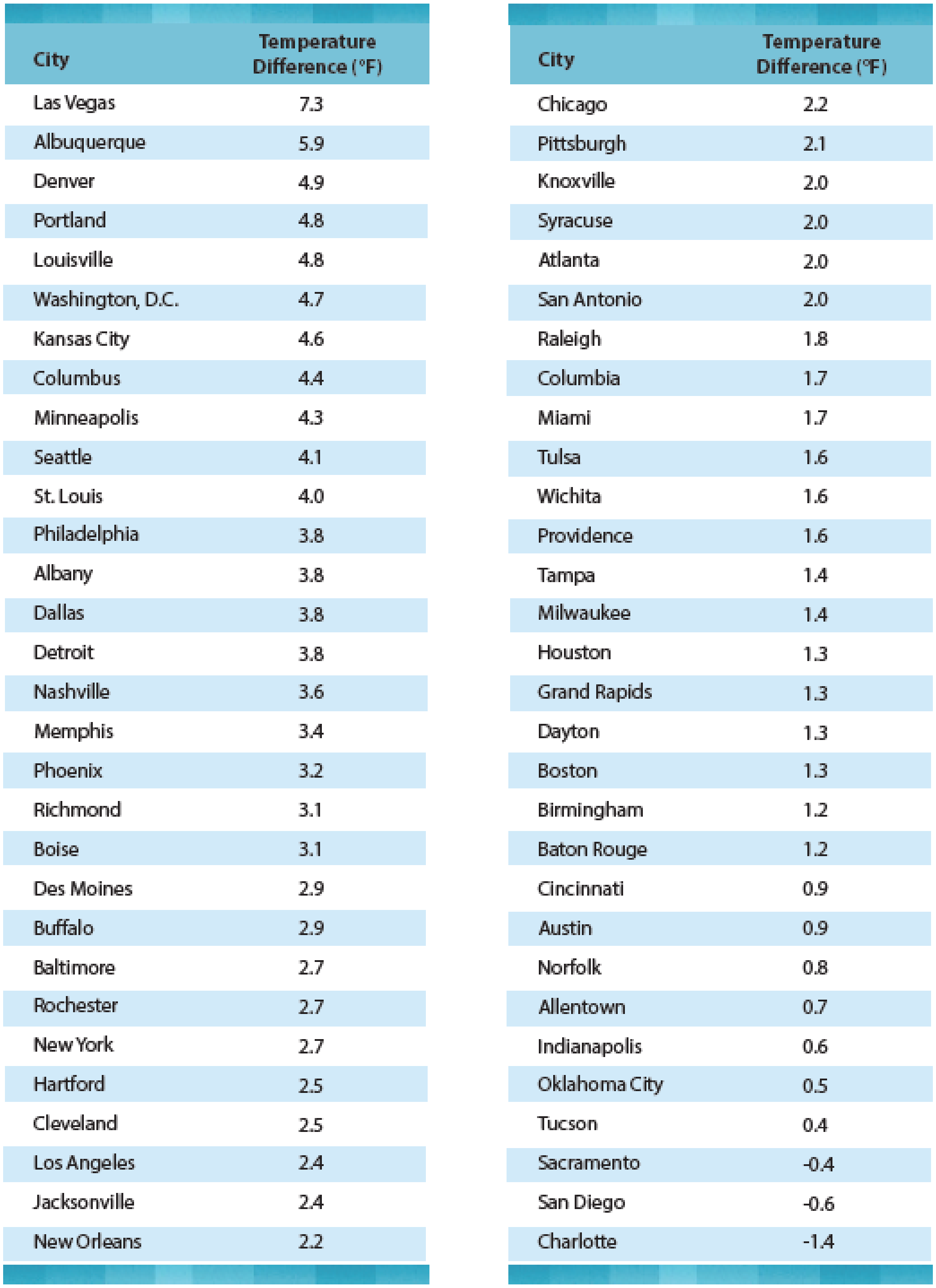

City	Temperature Difference (°F)
Las Vegas	7.3
Albuquerque	5.9
Denver	4.9
Portland	4.8
Louisville	4.8
Washington, D.C.	4.7
Kansas City	4.6
Columbus	4.4
Minneapolis	4.3
Seattle	4.1
St. Louis	4.0
Philadelphia	3.8
Albany	3.8
Dallas	3.8
Detroit	3.8
Nashville	3.6
Memphis	3.4
Phoenix	3.2
Richmond	3.1
Boise	3.1
Des Moines	2.9
Buffalo	2.9
Baltimore	2.7
Rochester	2.7
New York	2.7
Hartford	2.5
Cleveland	2.5
Los Angeles	2.4
Jacksonville	2.4
New Orleans	2.2
Chicago	2.2
Pittsburgh	2.1
Knoxville	2.0
Syracuse	2.0
Atlanta	2.0
San Antonio	2.0
Raleigh	1.8
Columbia	1.7
Miami	1.7
Tulsa	1.6
Wichita	1.6
Providence	1.6
Tampa	1.4
Milwaukee	1.4
Houston	1.3
Grand Rapids	1.3
Dayton	1.3
Boston	1.3
Birmingham	1.2
Baton Rouge	1.2
Cincinnati	0.9
Austin	0.9
Norfolk	0.8
Allentown	0.7
Indianapolis	0.6
Oklahoma City	0.5
Tucson	0.4
Sacramento	-0.4
San Diego	-0.6
Charlotte	-1.4

Figure 1.1 Urban heat island ranking for 60 U.S. cities (Kenward *et al*. 2014).

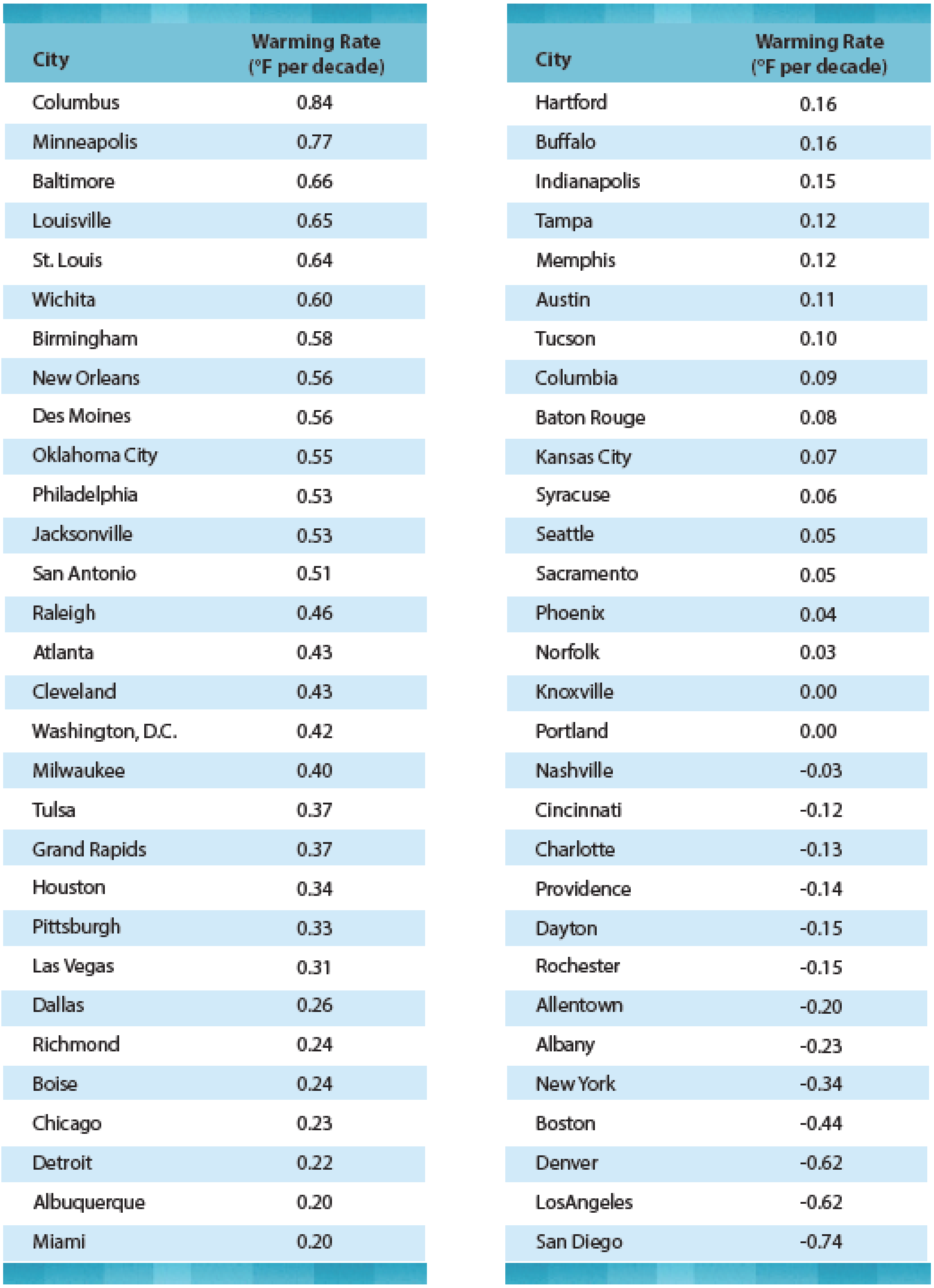

City	Warming Rate (°F per decade)
Columbus	0.84
Minneapolis	0.77
Baltimore	0.66
Louisville	0.65
St. Louis	0.64
Wichita	0.60
Birmingham	0.58
New Orleans	0.56
Des Moines	0.56
Oklahoma City	0.55
Philadelphia	0.53
Jacksonville	0.53
San Antonio	0.51
Raleigh	0.46
Atlanta	0.43
Cleveland	0.43
Washington, D.C.	0.42
Milwaukee	0.40
Tulsa	0.37
Grand Rapids	0.37
Houston	0.34
Pittsburgh	0.33
Las Vegas	0.31
Dallas	0.26
Richmond	0.24
Boise	0.24
Chicago	0.23
Detroit	0.22
Albuquerque	0.20
Miami	0.20

City	Warming Rate (°F per decade)
Hartford	0.16
Buffalo	0.16
Indianapolis	0.15
Tampa	0.12
Memphis	0.12
Austin	0.11
Tucson	0.10
Columbia	0.09
Baton Rouge	0.08
Kansas City	0.07
Syracuse	0.06
Seattle	0.05
Sacramento	0.05
Phoenix	0.04
Norfolk	0.03
Knoxville	0.00
Portland	0.00
Nashville	-0.03
Cincinnati	-0.12
Charlotte	-0.13
Providence	-0.14
Dayton	-0.15
Rochester	-0.15
Allentown	-0.20
Albany	-0.23
New York	-0.34
Boston	-0.44
Denver	-0.62
LosAngeles	-0.62
San Diego	-0.74

Figure 1.2 The change rate of urban heat island intensity in 60 U.S. cities (Kenward *et al*. 2014).

- **Mitigation of urban heat islands**

Cool roofs

Cool roofs, also called reflective roofs, are installed to elevate urban albedo. Cool roofs are generally in white color and of high albedos. Santamouris (2014) indicated that per 0.1 increase of the albedo of cool roofs can lead to 0.1–0.33°C decrease of urban temperature.

Green roofs

Green roofs, also termed living roofs, are deployed to adjust the environmental temperature. Green roofs can be treated as part of urban green spaces, which provide shading and evaporative cooling for buildings and surroundings. Santamouris (2014) estimated that applying green roofs on a city scale can reduce the overall temperature by 0.3–3°C.

Reflective pavements

Reflective pavements are either made of cold materials or painted with white, highly reflective paints or infrared-reflective paints. Cold materials are distinguished by their high reflectivity to solar radiation and high spectral emissivity (Santamouris et al. 2011). Santamouris *et al.* (2012) found that using cool paving materials in the park (4500 m^2) of greater Athens area reduced peak ambient temperature in summer by 1.9°C and lowered pavement surface temperature by 12°C.

1.3 Heat waves

1.3.1 Definition of heat waves

Although heat waves are natural climate events, they are identified based on the capacity of the population to withstand the extreme heat (Robinson 2001). There is no universal definition for a heat wave. Existing studies defined a heat wave based on one or several of the following indicators: daytime high temperatures, nighttime low temperatures, mean daily temperatures, heat index, and so forth. The widely used definitions are summarized in Table 1.1. The heat index (*HI*) was proposed by the National Weather Station (NWS 1994; NWS 2016) to estimate the physiological stress of humans when given an apparent temperature value. The apparent temperature is the air temperature in a standard environment that would produce the same thermal stress as the actual environment (Jendritzky and Tinz 2009).

In this dissertation, a heat wave is defined as at least six consecutive days in which maximum temperatures exceed the local 90th percentile of the control period from 1961 to 1990. This definition was employed by Fischer and Schar (2010) and recommended by the fifth report of IPCC (IPCC 2013). In the following, we examined the definition by varying the least number of days for a heat wave. We used the temperature data of a weather station (USC00186350, 38.9 °N, 76.9667 °W) in Washington D.C. from 1961 to 2015 (NOAA 2017). The 90th and 95th percentiles of local maximum daily temperatures from 1961 to 1990 are 31.7 °C and 33.3 °C, respectively. Figure 1.3 presents the statistics results for the maximum amplitude of heat waves each year and occurrence numbers. Defining heat waves to a smaller number of days tends to capture extreme hot temperatures better. However, for most cases, four days and six days generate the same results for maximum heat wave amplitudes. The average heat wave amplitudes each year hardly change when the threshold of day numbers decreases.

In addition, defining heat waves to a smaller number of days results in higher occurrence numbers. The requirement for at least four days results in a high value of occurrence, which is up to eight. The requirement for at least six days can lead to some years without a heat wave, but starting from the 21st century, heat wave occurred every year except the year 2004. The warming trend in the future may improve the performance of six days in characterizing heat wave frequency. The average duration of heat waves each year tends to be smaller for less required days. Overall, six days can well characterize the variation of heat wave characteristics. Compared to five and four days, six days can lead to lower amplitude, lower frequency and longer duration of heat wave results. For future projections, six days can better characterize the duration change of heat waves but may be less sensitive to frequency change.

Table 1.1 Definition of a heat wave (Zhang and Ayyub 2018).

Study	Definition
NWS (1995); Robinson (2001)	A period of at least 48 hours during which neither the nocturnal low nor the diurnal high heat index value falls below 26.7 °C and 40.6 °C, respectively.
Monteiro *et al.* (2013)	At least two consecutive days with the heat index equal to or above level III of heat-related danger; that is, the value of heat index should be no less than 41 °C.
Huth *et al.* (2000); Meehl and Tebaldi (2004); Zhou and Shepherd (2010)	The longest period of consecutive days in which: (1) the maximum temperature is above T1 for at least three days, (2) the average maximum temperature is above T1 for the entire period, and (3) the maximum temperature is above T2 for the whole period. T1 and T2 are the 97.5th and 81st percentile of the distribution of maximum daily temperature in the current climate, respectively.
Frich *et al.* (2002)	More than five consecutive days in which the daily maximum temperatures exceed the average maximum temperature by 5 °C. The average maximum temperature is determined in the period of 1961 to 1990.

Table1. Definition of a heat wave (continued).

Study	Definition
Anderson and Bell (2011); Lombardo and Ayyub (2015)	Two or more consecutive days during which the mean daily temperatures exceed local 95th percentile threshold of mean daily temperature in the control period from 1961 to 1990.
Perkins and Alexander (2012)	At least three consecutive days in which the maximum temperatures exceeding local 90th percentile of daily maximum temperature in the control period from 1961 to 1990.
Fischer and Schar (2010)	At least six consecutive days in which the maximum temperatures exceeding local 90th percentile of daily maximum temperature in the control period from 1961 to 1990.

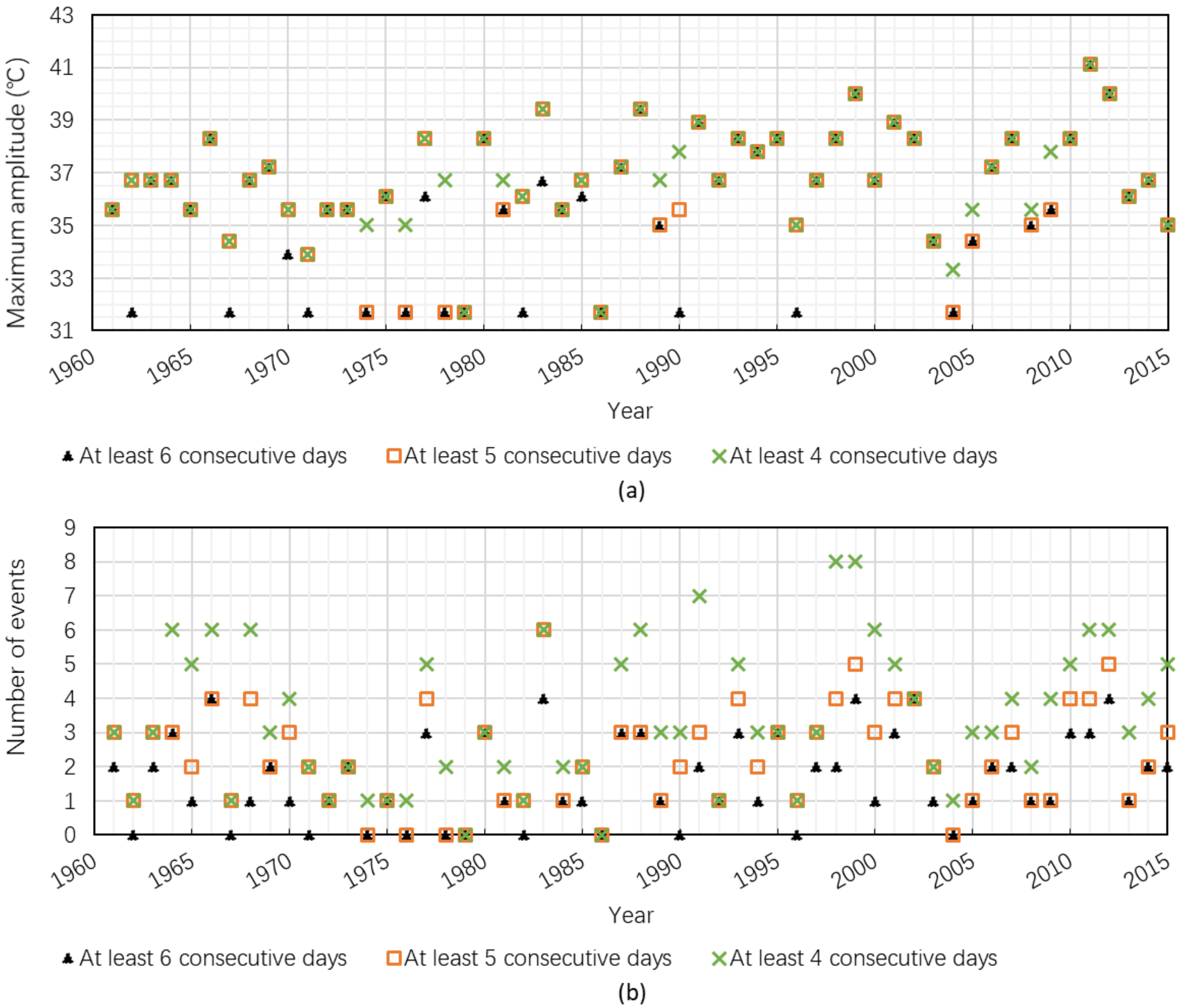

Figure 1.3 Heat waves in Washington D.C. from 1961 to 2015. (a) The maximum amplitude of heat waves each year; (b) The occurrence numbers each year for heat waves at least 6-, 5-, and 4-day long. For years without heat waves, local 90th percentile temperature (31.7 °C) is used as the amplitude value.

1.3.2 Impacts of heat waves

- **Heat-related mortality**

Exposure to extremely hot weather can lead to increased risk of deaths. The statistics of the Center for Disease Control and Prevention (CDC) indicated that from the year 1999 to 2017, extreme hot weather caused more than 7,500 deaths, greater than death tolls resulted from any other natural hazards (CDC 2018). The statistics of 43 U.S. cities from the year 1987 to 2005 suggested that the mortality risk increased by 2.65–5.04% during heat wave days relative to normal days (Anderson and Bell 2011). In addition, mortality risk may increase by 2.49% per 1 °F (0.56 °C) escalation of heat wave intensity, and increase by 0.38% per 1-day increment in heat wave duration (Anderson and Bell 2011). The elderly, children, and infants are vulnerable to extreme heat (Gouveia et al. 2003; O’Neill et al. 2005; Diaz et al. 2006; Basu and Ostro 2008; Basu 2009). Moreover, patients receiving psychotropic drug treatment for mental disorders and those taking medications that affect the body’s heat regulatory system or have anticholinergic effects are susceptible to heat exposure (Berko et al. 2014).

- **Building energy consumption**

The building energy consumption pattern is altered due to the increase in temperature. Heating demand drops during winters while cooling demand soars during summers. Space heating is largely provided by oil- or gas-fired boiler plants, while space cooling relies on electricity. Santamouris et al. (2015) estimated that 1°C of temperature increment that starts from 18 °C may result in 0.45–4.6% rise of peak electricity load and 0.5–8.5% growth of total electricity demand, dependent on building characteristics, climate zones, urban morphologies, and the type of energy services provided (*e.g.*, fans, air conditioners). Moreover, the efficiency of air conditioners declines in a hot environment, which may oblige designers to increase the size of the installed air conditioner system (Santamouris et al. 2001; Wang and Chen 2014). This elevates pressure on electricity grids and causes unstable energy supply in turn.

- **Transportation system**

Extreme heat can cause asphalt melting, concrete hogging, and malfunction of signaling equipment (McEvoy et al. 2012). McEvoy *et al*. (2012) indicated that rail infrastructure and operation is most vulnerable to heat waves in transportation systems. Extreme heat affects train operations in two ways: rail track buckling and air conditioning failure. The previous bolt joints among tracks have now been replaced with welded joints, which have no expansion gap. When new tracks expand due to heat exposure, the lack of expansion joints can result in buckling at spots of weakness. The structural weakness can be caused by one or several of the following reasons: the tracks are in poor condition due to a lack of maintenance; the tracks are not pre-stressed or welded adequately; old wooden sleepers are moved out of place due to decay or loose fastening (Osborne and McKeown 2009). The failure of air conditioning is the main reason for train cancellation during extreme hot days. The air conditioning units are typically designed to operate under 38°C, and temperature above can cause electronic fault and serious damages to electronic units (McEvoy *et al*. 2012).

- **Air quality**

Heat waves also worsen outdoor air quality (Keith *et al*. 2005; Filleul *et al*. 2006; Pu *et al*. 2017; Kalisa *et al.* 2018). The high temperature and abundant sunshine during heat waves can speed up the rate of chemical reactions, which propels the formation of ozone and fine particular matters. Ozone in the upper atmosphere plays a key role in blocking harmful solar radiation, whereas ozone in the ground level adversely affects human health. Moreover, high atmosphere pressure during heat waves constrains air convection and hinders dissipation of pollutants, which can result in a dangerously high-level concentration of ozone and fine particular matters.

1.3.3 Methods to project heat waves

The methods discussed in the UHI effect section for projecting temperature are applicable to heat waves. Heat wave projection relies on accurate temperature prediction.

1.3.4 Current statues of heat wave studies

- **Observation and projection**

The fourth national assessment (USGCRP 2018) reported that heat waves have become more frequent in the United States since the mid-1960s, and the season length of heat waves in many U.S. cities has increased by more than 40 days since 1960. The formation of heat waves starts with air sinking due to high pressure in the upper atmosphere. The subsided air acting as a dome caps atmosphere inhibits air convection and traps warm and humid air under it, resulting in continuous heat near the ground for several days or weeks (NWS 2016). The high pressure in the upper atmosphere is indicated by the 500-hPa height anomaly. Meehl and Tebaldi (2004) projected that mean height anomaly may escalate over the contiguous United States in the 21st century due to increased greenhouse gases, meaning intensified heat waves in the future. On the other hand, the UHI effect can prolong the duration of heat waves (Tan *et al.* 2010), and hinder cooling process at night, causing excessive mortality during heat waves (Basara *et al.* 2010; Laaidi *et al.* 2012). Heat waves, in turn, inhibit surface evapotranspiration and advection cooling, exacerbating the UHI effect. The synergistic effect of UHI and heat waves can be greater than the sum of its parts (Li and Bou-Zeid 2013).

- **Mitigation of heat waves**

The mitigation strategies for climate change and UHI can be utilized to mitigating heat wave impacts.

- **Adaptation to heat waves**

Adaptation for electricity systems

Electricity systems are vulnerable to temperature rise due to various reasons. First, the increase in summer temperatures leads to escalated cooling demand, intensified electricity consumption, and rising pressure on power grids. Second, the capacity and efficiency of power generation, transmission, and distribution decline as temperature increases. Third, high ambient temperatures can cause damage to electronic devices and equipment. Adapting electricity systems to extreme hot weather is important to the nation's energy security. The following bulleted list summarizes the adaptation strategies proposed by recent studies (Sathaye *et al*. 2013; Bartos *et al*. 2016; Burillo *et al.* 2016):

- Improve cooling equipment technologies for power plants and substations
- Adopt more heat-resistant conductor technologies (*e.g.*, aluminum conductor steel supported conductors)
- Place overhead power lines underground
- Deploy smart grid power flow controls
- Diversify the power generation mix (*e.g.*, solar energy, wind)
- Design effective demand-side management programs
- Improve customer energy efficiency
- Upgrade infrastructure to be more thermal resistant

Rooftop photovoltaics

Rooftop photovoltaics (PV) is gaining increased attention as a clean energy technology that converts the sun's rays into electricity directly for building use. The benefits of solar PV have been discussed extensively in the literature, including lowering energy costs, reducing greenhouse gas emissions, decreasing harmful air pollutants, improving public health, providing work opportunities, and enhancing the reliability and security of electric power systems (Tsoutsos et al. 2005; Kats and Glassbrook 2016). Gagnon *et al*. (2016) estimated that small buildings can provide 731 GW of PV capacity and generate 926 TWh/year of PV energy, and medium and large buildings have a total installed capacity potential of 386 GW and energy generation potential of 506 TWh/year in the United States. The total national technical potential of rooftop PV is 1,118 GW of installed capacity and 1,432 TWh of annual energy generation, which equals to 39% of total national electric-sector sales (Gagnon *et al*. 2016).

1.4 Knowledge gap, objectives, and research questions

The urban heat island (UHI) effect and heat waves are becoming more intense across most U.S. cities due to global climate change (Kenward *et al.* 2014; Habeeb *et al.* 2015). The UHI effect often leads to increased cooling energy demand (Konopacki and Akbari 2002), decreased air quality (Ebi *et al.* 2008; Leung and Gustafson 2005), and rising risks of heat-related health problems (Tan *et al.* 2010; Kenward *et al.* 2014). Heat waves are among the deadliest natural hazards, which caused more than 7,500 deaths in the U.S. from the year 1999 to 2017 (CDC 2018). Characterizing the future trends and levels of the UHI effect and heat waves is important for cities to plan and initiate appropriate climate adaptations.

Analyzing future trends of heat-related conditions for cities needs high-resolution temperature projections. However, the spatial resolution of a typical global climate model is 1×1 degree, corresponding to a grid size of 110.03 km (in latitude) × 85.39

km (in longitude) at latitude 40 degrees, which does not meet the requirement of local-scale studies. Increasing the resolution of global climate models can be very expensive, as raising the resolution by a factor of two needs ten times as much computing power. To solve this problem, climate researchers developed statistical and dynamical downscaling techniques to adjust global simulations to local results.

Many studies have used the downscaled results of a single or multiple global climate models archived in the Coupled Model Intercomparison Project Phase Three (CMIP3) to analyze the UHI effect and heat waves for the U.S. cities (*e.g.*, Hayhoe *et al.* 2010; Dole *et al.* 2011; Lau and Nath 2012; Cowan *et al.* 2014; Schoetter *et al*. 2015), whereas few studies used the Coupled Model Intercomparison Project Phase Five (CMIP5) data for such purpose. The CMIP5 incorporates the latest and most sophisticated climate model experiments worldwide (Taylor *et al.* 2012; Wuebbles *et al.* 2014), and shows superior performance in simulating climate change and its uncertainties compared to the CMIP3 (Sheffield *et al.* 2013a; Sheffield *et al.* 2013b; Taylor *et al.* 2012). Therefore, this dissertation utilized CMIP5 data to improve heat-related projections for cities.

The communities that have experienced heat waves may suffer from greater frequencies and intensities in the future (Meehl and Tebaldi 2004; Kunkel *et al.* 2010; Russo *et al*. 2014). With urban sprawling, the influence of heat waves may expand to new regions. The communities newly exposed to extreme heat can be vulnerable due to the lack of experience and preparedness. Therefore, it would be important to understand the spatial and temporal variation of heat waves so that appropriate actions can be taken to improve the community's resilience to extreme heat. This dissertation projected the variation of heat waves in the Washington metro area, as this area has more than six million residents (Census 2019) and suffered from increased heat waves in past decades (Habeeb *et al.* 2015; Lombardo and Ayyub 2015).

A large number of studies (Kalnay and Cai 2003; Tan *et al.* 2010; Stone *et al.* 2013; Li and Bou-Zeid 2013; Habeeb *et al*. 2015) have demonstrated that UHIs can intensify heat waves, which suggests a promising way to reduce the impacts of heat waves by mitigating the UHI effect. The popular mitigation technologies for UHIs include cool roofs, green roofs, and reflective pavements (Santamouris *et al.* 2012; Santamouris 2014; Li *et al*. 2014). However, those technologies were tested under current climate condition, and their performance under intensified heat conditions is unclear. In addition, to what degree those technologies can moderate heat waves has not been assessed, which is critical to developing effective heat mitigation strategies and policies for cities.

Electrical power systems are particularly vulnerable to extreme heat, as heat waves not only increase electricity consumption, but also decrease the capacity and efficiency of electricity generation, transmission, and distribution sectors. The vulnerability of national power grids has been extensively studied (*e.g.*, DOE 2013; Bartos *et al.* 2016), but those studies used coarse, national temperature projection and general information on energy resources and infrastructure. As a result, their results do not accurately reflect local susceptibility levels. On the other hand, local-scale studies mostly focused on the power grids of the western (e.g., Sathaye *et al.* 2013; Bartos and Chester 2015; Burillo *et al.* 2016) and southern (e.g., Allen *et al*. 2016) United States, whereas the vulnerability of the eastern region was less studied. To fill the gap, this dissertation incorporated high-resolution temperature projections, summer cooling load predictions, electrical network model, and system failure model into a quantitative and systematical assessment on the potential change of grid vulnerability in the Washington metro area.

Rooftop photovoltaics (PV) is a clean energy technology that converts sunlight into electricity directly for building use. The benefits of Rooftop PV include, among others, lowering energy costs, reducing greenhouse gas emissions, decreasing harmful air pollutants, improving public health, and enhancing the resilience of electrical power systems (Tsoutsos et al. 2005; Kats and Glassbrook 2016). The government of Washington D.C. has launched a smart roof program and solar incentive programs to encourage rooftop PV installation in the district (BLUEFIN 2013; DOEE 2016). Moreover, the government attempts to maximize renewable energy generation, especially solar energy, in order to achieve the goal of carbon neutrality by 2050 (DOEE 2018). Investigating adoption potential and cost-effectiveness of rooftop PV would help cities, like Washington D.C., make the best use of solar energy and achieve the resilience and sustainability goal.

In summary, this dissertation addressed three questions that are critical for improving urban heat-related projection and adaptation techniques. First, how to generate accurate and reliable projections for the UHI effect and heat waves at a local scale? Second, to what degree can cool roofs, green roofs, and reflective pavements mitigate heat waves, and will their performance change under intensified warming climate? Third, how does the increase in temperature affect the vulnerability of electricity systems, and how to make the best use of rooftop photovoltaics to improve the resilience of electricity systems?

1.5 Organization of the dissertation

Chapter 1 provides the definitions of climate change, the UHI effect, and heat waves, and describes their impacts on the environment and society. A literature review is included to introduce the methods and models employed by climate studies as well as the current status of climate mitigation and adaptation practice. Knowledge gaps, objectives, and research questions addressed in this dissertation are elaborated.

Chapter 2 describes the work that was published in the ASCE journal last year. In this work, an observational analysis was conducted to reveal the trends of the UHI effect and heat waves at Washington D.C. in the last six decades. In addition, the future trends and levels of the UHI effect and heat waves were projected using an improved downscaling strategy. The new strategy used the Asynchronous Regional Regression Model (ARRM) that statistically downscales CMIP5 simulations into the location of observing stations. This downscaling method develops a quantile relationship between historical observations and simulations, and employs this relationship to project future temperatures at the location of stations. Simulation datasets were created by coupling ten global climate models archived in CMIP5 with the same weight. Observation datasets were obtained from two stations in the city and two stations in suburbs. The developed ARRMs were validated using three reliability measures. Downscaled temperature projections were then utilized to predict the UHI effect and heat waves. The highest and lowest concentration scenarios, RCP 8.5 and RCP 2.6, were considered in the projection to account for future climate uncertainties.

Chapter 3 presents the study carried out on heat wave projection and mitigation. The projection was made by using the Weather Research and Forecasting (WRF) model that dynamically downscales the Community Earth System Model version one (CESM1) data into fine-grid results. This projection helps to understand the temporal and spatial variation of heat waves in the rest of the current century and to locate potential vulnerable population and assets in the Washington metro area. The impacts of climate change and UHIs to heat wave growth were assessed respectively. In addition, five strategies based on cool roofs, green roofs, and reflective pavements were evaluated in three future time periods regarding their effectiveness in reducing heat wave amplitude and warm spell duration. Uncertainties associated with the efficacy of those strategies were analyzed, including land use types, the magnitude of roof and pavement albedos, the replacement rate of green roofs, and daytime and nighttime conditions.

Chapter 4 describes our recent progress in assessing the vulnerability of electricity systems to temperature rise in the rest of the century. The high-resolution temperature projections made in previous work were used to predict summer peak loads and failure probability of single component and the entire electricity system in a future warming climate. An electrical network model and system failure model were created to assist vulnerability analysis. In addition, an adaptation assessment framework that incorporates the probabilistic risk approach was developed to improve uncertainty and sophisticated relations modeling. This framework consists of four steps: exposure projection, sensitivity measurement, adaptation capacity evaluation, and decision making. Each step generates a set of conditional probabilities to support risk assessment. This framework was applied to evaluating and optimizing rooftop PV strategies in order to help make the best use of solar energy and improve power system resilience.

Chapter 5 concluded and discussed the implications of the dissertation to future research. Appendix A compared statistical and dynamical downscaling results. Appendix B explained physical mechanisms employed in the WRF model. Appendix C described the electrical network model created for failure analysis. Appendices D and E provided detailed information on cost-benefit analysis for rooftop PV, cool roof, green roof, and reflective pavement strategies.

Chapter 2: Urban Heat Projections in a Changing Climate: Washington D.C. as a Case Study

2.1 Introduction

The urban heat island (UHI) effect and heat waves are becoming more intense across most U.S. cities due to global climate change (Kenward *et al.* 2014; Habeeb *et al.* 2015). The UHI effect often leads to increased cooling energy demand (Konopacki and Akbari 2002), decreased air quality (Ebi *et al.* 2008; Leung and Gustafson 2005), and rising risks of heat-related health problems (Tan *et al.* 2010; Kenward *et al.* 2014). Heat waves are among the deadliest natural hazards, which caused more than 7,500 deaths in the U.S. from the year 1999 to 2017 (CDC 2018).

This dissertation proposes and develops a new method to project the UHI effect and heat waves on a local scale using downscaled Coupled Model Intercomparison Project Phase Five (CMIP5) data. A statistical downscaling technique, named Asynchronous Regional Regression Model (ARRM), is applied to adjust CMIP5 simulation to the location of station-based observation. Additionally, the dissertation projects future trends and levels of the UHI effect and heat waves in Washington D.C. Overall, this study provides new insights for climate-change studies regarding heat unbalance and extreme heat events. The projection results would help engineering practitioners evaluate and foresee heat-related problems in Washington D.C. and other similar cities, and assist public policy development on urban climate adaptations.

The UHI effect describes the phenomenon whereby metropolitan areas are significantly warmer than their surroundings (EPA 2016; Santamouris 2015; Kolokotroni *et al.* 2012). The UHI effect is usually attributable to the intense human activities that release considerable heat and replacement of large-scale vegetation with roads, buildings, and other structures (Memon *et al.* 2008). Heat waves are extended periods of excessive heat that cause abnormal stress on humans (Robinson 2001). The formation of heat waves starts with air sinking due to high pressure in the upper atmosphere. The subsided air acting as a dome caps atmosphere inhibits air convection and traps warm and humid air under it, resulting in continuous heat near the ground for several days or weeks (NWS 2016).

Although heat waves are natural climate events, they are identified based on the capacity of the population to withstand the extreme heat (Robinson 2001). Several different criteria, as presented in Table 1.1, have been suggested to define heat waves. The heat index (*HI*) was proposed by the National Weather Station (NWS 1994; NWS 2016) to estimate the physiological stress of humans when given an apparent temperature value. The apparent temperature is the air temperature in a standard environment that would produce the same thermal stress as the actual environment (Jendritzky and Tinz 2009). Consistent with the 5th Assessment Report of the Intergovernmental Panel on Climate Change (IPCC), this study defines a *heat wave* as a spell of at least 6 consecutive days in which maximum temperatures exceeding the local 90th percentile of the control period from 1961 to 1990 (IPCC 2013; IPCC 2014).

CMIP5 model ensemble was published in the 5th IPCC climate change assessment report (IPCC 2013; IPCC 2014), incorporating the latest and most sophisticated climate model experiments worldwide (Wuebbles *et al.* 2014; Taylor *et al.* 2012). Compared to single AOGCM, a multiple model ensemble has shown superior performance for historical climate assessment (Pierce *et al.* 2009), because coupling these models can take advantages of their strengths and compensate limitations. Compared to the previous model ensemble CMIP3, CMIP5 has a higher spatial resolution, improved parametrizations, and additional trajectories for future assumptions, facilitating simulations for regional climate and projections under complicated future uncertainties (Sheffield *et al.* 2013a; Sheffield *et al.* 2013b; Taylor *et al.* 2012).

The UHI effect and heat waves are projected based on temperature data. Most studies utilized temperature data of a single or multiple Atmosphere-Ocean General Circulation Models (AOGCMs) to project the UHI effect (Wilby 2003) and heat waves (Hayhoe *et al.* 2010; Dole *et al.* 2011; Lau and Nath 2012; Cowan *et al.* 2014; Schoetter *et al*. 2015) for the entire 21st century. A small number of studies relied on regional climate models (Li and Bou-Zeid 2013; Diffenbaugh *et al.* 2005). However, few studies employed downscaled CMIP5 projections to the climate-change study of U.S. cities, and hence the performance for this purpose has not been assessed yet.

Existing studies for extreme heat events indicated that CMIP5 can capture well the observed mean heat wave characteristics of past decades for Europe (Schoetter *et al*. 2015) and Australia (Cowan *et al.* 2014). Studies assessing North America climate change implied that median values produced by CMIP5 can represent central tendencies of climate variables well, though CMIP5 has a hard time in reproducing extreme temperature values in dry periods of dryer regions due to complex land hydrology (Sheffield *et al.* 2013a). The overall performance of CMIP5 is dependent on the coupled AOGCMs, and these AOGCM may perform well for several metrics but poorly for other metrics (Sheffield *et al.* 2013a; Sheffield *et al.* 2013b; Maloney *et al.* 2014).

Washington D.C. is selected to demonstrate the proposed approach because of its rising heat-related risk. In 2014, Washington D.C. including its surrounding suburbs was rated the seventh-largest metropolitan area in the U.S. with an estimate of six million residents. Meanwhile, Washington D.C. was ranked the sixth among U.S. cities for the worst UHI effect (Kenward *et al.* 2014). Moreover, the frequency and duration of heat waves are increasing. Compared to the years 1950–1980, the number of occurrences increased by 1.4, the duration of heat waves rose by 25 %, corresponding to an increase of 0.6 days, during the years 1981–2012 (Lombardo and Ayyub 2015). The definition of this heat wave is given in Table 1.1.

The chapter is organized as follows. The next section introduces the CMIP5 model ensemble and ARRM downscaling model and discussing their strengths and weaknesses when applied to climate projections. Then the UHI effect of Washington D.C. is analyzed based on historical observation and projected to the end of the 21st century. In the projection process, downscaling models are developed and assessed by three reliability measures. Next, heat waves and extreme temperature indices of Washington D.C. are investigated and projected for the entire 21st century. The last section concludes the study and discusses the implications of the findings.

2.2 Models and methods

2.2.1 CMIP5 model ensemble

The inputs for CMIP5 standard model 'r1i1p1' include NO/NO_2/NH_3 emissions caused by deposition and fertilization in croplands, anthropogenic land use change, interactive carbon-nitrogen cycling, carbon-nitrogen dynamics, and CH_4 emissions on peatlands (Stocker *et al.* 2013). Four trajectories are devised to address the future uncertainties regarding emissions and concentrations of greenhouse gasses and aerosols, land change, and solar radiations (IPCC 2013). The four trajectories are Representative Concentration Pathways (RCP) 2.6, RCP 4.5, RCP 6.0, and RCP 8.5, corresponding to radiative forcing of 2.6, 4.5, 6.5, and 8.5 W/m^2 by 2100, respectively (IPCC 2013). *Radiative forcing* is defined as the net change in the energy balance of the Earth system because of natural and anthropogenic substances and processes, relative to the reference year of 1750 (IPCC 2013). The four trajectories assume CO_2 concentrations of 421, 538, 670, and 936 ppm by 2100, and greenhouse gas concentrations (CO_2, CH_4, N_2O) of 475, 630, 880, and 1313 ppm by 2100, respectively (IPCC 2013).

The highest concentration scenario RCP 8.5 and the lowest concentration scenario RCP 2.6 are studied to account for future uncertainties. Scenario RCP 8.5, also called business-as-usual scenario, describes a heterogeneous world where economy and technology develop slowly and restrict the improvement of energy efficiency, and global population grows continuously and consumes considerable energy, resulting in long-term high greenhouse gas emissions and the absence of mitigation policies for climate change (Riahi *et al.* 2011). In contrast, scenario RCP 2.6 (also named RCP3-PD) assumes that strong mitigation actions are taken, and thereby the radiative forcing will increase to 3 W/m^2 and then decline to 2.6 W/m^2 at the end of the 21st century (IPCC 2013).

The grid resolution of CMIP5 model ensemble is 1×1 degree, corresponding to the length of 110.03 km (in latitude) × 85.39 km (in longitude) at latitude 40 degrees. Coupled AOGCMs are adjusted to this resolution for consistency. However, the gird resolution is still too coarse for local climate simulation (ASCE Committee on Adaptation to a Changing Climate 2015). Therefore, dynamical and statistical techniques are developed to downscale global projections to finer-grid results. Compared to dynamical methods, statistical methods have advantages of inexpensive computation and are simple to use and apply (Chen *et al.* 2012), although the assumption of stationary predicator–predictand relationships may weaken the accuracy of future projections (Barsugli *et al.* 2013). The predictor refers to model simulation, and predictand is observation. Statistical methods assume the relationship between the model simulation and observation is stationary, and hence the relationship derived from the historical period can be applied to projecting future conditions (Stoner *et al.* 2013). However, this relationship may change slightly over time, which is discussed in the later section.

2.2.2 ARRM downscaling model

ARRM is one of the empirical statistical downscaling models, capable of downscaling global projections to the station- or fine grid-based observations (as used in Dettinger *et al.* 2004; Hayhoe *et al.* 2010; Themeßl *et al*. 2011; Gudmundsson *et al.* 2012; Stoner *et al.* 2013). ARRM relies on empirical quantile mapping technique which assumes that two independent time series should have similar probability density functions (PDF) if they describe the same variable and are at approximately the same location, such as the temperatures simulated by a climate model and observed by a weather station for the same location (Hayhoe *et al.* 2010; Stoner *et al.* 2013).

In probability theory, quantiles are cut points that divide the range of a probability distribution into contiguous intervals with equal probability. In statistics, quantiles divide an ascending dataset [x_1, x_2... x_n] of variable x into q equal-sized subsets. Assuming the i^{th} quantile corresponds to the value x_i, then the i^{th} quantile implies the probability of i/q that the variable is equal to or less than the value x_i, and the probability of $(q - i)/q$ that the variable is greater than the value x_i (Stoner *et al.* 2013).

Themeßl *et al*. (2011) summarized three features of the empirical quantile mapping technique as follows: (1) Distribution-based. The data are calibrated on their empirical cumulative distribution function (CDF), rather than the paired data. (2) Direct. The predictor and predictand depict the same variable. The predictor is model simulated variable, and predictand is observed same variable. (3) Parameter-free. The simulation uses empirical CDF, rather than theoretical CDFs (*e.g.*, normal, exponential distribution). Such a model feature makes ARRM more competitive in meteorological and hydrological predictions, because the distribution of most variables may not conform to any theoretical distributions.

Figure 2.1 presents the flow chart of applying ARRM to downscaling the information of global climate model. The first step of ARRM is to rank the observed historical data and model simulated historical data in ascending sequences based on respective values regardless of timestamps. The second step is to develop a mathematical relationship between observation and model simulation by using quantile regression function to fit the ranked results. The last step is to downscale (also called correct or train) model projections using the developed regression function.

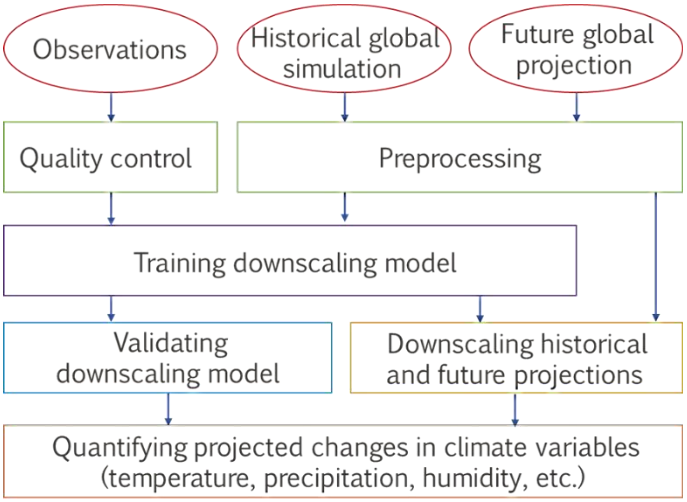

Figure 2.1 Asynchronies Regional Regression Modeling (ARRM) system flow chart (Stoner et al. 2013).

Piecewise linear regression (also termed segmented linear regression) is commonly used to simulate the predictor-predictand relationship for its advantages in capturing the values near the tails of the distribution and avoiding overfitting when appropriate breakpoints are chosen (Dettinger *et al.* 2004; Stoner *et al.* 2013). The number and position of breakpoints are set by users manually, and appropriate breakpoints should prevent negative slopes in any segments when fitted by linear functions. Literature has suggested using a fixed window width to set breakpoints, and adding more breakpoints to the tail of distribution to capture extreme values (Stoner *et al.* 2013). The window width (*e.g.*, 5 % or 10 % of the distribution) is dependent on the variability of the predictor-predictand relationship. Once breakpoints are selected, piecewise regression creates regression functions for each segment based on the least-squares scheme, which minimizes the sum of squared residuals in each segment to generate the best fitting results. The details for creating the ARRM downscaling model are demonstrated as follows.

Firstly, ranking the historical time series of model simulated variable (x) and observed same variable (y) to ascending datasets, [x_1, x_2... x_n] and [y_1, y_2... y_n], where x_i and y_i are in the same quantile of their respective CDF. The piecewise regression function with one breakpoint (BP) can be written as follows:

$$y_{p,h} = \begin{cases} A_{1,int}x_h + B_{1,int} & x_h < BP \\ A_{2,int}x_h + B_{2,int} & x_h \geq BP \end{cases} \tag{2.1}$$

where x_h = model simulated value in the historical period; $y_{p,h}$ = predicted value for a particular value of x_h; $A_{1,int}$, $A_{2,int}$ = initial coefficients implying slopes of the linear regressions; and $B_{1,int}$, $B_{2,int}$ = initial constants implying the intercepts of the linear segments at the y-axis.

The prediction errors or residuals, e, can be expressed as follows:

$$e = \begin{cases} y - A_1x - B_1 & x < BP \\ y - A_2x - B_2 & x \geq BP \end{cases} \tag{2.2}$$

Using the least-squares method to minimize fitting errors of each segment yields the optimized parameters $A_{1,opt}$, $A_{2,opt}$, and $B_{1,opt}$, $B_{2,opt}$. The least-squares optimization was conducted on a commercial software package MATLAB (R2016a) that is developed by the MathWork Inc. Substituting these parameters into Equation 2.1, the piecewise regression model is formulated as follows:

$$y_{p,f} = \begin{cases} A_{1,opt}x_f + B_{1,opt} & x_f < BP \\ A_{2,opt}x_f + B_{2,opt} & x_f \geq BP \end{cases} \tag{2.3}$$

where x_f = model projected value in the future; $y_{p,f}$ = predicted value for a particular value of x_f.

Equation 3 is then employed to downscale model projections. The model projected values that are out of the range found in the historical simulation should be adjusted using the regression function developed for the end segment. It should be noted that the projection results, $y_{p,f}$, are mapped in quantiles with model projections, x_f. To obtain the time series of the variable, prediction results should be sorted via the timestamp provided by model projections.

2.3 The UHI effect

2.3.1 Measurement of the UHI effect

The strength of the UHI effect is generally measured by the UHI intensity. The UHI intensity is determined as the spatially averaged temperature difference between the urban and surrounding areas (Magee *et al.* 1999; Kim and Baik 2005). The mean and maximum UHI intensity are two major indicators, referring to the differences in mean and maximum temperatures, respectively. The period of comparison can be a year, a season, a month, a few days, or even the portion of a day (Velazquez-Lozada *et al.* 2006). Temperature types (*e.g.*, air or surface temperatures) and measurement methods (*e.g.*, automobile data, satellite data, or weather stations) can affect the observed results for UHI intensity (Memon *et al.* 2008).

The U.S. Census (2010) defined ‘urban areas’ as two parts: urbanized areas where population densities are greater than 1,930 people/km^2 and urban clusters where populations are between 965 and 1,930 people/km^2. For rural areas, populations are less than 965 people/km^2. This study selected four weather stations that provide the most complete temperature records for Washington D.C. and its surroundings. The spatial distributions of these weather stations are illustrated in Figure 2.2. Stations 1 and 2 are located in Washington D.C. and surrounded by urban parks. Temperatures measured by the two stations can be lower than that at dense residential and commercial areas because of the cooling effect of vegetation. Station 3 is in Dulles, VA, and Station 4 is in Greater Upper Marlboro, MD. The regions where Stations 3 and 4 located are suburbs because their populations are lower than the threshold of urban areas. Temperatures measured by Stations 3 and 4 can be higher than other suburban and rural areas because the two are nearby urban boundaries.

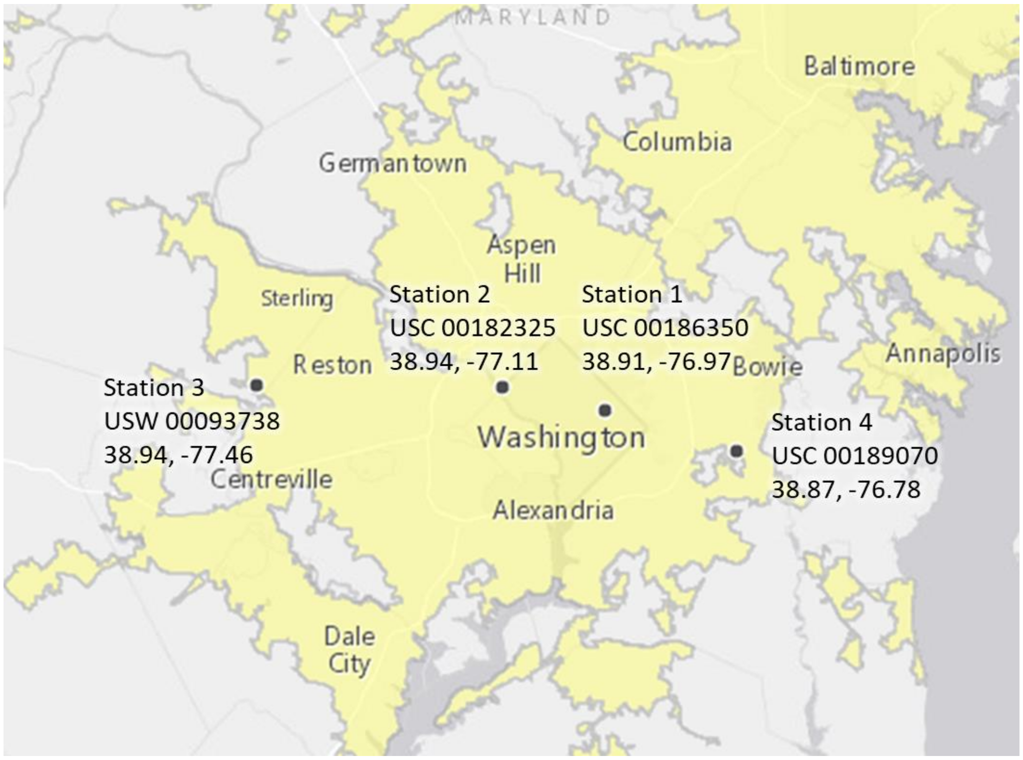

Figure 2.2 Spatial distribution of four weather stations. Yellow areas denote urban areas in the year 2015.

2.3.2 Observational analysis

The annual UHI intensity is measured as the annual temperature difference between the city (Stations 1 and 2) and suburbs (Stations 3 and 4). The annual maximum and minimum temperatures observed by four stations from 1950 to 2015 are compared in Figure 2.3. Data are obtained from NOAA daily summary (NOAA 2016). Annual maximum and minimum temperatures are calculated by averaging daily maximum and minimum temperatures of 365 days. Daily maximum and minimum temperatures are higher at Washington D.C. (Stations 1 and 2) compared to suburbs (Stations 3 and 4), though the difference between the city and suburbs shows a declining trend because of ongoing urbanization in suburbs. These observations are consistent with the study of Tan *et al.* (2010) for Shanghai, China, and the study of Zhou and Shepherd (2010) for Atlanta, GA. They both indicated that temperature gaps are growing between urban and rural areas, but shrinking between urban and suburban areas.

2.3.3 Model creation and evaluation

The reference period for creating ARRM should be long enough to capture a general relationship between the observation and simulation and prevent disturbances from minor abnormal observations. Considering the availability and quality of data as well, the reference period determined for the four stations is from 1965 to 2000. The CMIP5 simulated daily temperatures in the nearest grid point are extracted from Lawrence Livermore National Laboratory (LLNL) netCDF software packages (LLNL 2016). Ten AOGCMs from CMIP5 are coupled using equal weights, as listed in Table 2.1. Details for these AOGCMs are documented in the Program for Climate Model Diagnosis and Intercomparison (PCMDI 2016) and Maloney *et al.* (2014). The data points missing in observation sets should be removed in simulation sets (the same timestamp) to maintain correspondence and consistency.

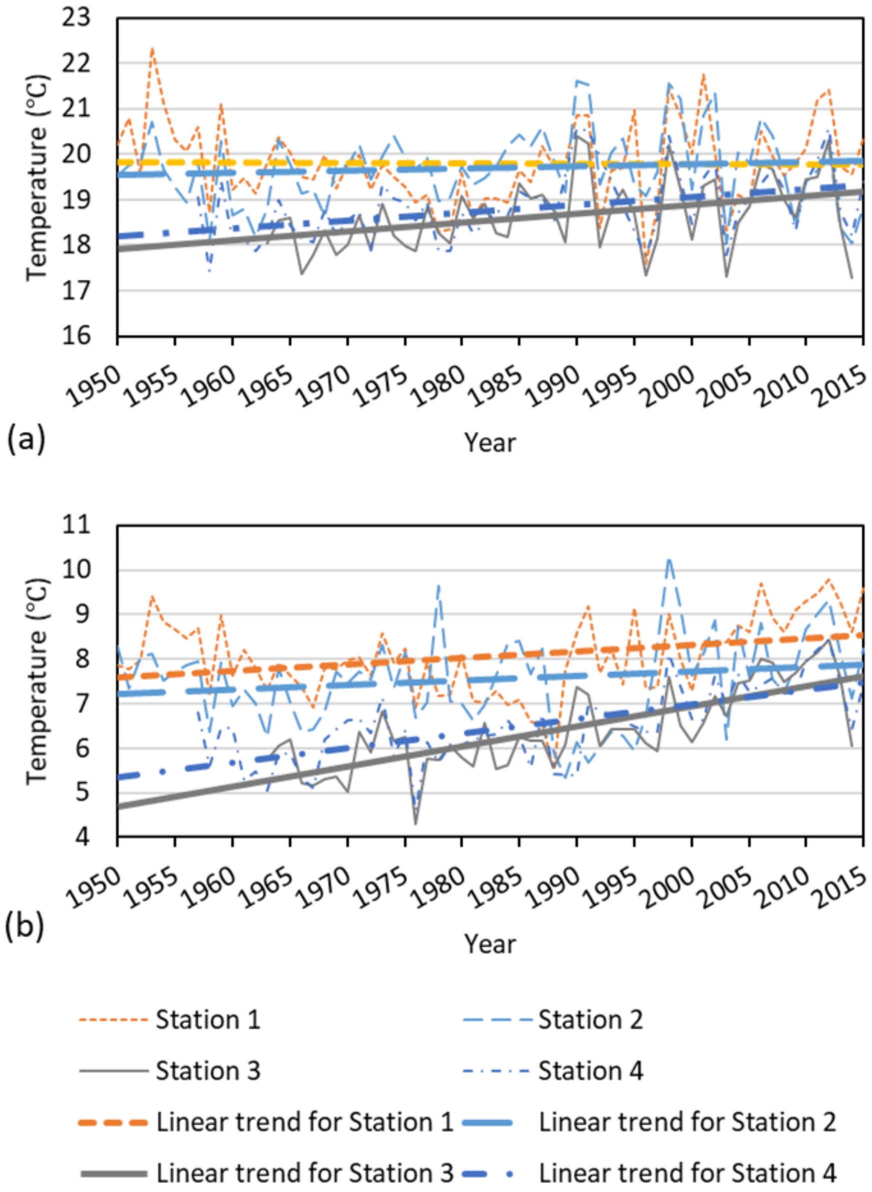

Figure 2.3 Annual temperatures observed by four stations during 1950–2015 and corresponding linear trend lines: (a) maximum temperatures; (b) minimum temperatures.

Table 2.1 The CMIP5 models coupled for urban heat study.

Model	Institution
BCC-CSM1.1	Beijing Climate Center, China Meteorological Administration, China
CanESM2	Canadian Centre for Climate Modeling and Analysis, Canada
CCCSM4	National Center for Atmospheric Research (NCAR), USA
CSIRO-Mk3.6.0	Australian Commonwealth Scientific and Industrial Research Organization, Australia
GFDL-CM3	NOAA Geophysical Fluid Dynamics Laboratory, USA
GFDL-ESM2G	NOAA Geophysical Fluid Dynamics Laboratory, USA
IPSL-CM5A-LR	Institut Pierre-Simon Laplace, France
MIROC5	AORI (Atmosphere and Ocean Research Institute), NIES (National Institute for Environmental Studies), JAMSTEC (Japan Agency for Marine-Earth Science and Technology), Japan
MPI-ESM-LR	Max Planck Institute for Meteorology, Germany
MRI-CGCM3	Meteorological Research Institute, Japan

Six data points are evenly selected from each month to construct observation and simulation sets for the four stations. These sets are then ranked respectively in ascending sequence, as shown in Figure 2.4 for daily maximum and minimum temperatures at Station 1, which is similar to the other stations. A striking correlation can be observed between the observed and CMIP5 simulated daily maximum and minimum temperatures. Based on visual testing, seven breakpoints are set at the 1st, 10th, 25th, 50th, 75th, 90th, and 99th quantile of distribution for linear piecewise regression to fit the scatter profile of those points. Figure 2.4a illustrates quantile mapping between observations and simulations and linear piecewise regression function employed in simulating the quantile relationship. Two more breakpoints are added at the 40th and 60th quantile for the regression function of Station 4, because of the variability in the mid-section of its scatter profiles. After adjusted by piecewise regression function, the distributions of CMIP5 simulation are close to those of local observation, as shown in Figure 2.5 for daily maximum and minimum temperatures at Station 1, respectively.

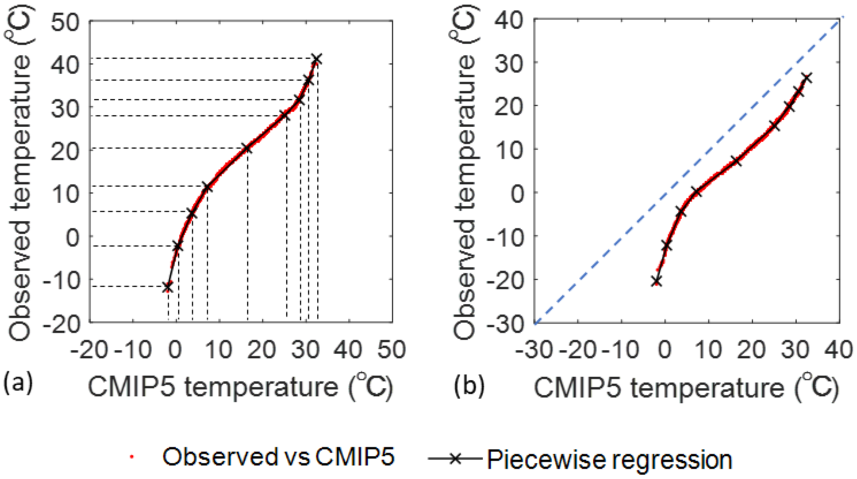

Figure 2.4 Scatter plot of observed *versus* CMIP5 simulated temperatures at Station 1 during 1965–2000 (ordered by rank), and linear piecewise regression fitting: (a) maximum daily temperatures and quantile mapping between observations and simulations (1st, 10th, 25th, 50th, 75th, 90th, 99th quantiles); (b) minimum daily temperatures.

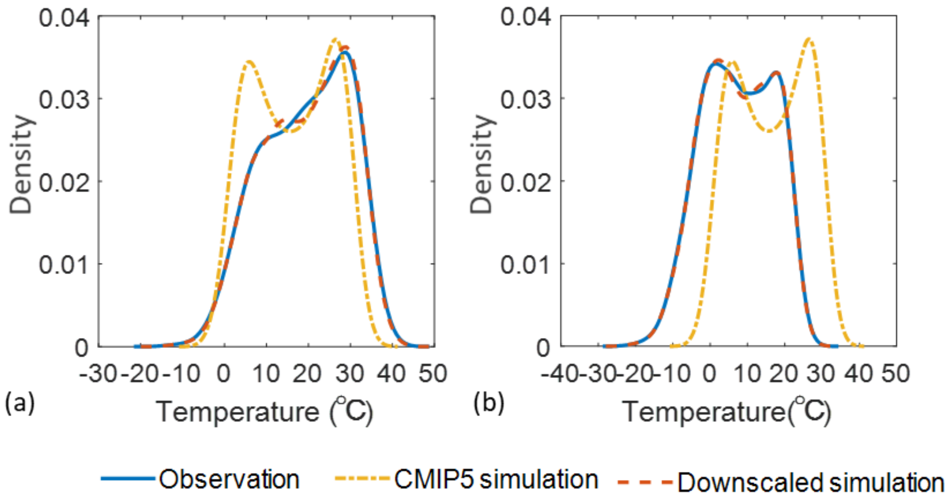

Figure 2.5 Probability density distributions of observed, CMIP5 simulated, and downscaled CMIP5 simulated temperatures at Station 1 during 1965–2000: (a) maximum daily temperatures; (b) minimum daily temperatures.

Three measures are taken to evaluate the performance of the downscaling model. Firstly, the method of Root-Mean-Square errors (RMSEs) is employed to assess the ability of the downscaling model to reproduce observations. RMSE is the standard deviation of the differences between predicted values and observed values. Figure 2.6 displays the RMSE results for daily maximum and minimum temperatures at the four stations. All RMSEs are lower than 0.25 °C, indicating the high accuracy of developed downscaling models.

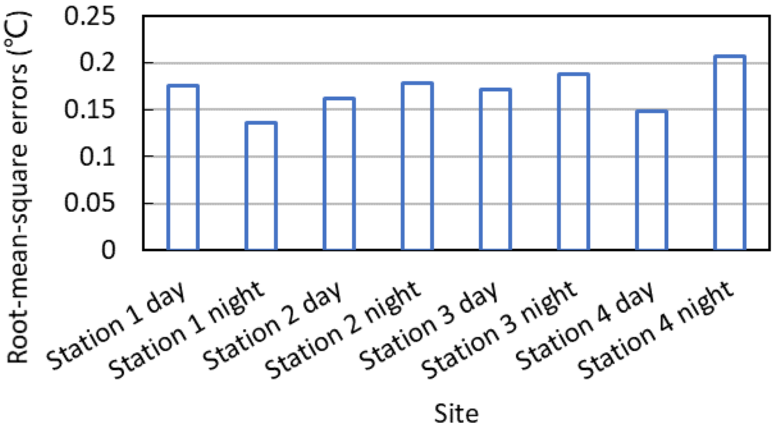

Figure 2.6 Root-mean-square errors for downscaled CMIP5 results relative to observations.

The second measure evaluates the capacity of the downscaling model to recreate the probability distribution of observed temperatures. Seven quantiles of the distribution, consisting of the 1st, 10th, 25th, 50th, 75th, 90th, and 99th quantiles, were assessed as shown in Figure 2.7. The error is calculated as the difference between downscaled CMIP5 simulation and observation. A positive error implies over-prediction and a negative error means under-prediction. All the errors analyzed are within ±0.65 °C, with no clear attributions of negative or positive, large or small (Figure 2.7).

Like any other statistical downscaling models, ARRM is built on the assumption that the relationship between observation and simulation is time-invariant. However, such an assumption is often arguable (Hayhoe *et al*. 2008), and the potential shift of their relationship can affect the ability of the downscaling model to project future conditions. Therefore, the third measure is to assess the variation of observation-simulation relationship by using the cross-validation method.

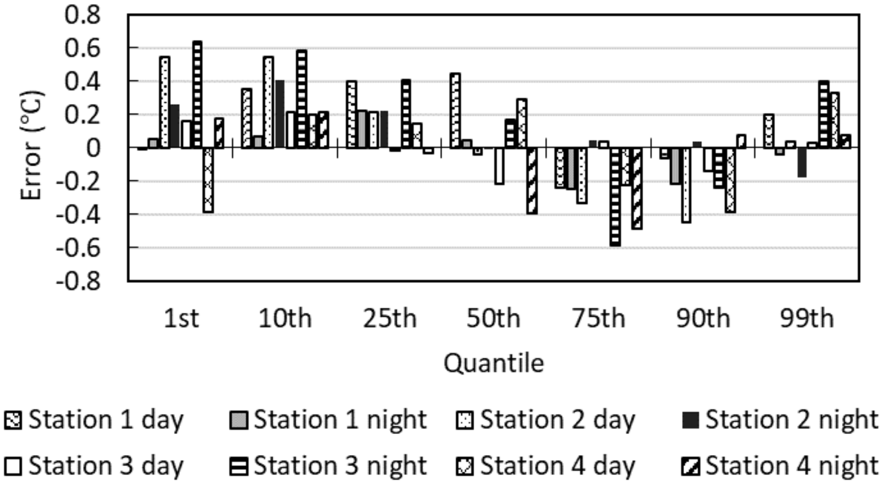

Figure 2.7 Errors in quantile of downscaled CMIP5 results relative to observations for four stations during the day (maximum daily temperatures) and at night (minimum daily temperatures). Positive values indicate overestimation, while negative values imply underestimation.

Cross validation has been employed by many studies to evaluate the performance of statistical forecasting models (Michaelsen 1987; Elsner and Schmertmann 1994; Kharin and Zwiers 2002; Stoner *et al.* 2013). Testing a prediction function on the same data that are used to determine the parameters for the function often yields a perfect score; however, the score cannot indicate anything for the function to predict using yet-unseen data. Cross validation solves this problem by randomly partitioning the original sample into four subsamples and designating two subsamples as the training data and the other two as the testing data. The training data are used to discover potentially predictive relationships, and the testing data are used to verify the relationships. Since testing data do no repeat the training data, the test results can reflect the forecasting capability of the developed function.

In this study, the time series of observation and simulation from 1965 to 2000 are selected as training datasets, and time series from 2001 to 2005 are testing datasets. Since downscaling models for the four stations have been created for the reference period 1965–2000, the developed piecewise regression functions are employed directly to downscale CMIP simulations during 2001–2005. The cross-validation error measures the difference between the downscaled model simulation and observation. Figure 2.8 presents the results of cross-validation errors for the four stations. All the errors are less than 8°C and most of them are less than 4°C. Compare Figure 2.7 and Figure 2.8, the cross-validation errors generally have no correlation with the fitting errors of downscaling models. Therefore, it is hard to say how fitting errors of downscaling models may affect future projections.

To further understand the cross-validation errors, Figure 2.9 plots the ranked observations and simulations during 1965–2000 and 2001–2005 for Station 1 at daytime and nighttime. The curves of two time periods almost overlap, though a minor shift can be observed at tails of the distribution. Overall, the above analyses prove that ARRM method is valid in downscaling CMIP5 daily simulation.

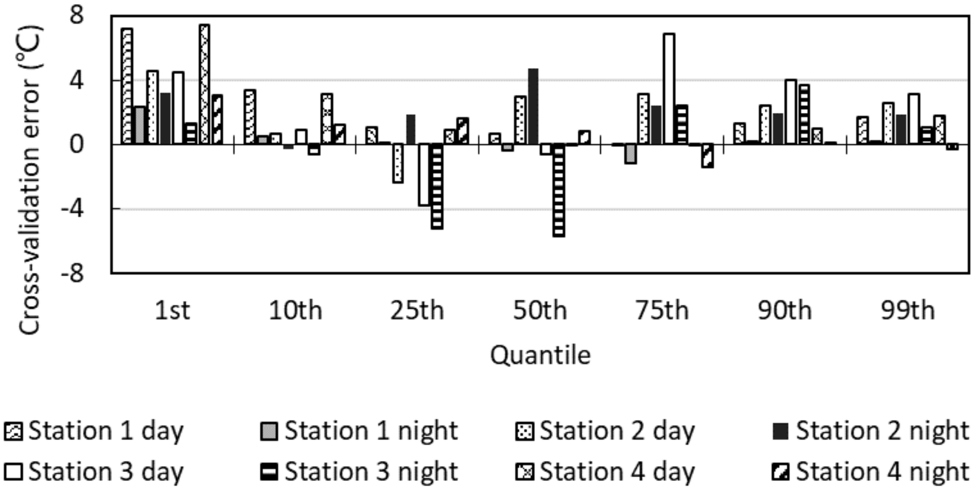

Figure 2.8 Cross-validation errors in quantile of projected 2001–2005 temperatures relative to observations for four stations during the day (maximum daily temperatures) and at night (minimum daily temperatures). Positive values indicate overestimation, while negative values imply underestimation.

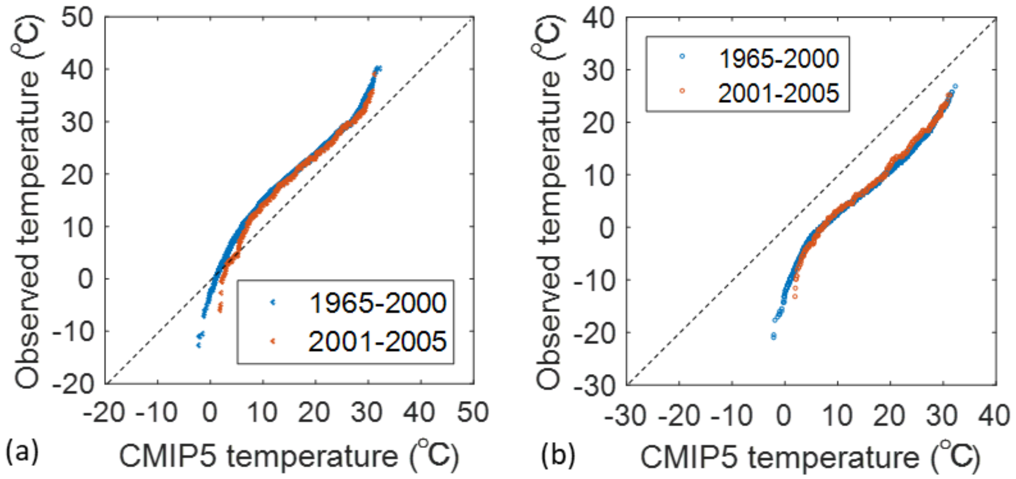

Figure 2.9 The shift of observation-simulation relationship in 2001–2005 relative to 1965–2000 at Station 1: (a) maximum daily temperatures; (b) minimum daily temperatures.

2.3.4 Projections for the UHI effect

The projected daily maximum and minimum temperatures in three time horizons: 2016–2035, 2046–2065, and 2086–2099 for the four weather stations are presented in Figure 2.10 and compared to the observation during 1965–2000. The temperatures projected for Stations 1 and 2 are averaged to obtain projections of Washington D.C., and the average temperatures of Stations 3 and 4 represent suburban projections. The seven quantiles of the 1st, 10th, 25th, 50th, 75th, 90th, and 99th correspond to extremely low, low, slightly low, mean, slightly high, high, and extremely high temperatures, respectively.

The similar trends of change can be observed in daily maximum and minimum temperatures (Figure 2.10). For scenario RCP 2.6, the temperature of Washington D.C. and its suburbs would keep at the same level in the next 80 years, but slightly greater than that of the reference period 1965–2000. The peak temperature (the 99th percentile) of the city would reach 40.9 °C during the day and 28 °C at night in 2086–2099. Scenario RCP 8.5 leads to a continually warming trend in the whole century. The peak temperature (the 99th percentile) of the city would rise to 48.2 °C during the day and 35.1 °C at night in 2086–2099. Overall, the projected trend for the temperature is consistent with the trend assumed for radiative forcing by climate scenarios.

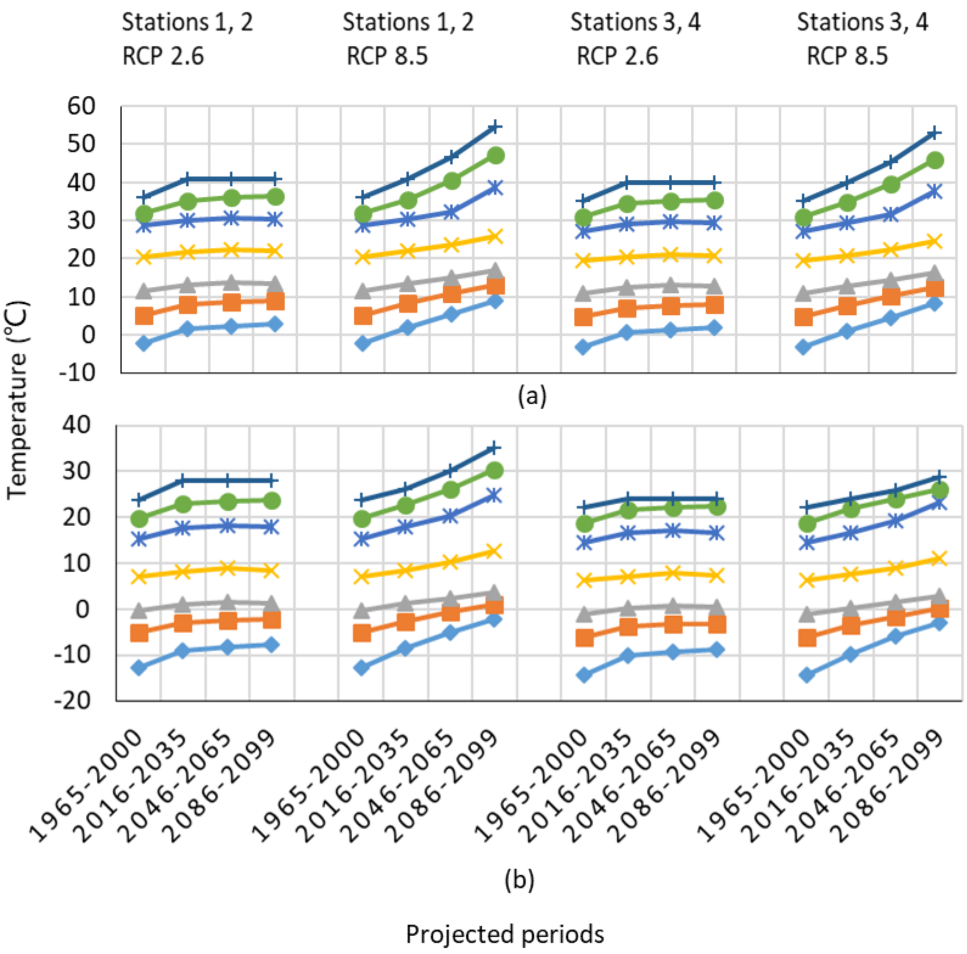

Figure 2.10 Projected temperatures in quantiles for three time horizons: 2016–2035, 2046–2065, and 2086–2099, and observed temperatures during 1965–2000: (a) maximum daily temperatures; (b) minimum daily temperatures.

The projected maximum UHI intensities for three time horizons: 2016–2035, 2046–2065, and 2086–2099 are presented in Figure 2.11 and compared to the observations during 1965–2000. UHI intensities are analyzed based on the quantiles of temperature distribution. Projections based on scenario RCP 2.6 indicate that UHI intensity would remain the same as the present, and daytime and nighttime UHI intensities would range between 1–2 °C and 1–3 °C in the next 80 years, respectively (Figure 2.11a and 2.11c). The range implies the variability of UHI intensities in the seven quantiles of temperature. Projections conducted for scenario RCP 8.5 suggest that the magnitude of UHI intensity would decline at low temperatures but rise at hot temperatures, especially at night (Figure 2.11b and 2.11c). UHI intensities at hot temperatures would grow continuously, and the growth is faster at hotter temperatures. Peak daytime and nighttime UHI intensities (at the 99th quantile of temperature) would reach 2.7 °C and 6.5 °C during 2086–2099, respectively. The projected UHI intensities based on the two scenarios are summarized in Table 2.2.

CMIP5 model ensemble considers the impacts of urban expansion on climate change from a general perspective. In those AOGCMs, urban expansion is indicated by the anthropogenic land-cover change that accounts for transitions between cropland, pasture, primary land, and secondary (recovering) land, the effect of wood harvest, shifting cultivation and urban land-use changes, and transitions from/to urban land. The value of land-cover change is updated every year for model inputs. For previous years (before 2006), the update relies on observations. For the future (since 2006), the update depends on projections made by climate scenarios. Scenarios RCP 2.6 and 8.5 result in different land-cover change due to different assumptions for radiative forcing. Overall, the downscaled CMIP5 projections reflect the impact of climate change on the temperature, and climate change is driven by a range of factors including urban expansion.

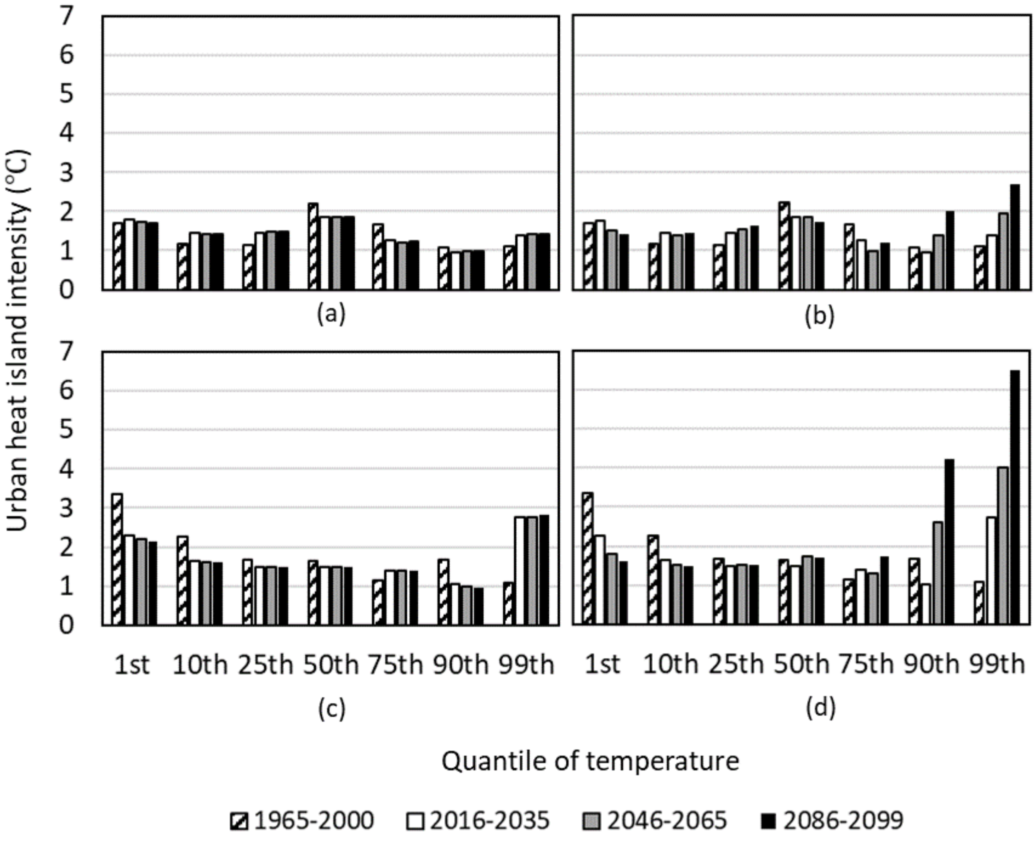

Figure 2.11 Projected UHI intensities in quantile of temperature for three time horizons: 2016–2035, 2046–2065, and 2086–2099, and observed UHI intensities during 1965–2000: (a) RCP 2.6 during the day; (b) RCP 8.5 during the day; (c) RCP 2.6 at night; (d) RCP 8.5 at night.

Table 2.2 Summary of the observed and projected UHI intensities.

	Quantiles						
Year	1st	10th	25th	50th	75th	90th	99th
Daytime UHI intensities (°C) based on RCP 2.6							
1961–2000	1.7	1.2	1.1	2.2	1.7	1.1	1.1
2016–2035	1.8	1.4	1.5	1.9	1.3	1.0	1.4
2046–2065	1.7	1.4	1.5	1.9	1.2	1.0	1.4
2086–2099	1.7	1.4	1.5	1.9	1.2	1.0	1.4
Daytime UHI intensities (°C) based on RCP 8.5							
2016–2035	1.8	1.4	1.5	1.9	1.3	1.0	1.4
2046–2065	1.5	1.4	1.5	1.8	1.0	1.4	1.9
2086–2099	1.4	1.4	1.6	1.7	1.2	2.0	2.7
Nighttime UHI intensities (°C) based on RCP 2.6							
1961–2000	3.4	2.3	1.7	1.6	1.2	1.7	1.1
2016–2035	2.3	1.6	1.5	1.5	1.4	1.1	2.8
2046–2065	2.2	1.6	1.5	1.5	1.4	1.0	2.8
2086–2099	2.1	1.6	1.5	1.5	1.4	1.0	2.8
Nighttime UHI intensities (°C) based on RCP 8.5							
2016–2035	2.3	1.6	1.5	1.5	1.4	1.0	2.7
2046–2065	1.8	1.5	1.5	1.7	1.3	2.6	4.0
2086–2099	1.6	1.5	1.5	1.7	1.7	4.2	6.5

Furthermore, precipitation is expected to increase in the future. Fall may experience the largest increase while winter precipitation would increase the smallest (USGCRP 2017). The cloud cover can amplify the UHI effect and result in higher value compared to this projection. In this study, the four stations are located within the same grid of CMIP5 simulation, and the same CMIP5 data are utilized to develop downscaling models and project temperatures. Due to different observation data, the observation-simulation relationships and thereby the projection results are different among the four stations. Therefore, the quality of observation data and the accuracy of the downscaling model dominate the reliability of projected UHI intensities.

2.4 Heat waves

2.4.1 Measurement of heat waves

Figure 2.12 presents the Cumulative Distribution Function (CDF) of daily maximum and minimum temperatures at Washington D.C. (Station 1) in the control period 1961–1990. The 90th percentile of maximum and minimum temperatures are 31.7 °C and 19.9 °C, respectively (Figure 2.12a and 12b). Therefore, a heat wave for Washington D.C. is defined as a spell of at least 6 consecutive days in which the maximum temperature exceeds 31.7 °C. Such definition allows identifying heat waves simply using temperature data, rather than estimating thermal stresses of humans to determine thermal indices (Matzarakis and Amelung 2008; Jendritzky and Tinz 2009), or collecting temperature, humidity, and regional information to calculate heat index (NWS, 1994; Robinson 2001; NWS 2016).

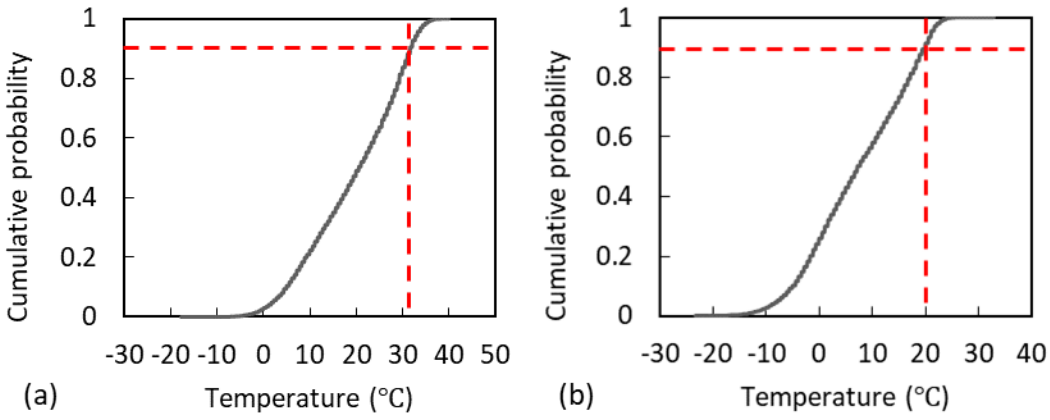

Figure 2.12 Cumulative Distribution Function (CDF) of temperature in Washington D.C. during 1961–1990: (a) maximum daily temperature: T_{90} = 31.7 °C and (b) minimum daily temperature: T_{90} = 19.9 °C.

Heat waves are usually characterized by temperature amplitude, the number of occurrences, and maximum duration (Fischer and Schar 2010; Anderson and Bell 2011). Furthermore, the Expert Team on Climate Change Detection and Indices (ETCCDI) proposed a set of climate change indices to measure and predict the evolution of extreme events (Sillmann *et al.* 2013a; Sillmann *et al.* 2013b). These indices have been published in IPCC reports (*e.g.*, IPCC 2013, IPCC 2014) for extreme weather and climate events analysis. Three of the indices related to heat waves are as follows:

- WSDI (warm spell duration index): defined as the annual count of days with at least 6 consecutive days in which the maximum temperature exceeds the 90th percentile (31.7 °C for Washington D.C.) of the base period 1961–1990. WSDI is affected by the frequency and length of heat waves.

- TX90p: defined as the percentage of calendar days in which the maximum temperature exceeds the 90th percentile (31.7 °C for Washington D.C.) for the base period 1961–1990. TX90p also refers to the annual percent of warm days.
- TN90p: defined as the percentage of calendar days when the minimum temperature exceeds the 90th percentile (19.9 °C for Washington D.C.) for the base period 1961–1990. TN90p also means the annual percent of warm nights.

Literature has indicated that the presence of warm nights is the main reason that results in excess mortality during heat waves (Grize *et al.* 2005) because warm nights prevent people from heat relief and keep people from sleep at night (Fischer and Schar 2010).

2.4.2 Observational analysis

The trend and variation of heat waves during 1961–2015 is shown in Figure 2.13 for Washington D.C. case. The maximum amplitude of the year without a heat wave is assigned a value of 31.7°C, which is the temperature threshold of a heat wave. During the 55 years, the maximum amplitude of heat waves shows a median growth of 0.025 °C per year, and the occurrence number shows a median increment of 0.017 per year. The maximum duration of a single heat wave also grew by about 0.1 days per year.

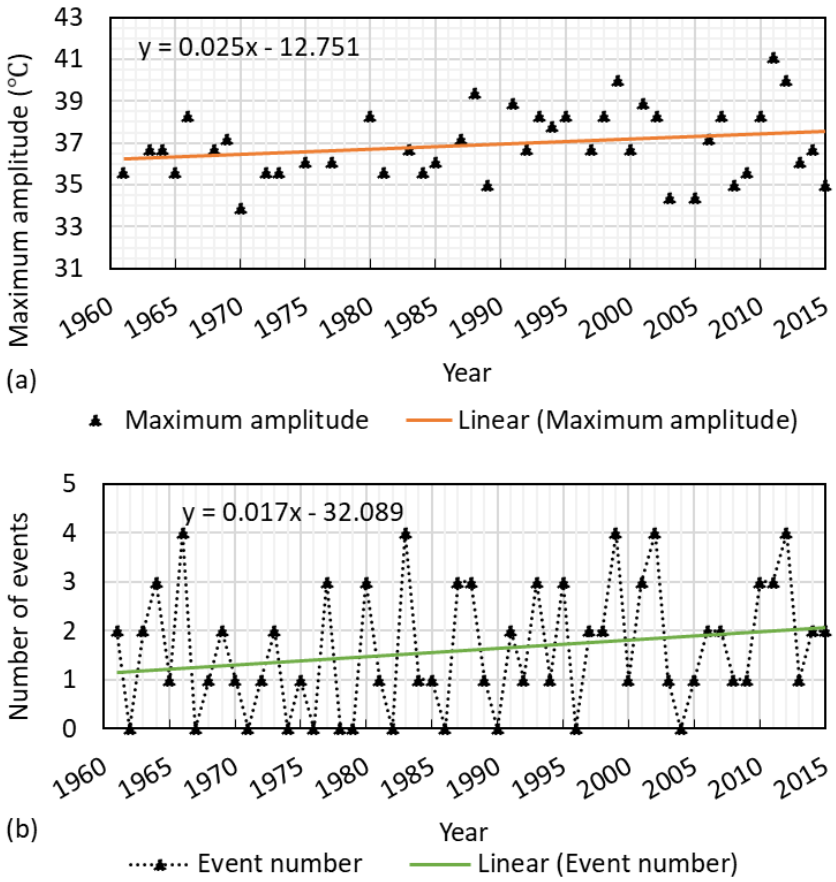

Figure 2.13 Observed maximum amplitude of heat waves and the number of occurrences in Washington D.C. (Station 1) during 1961–2015 and corresponding linear trend lines.

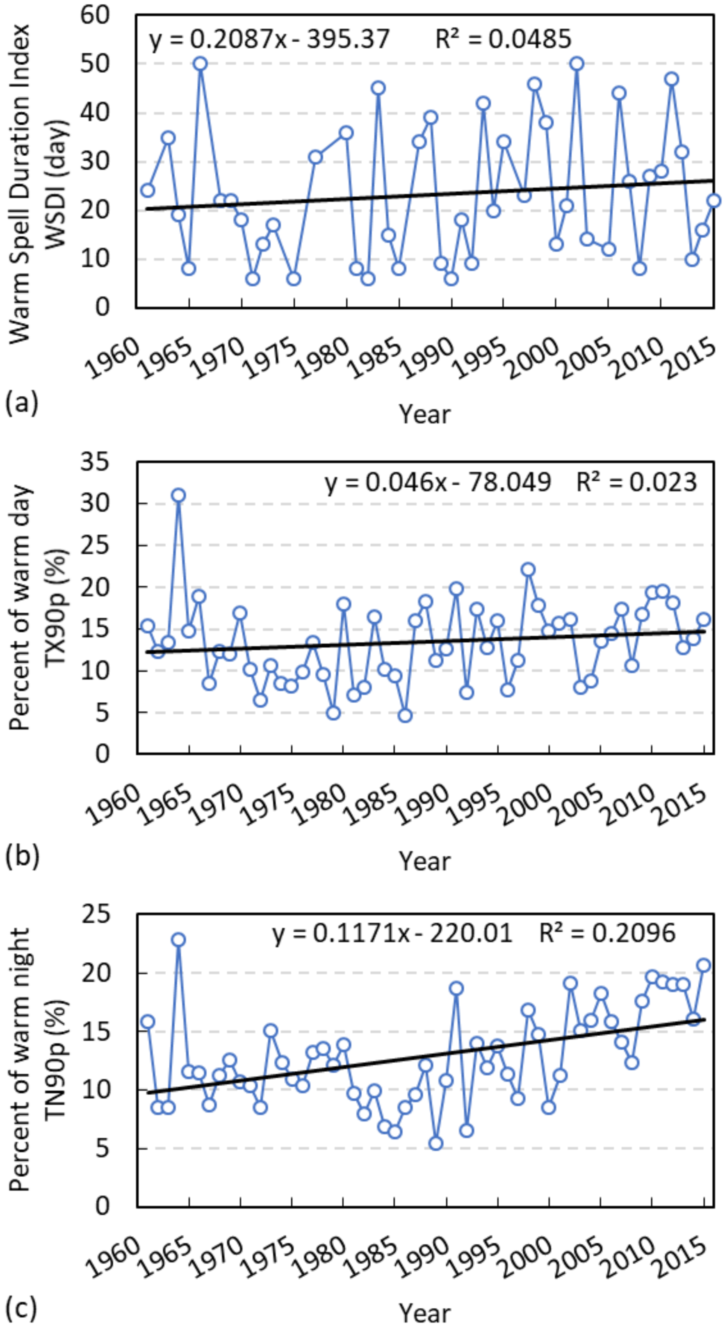

Figure 2.14 Observed extreme temperature indices of Washington D.C. (Station 1) during 1961–2015 and corresponding linear trend lines: (a) WSDI; (b) TX90p; and (c) TN90p.

Figure 2.14 shows the trends of the three extreme indices changing during 1961–2015 at Washington D.C. The median WSDI increased from 13.9 to 25.2 days, corresponding to an increment of 0.19 days per year (Figure 2.14a). The median TX90p grew from 12.2 % to 14.6 %, indicating an average increment of 0.04 % warm days per year (Figure 2.14b). The median TN90p rise from 9.5 % to 15.9 %, implying an average increase of 0.12 % warm nights per year (Figure 2.14c). The annual rate of warm nights (TN90p) grew faster than that of warm days (TX90p), which can be attributable to the UHI effect that slows the cooling process at night and makes nights warmer than usual (Zhou and Shepherd 2010).

2.4.3 Projections for heat waves

The downscaled CMIP5 projections for daily maximum and minimum temperatures are employed to predict heat waves and extreme temperature indices. Figure 2.15 presents projected heat waves at Washington D.C. (Station 1) in three time horizons: 2016–2035, 2046–2065, and 2086–2099. Projections of the single year are averaged to obtain the projections in the three periods. For scenario RCP 2.6, the maximum temperature amplitude would increase by 5 °C relative to the reference period 1996–2015 and keep at about 42 °C in the next eight decades (Figure 2.15a). The annual duration would double and peak in 2046–2065 (Figure 2.15c). For scenario RCP 8.5, a continuously growing trend is found for the heat waves. The maximum amplitude would increase by 15 °C relative to the reference period and reach 52 °C during 2086–2099 (Figure 2.15b). The annual duration would increase nearly threefold to 104 days during 2086–2099 (Figure 2.15d).

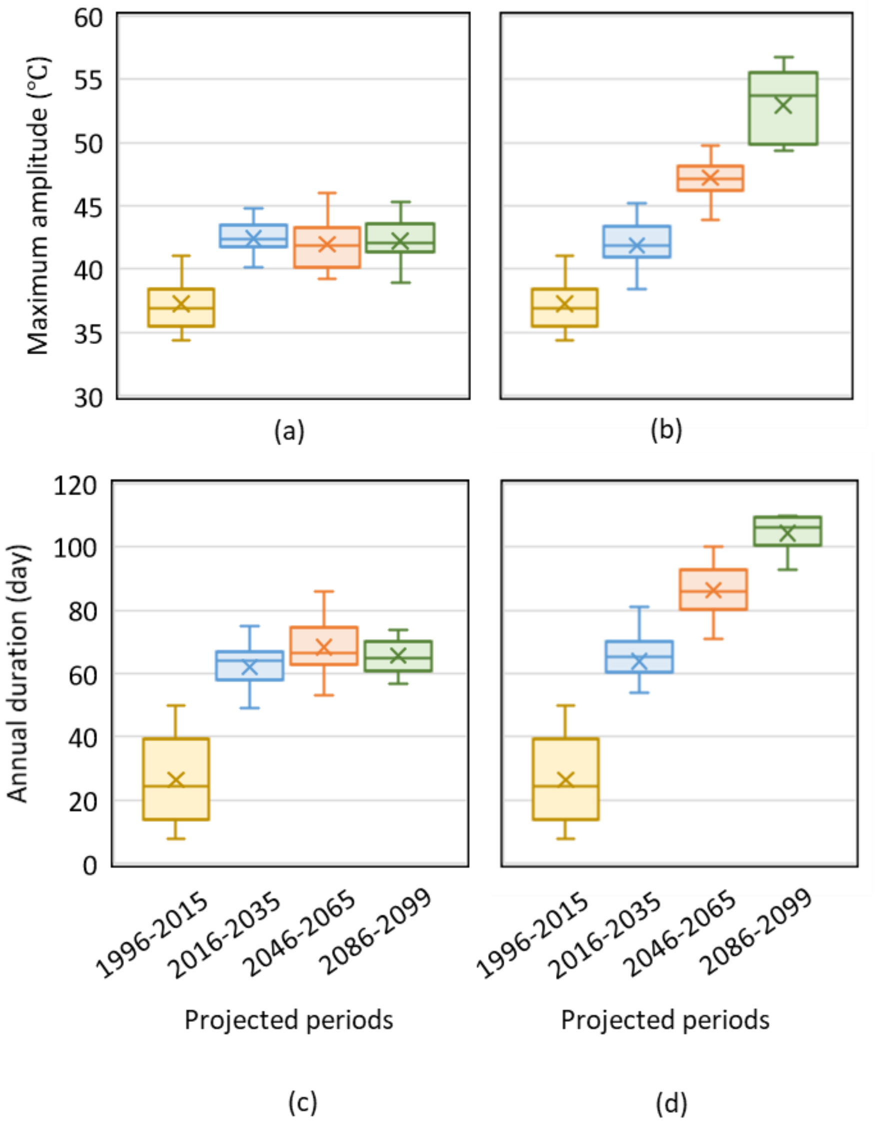

Figure 2.15 Projected heat waves of Washington D.C. (Station 1) in 2016–2035, 2046–2065, and 2086–2099, and observed heat waves in 1996–2015: (a) maximum amplitude based on RCP 2.6; (b) maximum amplitude based on RCP 8.5; (c) annual duration/WSDI based on RCP 2.6; and (d) annual duration/WSDI based on RCP 8.5. The cross “x” denotes mean; the top, middle, and bottom lines of the box represent 25, 50, and 75 quantiles, respectively; the top and bottom of whisker imply the minimum and maximum values, respectively.

The similar trend is observed in warm days and warm nights for the two scenarios, as shown in Figure 2.16. Projections based on scenario RCP 2.6 indicate that the annual percent of warm days and warm nights would peak in 2046–2065 and be 6% and 5% greater than that of the reference period, respectively (Figure 2.16a and 2.16c). Scenario RCP 8.5 results in a continually growing trend of warm days and warm nights in the whole century (Figure 2.16b and 2.16d). The mean values of TX90p and TN90p would double by the end of the century. The projected heat waves and extreme temperature indices based on the two climate scenarios are summarized in Table 2.3.

The frequency and maximum duration of heat waves are not investigated here. CMIP5 projections are the mean of ten AOGCMs' results, and thereby the variance of CMIP5 projections is less than that of single model's results, which results in consecutive hot days (daily maximum temperature greater than the 90th percentile) in the summer. Therefore, heat waves cannot be distinguished from each other based on the time series of projected temperatures. This also explains the fact that the projected annual duration of heat waves is much longer than the observed duration during the reference period.

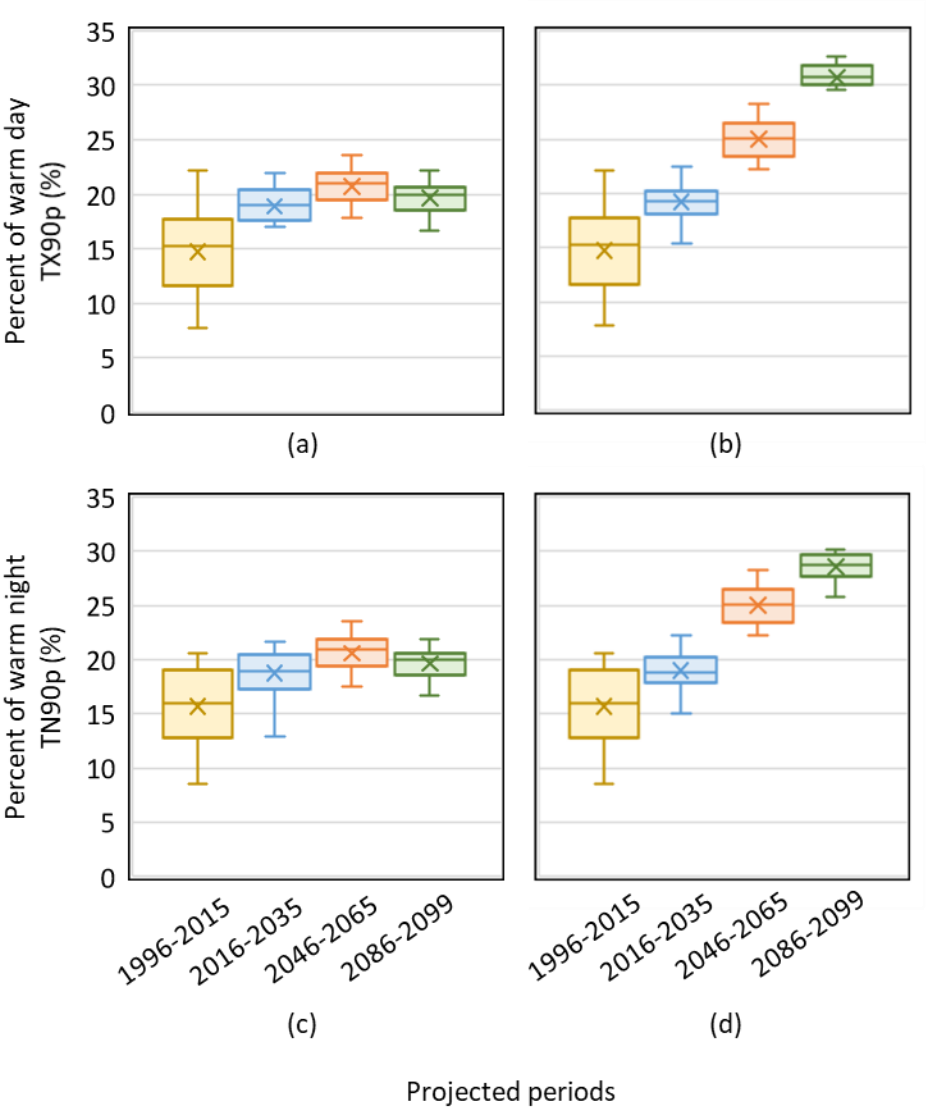

Figure 2.16 Projected extreme temperature indices of Washington D.C. (Station 1) in 2016–2035, 2046–2065, and 2086–2099, and observed indices in 1996–2015: (a) TX90p based on RCP 2.6; (b) TX90p based on RCP 8.5; (c) TN90p based on RCP 2.6; and (d) TN90p based on RCP 8.5. The cross "x" denotes mean; the top, middle, and bottom lines of the box represent 25, 50, and 75 quantiles, respectively; the top and bottom of whisker imply the minimum and maximum values, respectively.

Table 2.3 Summary of observed and projected mean (standard deviation) heat waves and extreme temperature indices.

Year	Maximum amplitude (°C)	Annual duration/ WSDI (days)	Percent of warm days/ TX90p (%)	Percent of warm nights/ TN90p (%)
Observed				
1996–2015	37.3 (2.0)[a]	26.5 (13.3)[a]	14.7 (3.9)	15.7 (3.5)
Projected for scenario RCP 2.6				
2016–2035	42.4 (1.5)	62.2 (8.7)	18.9 (2.1)	18.8 (2.1)
2046–2065	42.0 (1.9)	68.3 (8.0)	20.7 (1.6)	20.6 (1.6)
2086–2099	42.2 (1.7)	65.6 (5.7)	19.7 (1.6)	19.6 (1.4)
Projected for scenario RCP 8.5				
2016–2035	41.3 (1.6)	64.0 (9.6)	19.2 (1.8)	18.8 (2.1)
2046–2065	46.3 (2.1)	86.3 (8.1)	25.0 (1.9)	25.0 (1.9)
2086–2099	52.4 (2.5)	104.3 (5.8)	30.7 (1.5)	28.5 (1.3)

Note: [a] Only the year with at least one heat wave is counted.

2.5 Conclusions

This study proposes a method to project the UHI effect and heat waves by using statistical downscaling model, ARRM, that downscales CMIP5 projections to the locations of station-based observations. Three reliability measurements are taken to validate the proposed model. Results indicate the superior performance of the downscaling model in reproducing observed temperatures and temperature distributions. However, the errors of projection caused by the shift of the observation-simulation relationship are not treatable by statistical means and they require modeling the underlying physics which is outside the scope of the dissertation.

The trends and levels of the UHI effect and heat waves of Washington D.C. are projected based on two climate scenarios: the highest greenhouse gas concentration scenario RCP 8.5 and the lowest scenario RCP 2.6. For the next eight decades, projections of scenario RCP 2.6 indicate that UHI intensity would stay the same as the present, though the nighttime intensity may increase slightly at hot temperatures and decrease a little at low temperatures. Scenario RCP 8.5 suggests that UHI effect would be stronger at hotter temperatures, and weaker at lower temperatures, especially at nighttime. The UHI intensity at hot temperatures would increase continuously throughout the 21st century. The maximum amplitude and annual duration of heat waves would increase to the mid of the century and then decline slightly for scenario RCP 2.6. The same trend of change is found for warm days and nights. In contrast, projections based on scenario RCP 8.5 indicate that heat wave characteristics and warm days and nights would increase continuously in the whole century.

The contribution of this study consists of two parts. First, a new method is proposed to generate high-accuracy local UHI effect and heat wave projections. The downscaling model, ARRM, transforms data from global grid points to local station points by employing a set of statistical techniques, which produces high-accuracy projections and saves a large amount of computation resource. The CMIP5 data that combine solutions of multiple global climate models input to the downscaling model can ensure high accuracy of outputs. Using CMIP5 data also improves projection reliability because four climate scenarios are created to account for climate uncertainties in the future. Second, the future trends and levels of the UHI effect and heat waves characterized in this study reveals the rising impacts of global climate change on local communities and indicates the increased vulnerability of cities in the future. As for Washington D.C., the growing UHI intensity and heat wave characteristics in the future call for climate-change mitigation and adaptation efforts from both local governments and global collaborations.

Future work can use projection results of this study to assess the potential risks of urban systems exposed to extreme heat in a changing climate. All these works would help plan and initiate appropriate climate adaptations for cities.

Chapter 3: Projecting Heat Waves Temporally and Spatially for Local Adaptations in a Changing Climate: Washington D.C. as a Case Study

3.1. Introduction

Heat waves have become more frequent in the United States since the mid-1960s (USGCRP 2017). From the year 1999 to 2017, heat waves caused more than 7,500 deaths, greater than death tolls resulted from any other natural hazards in the United States (CDC 2018). Intensified heat waves lead to escalating electricity demand for space cooling, increased water consumption and water quality problems, and rising risks of asphalt melting, concrete hogging, and railway distortion, which threatens energy, water, and transportation systems (Zuo *et al.* 2015).

The increase of heat waves in metropolitan regions is attributable to both global climate change and local urban heat island (UHI) effect (Kalnay and Cai 2003; Tan *et al.* 2010; Basara *et al*. 2010; Li and Bou-Zeid 2013; Habeeb *et al*. 2015; Ortiz *et al.* 2018). Global climate change refers to the change induced by rising greenhouse gas concentration. Heat waves typically occur in summer when high-pressure weather conditions prevail, which can be measured by the height anomaly at 500 hPa. Meehl and Tebaldi (2004) indicated that the increase of greenhouse gases can lead to increased 500-hPa height anomaly over the contiguous United States. In addition, the UHI effect can prolong the duration of heat waves (Tan *et al.* 2010) and hinder cooling processes at night, causing excessive mortality during heat waves (Laaidi *et* *al.* 2012; Heaviside *et al*. 2016). Heat waves in turn enhance evaporative cooling in rural areas, increase heat emission from air conditioners, and inhibit air advection, exacerbating the UHI effect (Li and Bou-Zeid 2013; Zhao *et al.* 2018; Ortiz *et al.* 2018). Zhao *et al.* (2018) indicated that cities in temperate regions suffer greater from the synergistic interaction between UHI and heat waves compared to dry regions.

Washington D.C. experienced increased heat waves in past decades (Lombardo and Ayyub 2015; Zhang and Ayyub 2018), and its UHI effect is ranked the sixth among U.S. cities (Kenward *et al.* 2014). The local government has started to evaluate and address climate impacts on its community. The *Sustainable DC Plan* published in 2013 set a goal to reduce 50% and 80% of greenhouse gas emissions in the city by 2032 and 2050 respectively, relative to the emission level of 2006 (DOEE 2013). To achieve this goal, the government proposed to install more green roofs in addition to other measures. The adaptation plan *Climate Ready DC* released in 2016 highlighted the need to improve the resilience of infrastructure systems by utilizing cool roofs, green roofs, reflective pavements, and other technologies (DOEE 2016). Washington D.C. now installs the largest amount of green roofs in the nation (GRHC 2018). Therefore, investigating climate adaptation for Washington D.C. would potentially assist the sustainability practice of the city and provide guidance for other metropolises.

The goal of this study is to identify and reduce the vulnerability of cities, particularly Washington D.C., to increased heat waves. The first objective is to characterize the temporal and spatial variation of heat waves in the Washington DC metro area. The communities that have experienced heat waves may suffer from greater frequencies and intensities in the future (Meehl and Tebaldi 2004; Kunkel *et al.* 2010; Russo *et al*. 2014). With urban sprawling, the influence of heat waves may expand to new regions. The communities newly exposed to extreme heat can be vulnerable due to lack of experience and preparedness. Projecting heat waves would be important for identifying those susceptible regions and implementing appropriate adaptations for them.

The second objective is to quantify and predict the influences of UHIs and global climate change on heat wave growth. Comparing to accommodating cities to more extreme hot weather, mitigation has the advantages in addressing such a challenge from its root cause and enabling long-term risk reduction. Measuring the impacts of UHIs and climate change would help explore the mitigation potentials of heat waves from moderating the UHI effect and reducing greenhouse gas emissions, respectively.

The last objective is to evaluate heat wave mitigation strategies based on cool roof, green roof, and reflective pavement technologies. The three technologies have been extensively studied and tested in the current climate for UHI mitigation. Li *et al*. (2014) found that surface and near-surface UHI effect decreases almost linearly as cool and green roof fraction increase in the Baltimore, MD-Washington, DC metropolitan area. Santamouris (2014) indicated that a 0.1 increase in the albedo of cool roofs can lead to 0.1–0.33°C decrease of urban temperature, and applying green roofs on a city scale can reduce the overall temperature by 0.3–3°C. Santamouris *et al.* (2012) reported that using cool paving materials in a park (4500 m^2) of the greater Athens area can reduce summer peak temperature by 1.9°C and lessen pavement surface temperature by 12°C. However, the efficacy of these technologies may change when applied to a different environmental setting, especially under intensified future conditions. Increased hot temperature can elevate the evapotranspiration rate of green roofs and enhance their cooling efficiency. Increased precipitation may provide sufficient water to urban impervious surfaces and enhance evaporation there (Zhao *et al.* 2018). The enhanced evaporation can increase humidity, decrease vapor pressure deficit, and weaken the cooling capacity of green roofs. The performances of cool roofs and reflective pavements may decrease, as enhanced evaporation can increase cloudy days during heat waves. This study is distinguished from others by considering potential future circumstances, which would improve the understanding of these technologies employed in a dynamic environment.

The chapter is organized as follows. The next section describes the metrics of heat waves, model configuration, and experiments conducted in this study. The following two sections present projection results of heat wave characteristics and evaluation results of five mitigation strategies under assumed future climate conditions, respectively. The last section concludes the study and discusses uncertainties and the implications of the findings.

3.2. Model and methodology

3.2.1. Metrics of heat waves

Air temperature at two meters above the Earth's surface (2-m air temperature) can directly affect human thermal comfort (Anderson and Bell 2011) and building energy consumption (Akbari and Konopacki 2005). In addition, the Earth's surface temperature, also called surface skin temperature, is an important parameter for quantifying energy and water vapor exchanges between land/ocean and atmosphere. The 2-m air temperature and surface temperature are used in this study for heat wave analysis. The two temperatures are closely correlated but differ in magnitude, diurnal phase, and response to atmospheric conditions. Their difference is dependent on land cover (e.g., vegetation, asphalt, concrete) and sky conditions (e.g., clear or cloudy) (Jin and Dickinson 2010).

Heat waves are prolonged periods of excessive heat (Robinson 2001). This study defines a heat wave in Washington D.C. as at least six consecutive days in which daily maximum temperatures (2-m air temperature) exceeding the local 90th percentile (31.7 °C) of the control period from 1961 to 1990. This definition was employed by Fischer and Schar (2010) and recommended by the fifth report of the International Panel of Climate Change (IPCC 2013). To ensure the consistency of the analysis, this definition is applied to the nearby suburban and rural areas as well.

Heat waves are typically characterized by amplitude, frequency, and duration. Amplitude denotes the hottest temperature of a heat wave. Frequency measures the number of heat waves per year. Duration describes the length of a heat wave in days. In addition, warm spell duration (WSDI) counts the total number of heat wave days within a year, which is adopted by the fifth assessment report of the IPCC to evaluate and project the evolution of extreme heat events (Sillmann *et al.* 2013).

3.2.2. Model configuration

The Weather Research and Forecasting (WRF) model version 3.8 (Skamarock and Klemp 2008; NCAR 2017) is employed in this study to downscale Community Earth System Model version 1.0 (CESM1) data (Monaghan *et al*. 2014) for the Washington DC metro area. The variables in the CESM1 were bias-corrected by the National Center for Atmospheric Research (NCAR) using the European Centre for Medium-Range Weather Forecasts Interim Reanalysis (ERA-Interim) datasets. The ERA-Interim combines observations and numerical models to provide an estimate of the most likely current climate state (Dee *et al.* 2014). Komurcu *et al*. (2018) found that the CESM1 downscaled by the WRF model can provide a better match with observed mean and extreme temperatures compared to ERA-Interim. Krayenhoff *et al*. (2018) indicated that the CESM1 approximates the Fifth Coupled Model Intercomparison Project (CMIP5) mean in terms of summer temperatures. In this study, the bias-corrected CESM1 data are preprocessed using the WRF preprocessing system (WPS) and then input to the WRF model. The projections are forced by the Representative Concentration Pathway (RCP) 8.5, which is the ‘business as usual’ climate scenario and represents the highest concentration trajectory of greenhouse gases (IPCC 2013).

The WRF model utilizes a nesting technique to improve the resolution of climate simulation. The two-way nesting strategy is employed in this study to downscale solutions of the parent domain to the nested domain, and then to update the solutions of parent domains based on the results of the nested domain. This strategy can keep parent and nested domains consistent and minimize boundary reflections (Harris and Durran 2010). Four nested domains are created at a nest ratio of three (Figure 3.1), where Domain 3 covers the Washington DC metro area with a grid resolution of 4×4 km, and the Domain 4 includes Washington D.C. with a grid resolution of 1.3×1.3 km. The vertical dimension of the WRF model comprises 35 sigma vertical levels from the Earth’s surface to the 50 hPa pressure level. See the Appendix B for the vertical layers.

Table 3.1 lists the physical schemes employed in this study. Coupling the urban canopy model (UCM) with the Noah land surface model (LSM) in WRF can improve the accuracy of urban environment simulation (Chen *et al.* 2011). The single-layer UCM is adopted in this study to simplify urban spaces to 2-dimensional, infinitely-long, symmetric street canyons (Kusaka *et al.* 2001; Tewari *et al.* 2007), which is more suitable for weather forecasting compared to multilayer UCM, as fewer computing resources are required (Martilli *et al.* 2009). The land cover information is obtained from the National land cover database (NLCD) 2011 (Homer *et al.* 2015), where urban lands are categorized to high-density, medium-density, low-density, and open-space types (Figure 3.1). The low-density and open-space urban types of NLCD are merged into the low-density residential category of UCM. The high-density and medium-density urban types of NLCD are simulated as high-density residential and commercial categories in the UCM, respectively.

Table 3.1 Weather Research and Forecast (WRF) model setup and parameterization.

Model version	Advanced Research WRF (ARW) version 3.8
Duration	153 days from May 1 to September 30 for each year; 1-hour output frequency.
Grid spacing	36 km, 12 km, 4 km, and 1.33 km from the outermost domain to the innermost domain.
Physics	• Single-moment six-class microphysics scheme (WSM6); • Noah land surface model (LSM); • Single-layer urban canopy model (UCM); • Mellor-Yamada-Janjic (MYJ) planetary boundary layer (PBL) scheme; • Eta similarity surface layer scheme; • Rapid radiative transfer model (RRTM) for longwave radiation physics; • Dudiha scheme for shortwave radiation scheme; • Kain-Fritsch cumulus parametrization scheme.
Initial and boundary conditions	CESM1.0 Global Bias-Corrected CMIP5 datasets, 6-hour output frequency, grid cell resolution of 0.9×1.25 degree.

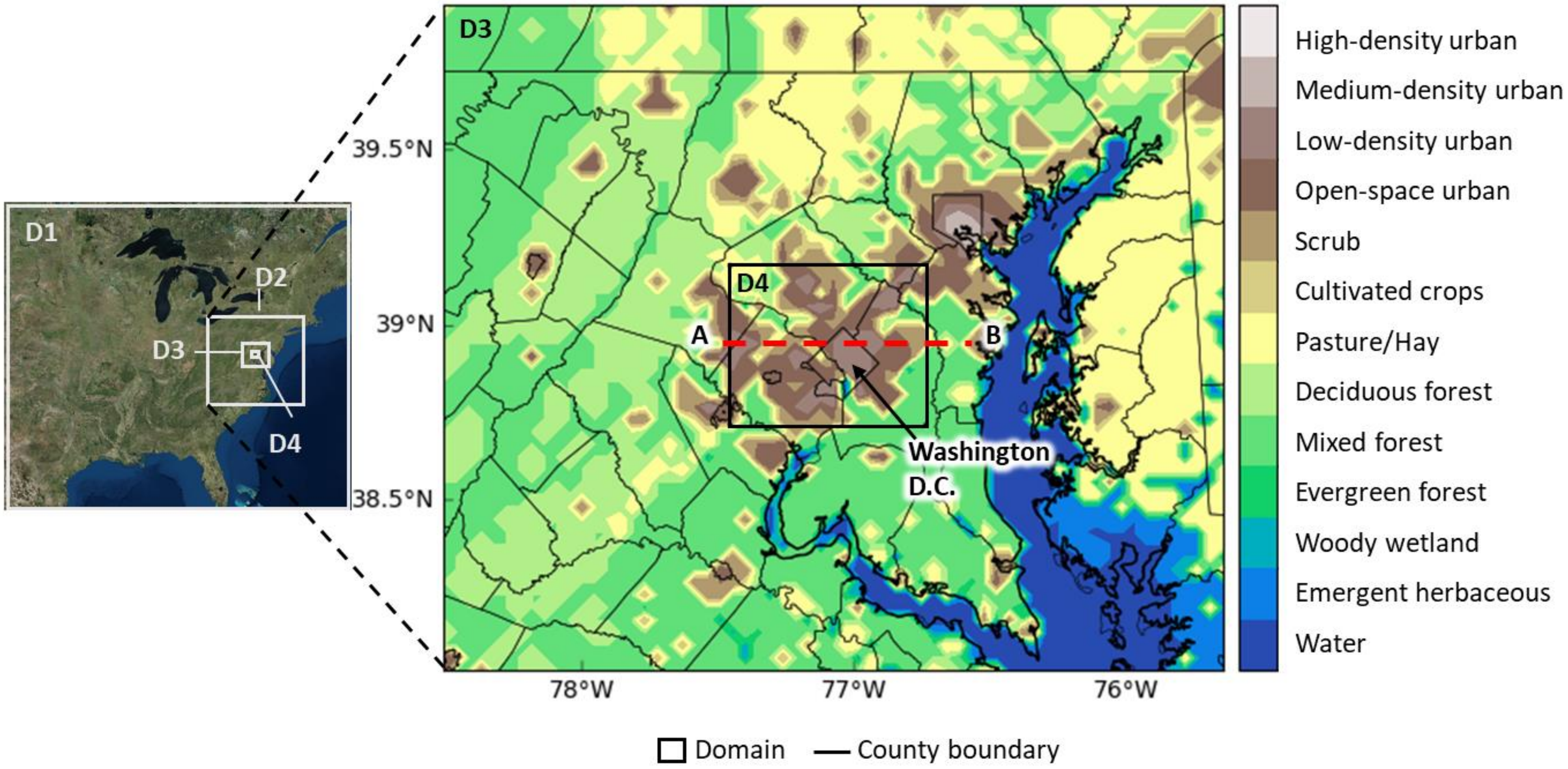

Figure 3.1 Four nest domains of the Weather Research and Forecast (WRF) model and National land cover database (NLCD) 2011 land use categories of Domain 3 (D3) and 4 (D4). Urban area refers to those where land use is high-density, medium-density, low-density, or open-space urban. The dashed line AB is the transect for studying the impacts of mitigation strategies.

The UCM parameters archived in the URBPARM.TBL file are revised for the Washington D.C. case, as shown in Table 3.2. The urban fraction and building height are determined based on the DC Zoning Regulations of 2016 Development Standards (DCOZ 2016) as follows:

- The zone districts of low-density residential land use category are occupied by single-family detached and semi-detached housing units that are no more than three stories. The height of three-story buildings is about 12.2 m, and a value of 9 m is used in the model, which is close to the height of a two-story building. The green area ratio should be at least 0.5.
- In the zone districts of high-density residential land use category, high-rise apartment buildings are in predominant use. High-rise apartments typically have eight stories or more, and the height of eight-story buildings is about 27.4 m. A value of 20 m is used in the model, considering there are some low buildings distributed in this zone. The green area ratio is required to be between 0.2 to 0.3.
- In high-density commercial areas, office and mixed office/retail buildings greater than eight stories are in predominant use. Building height of 25 m is used in the model to account for some low buildings, especially for some old buildings there. The green area ratio shall not be less than 0.2.

Table 3.2 Major parameters used in the single-layer urban canopy model (UCM).

Parameter	Unit	Commercial	High-density residential	Low-density residential
Urban fraction (impervious fraction)	%	80	70	50
Average building height	m	25	20	9
Building width	m	10	9.4	8.3
Road width	m	10	9.4	8.3
Surface albedo of roof		0.3	0.3	0.3
Surface albedo of wall		0.3	0.3	0.3
Surface albedo of pavement		0.15	0.15	0.15

The road width and building width employ the default values of UCM, which were used by Li and Bou-Zeid (2013) and Li *et al*. (2014) to simulate the UHI effect of Baltimore-Washington metropolitan area. In the UCM, both roofs and roads take up 45%, 35%, and 25% of commercial, high-density residential, and low-residential types of urban grid cells, respectively. The physical mechanisms for simulating 2-m air temperature are explained in the Appendix B.

3.2.3 Time slice experiment

This study projects heat waves in three time periods, 2036–2040, 2066–2070, and 2096–2100, to help foresee potential risks in the next twenty, fifty, and eighty years. The baseline period is 2011–2015. The WRF model is run at five-day intervals from May 1 to September 30 for each year, and the first day of each interval is reserved as a spin-up period to allow the initial conditions of the model to be thermodynamically balanced so as to generate stable and trusted results. The amplitude of heat waves is calculated as an average of the maximum amplitude in each year. Using maximum amplitudes instead of averages can avoid an overestimation of rural areas that have fewer heat waves. The duration of heat waves is averaged each year and then over five years. The frequency and warm spell duration are counted each year and averaged over five years. The characteristics of heat waves in Washington D.C. are measured on urban grid cells of Domain 4. Urban grid cells are those categorized by the NLCD as high-density, medium-density, low-density, or open-space types (Figure 3.1). The heat waves in rural areas are calculated on nonurban grid cells of Domain 3 excluding Domain 4. Water bodies (e.g., lake, river) are not considered in the analysis.

3.2.4 Mitigation technology experiment

Albedo is an indicator of surface reflectivity and its value ranges between 0 and 1. A high albedo means that a large amount of solar radiation is reflected, and a small amount is absorbed by the surface. Cool roofs, also called reflective roofs, are generally white-colored and of high albedo up to 0.9 for new roofs and 0.55–0.65 for aged roofs, while the albedo of conventional roofs is about 0.05–0.36 (Testa and Krarti 2017). Reflective pavements are either made of materials or covered in paint with high solar reflectivity or high infrared emittance (Santamouris *et al*. 2011). The albedo of reflective pavements varies between 0.20 and 0.80, dependent on material types and aging levels (Qin 2015). Green roofs, also termed living roofs, are partially or completed covered with vegetation and a growing medium over a waterproofing membrane, which can provide shading and evaporative cooling for buildings and the ambient environment (Santamouris 2014). The albedo of green roofs is close to the dry soil about 0.08–0.2 (Schwarz 2015). Five strategies based on above technologies are evaluated in this study as follows:

Strategy 1. Elevate roof surface albedo by 100%, denoted by AR100;

Strategy 2. Raise pavement surface albedo by 100%, denoted by AP100;

Strategy 3. Raise pavement surface albedo by 200%, denoted by AP200;

Strategy 4. Replace 50% conventional roofs with green roofs, denoted by GR50;

Strategy 5. Replace 100% conventional roofs with green roofs, denoted by GR100.

The values of UCM parameters are modified per strategy as demonstrated in Table 3.3. Green roofs are assumed to be irrigated every day to retain abundant moisture in the soil. The effectiveness of the five strategies in reducing heat wave amplitude and warm spell duration is assessed in three time periods, 2036–2040, 2066–2070, and 2096–2100, for Washington D.C. The simulation is run on a five-day period for the heat wave with the maximum amplitude in the five-year period (identified in the time slice experiment), called the hottest heat wave, using the WRF model with an output frequency of one hour.

This five-day period must include the peak day of the heat wave in order to measure the maximum amplitude after mitigation actions. Warm spell duration is computed on adjusted daily maximum temperatures. The adjustment subtracts the decline in the maximum amplitude of heat wave, contributed by each mitigation strategy, from daily maximum temperatures.

Table 3.3 Design of five UHI mitigation strategies.

Strategy	Parameters		
	Albedo of roof	Albedo of pavement	Green roof ratio
Reference	0.3	0.15	0
#1. Elevate roof surface albedo by 100%	0.6	0.15	0
#2. Raise pavement surface albedo by 100%	0.3	0.3	0
#3. Raise pavement surface albedo by 200%	0.3	0.45	0
#4. Replace 50% conventional roofs with green roofs	0.25	0.15	0.5
#5. Replace 100% conventional roofs with green roofs	0.2	0.15	1

3.2.5 Mitigation sensitivity experiment

This study further examines the performance of cool roofs and reflective pavements at different albedo levels, and the performance of green roofs with different replacement ratios. For cool roofs, the albedo levels of 0.3, 0.45, 0.6, 0.75, and 0.9 are analyzed. For reflective pavements, the albedo levels of 0.15, 0.3, 0.45, 0.6, 0.75, and 0.9 are assessed. For green roofs, the replacement ratio of 0, 0.25, 0.5, 0.75, and 1 are evaluated. The simulation is conducted on the hottest heat wave in the five-year period, which is the same as the mitigation technology experiment.

Moreover, this study examines the five strategies on less hot heat wave days to help understand the variability of mitigation effects. Three such days are selected from each year of 2096–2100 and compared to the peak day of the hottest heat wave. It should be noted that this experiment cannot reveal a mathematical relationship between mitigation effects and background temperatures, as many other natural factors (e.g., wind speed, humidity, solar radiation) that can affect mitigation effects are not identical in the samples.

3.3. Projection of heat waves

3.3.1. Model validation

The WRF model of the same physical schemes has been validated by several studies (e.g., Gao et al. 2012; Li and Bou-Zeid 2013; Li and Bou-Zeid 2014). This study further assesses the performance of the WRF model in reproducing heat waves by comparing simulation results against observations of 33 weather stations in the Washington metropolitan region for the period of 2011–2015 (Figure 3.2). Considering four climate scenarios resulting in similar pathways of temperature growth in the early 21st century, the simulation here based on the scenario RCP8.5 can represent the overall scheme of temperature change. Time series of observed temperatures are derived from NOAA daily summary database (NOAA 2017). The simulation errors for the average amplitude, average duration, and average warm spell duration of heat waves in the five-year period are presented in Figure 3.3. These average values are first computed each year and then averaged over five years. Table 3.4 provides more details for the comparison.

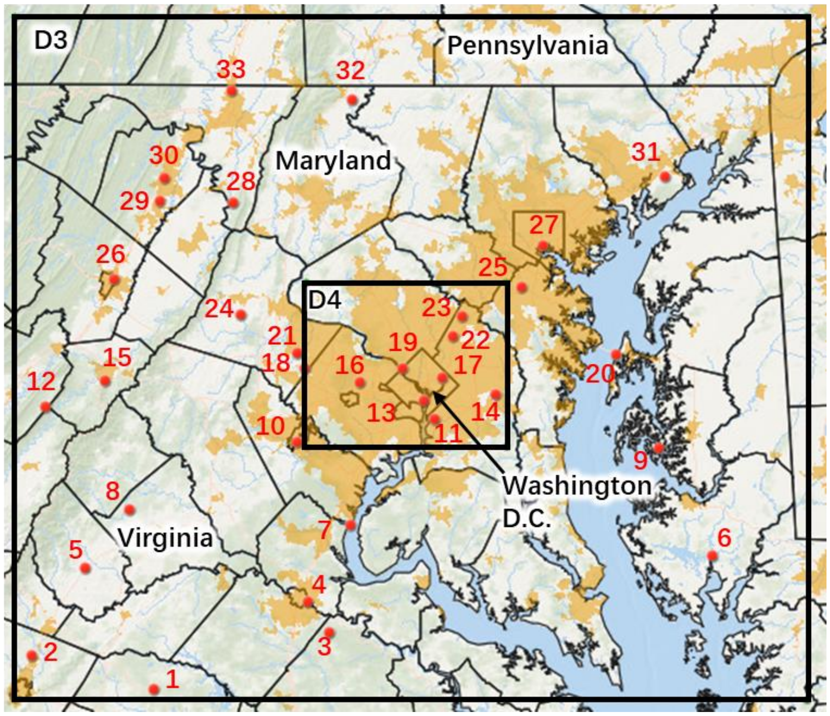

Figure 3.2 Spatial distribution of weather stations in nested Domain 3 (D3) and Domain 4 (D4). Red points denote stations. The orange areas are urbanized.

(a) 2011-2015 Average Heat Wave Amplitude

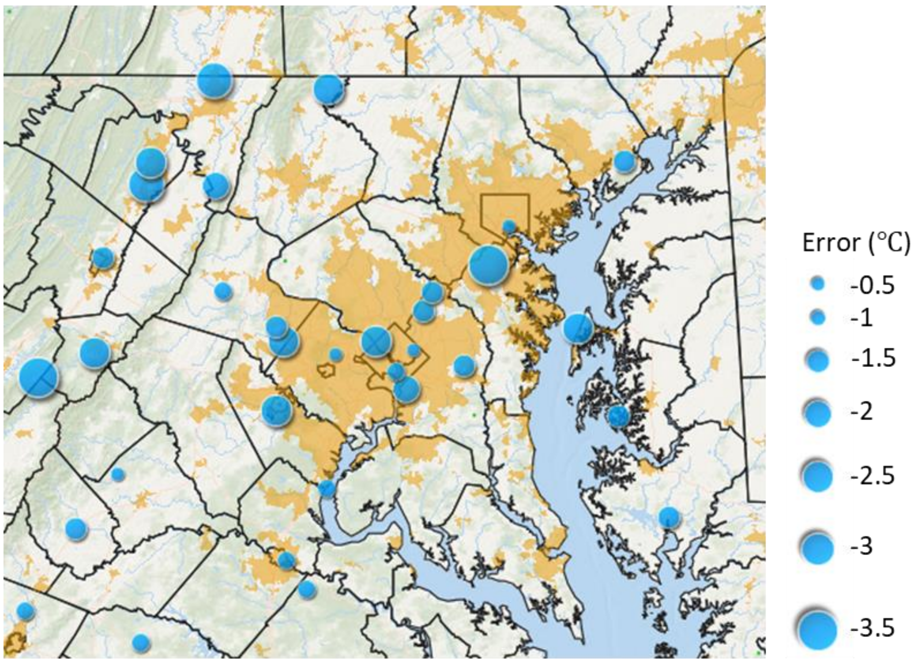

(b) 2011-2015 Average Heat Wave Duration

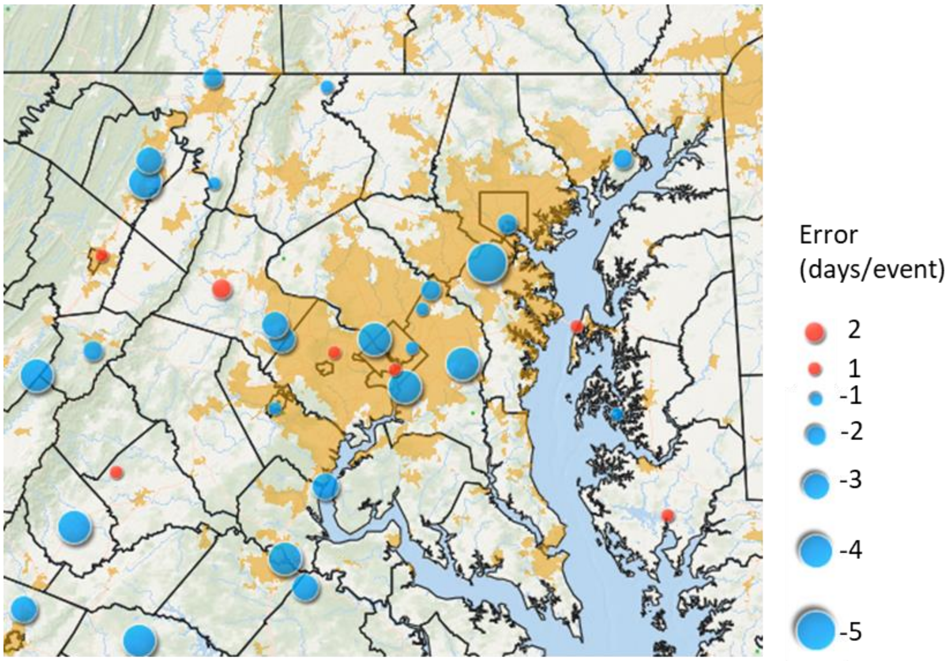

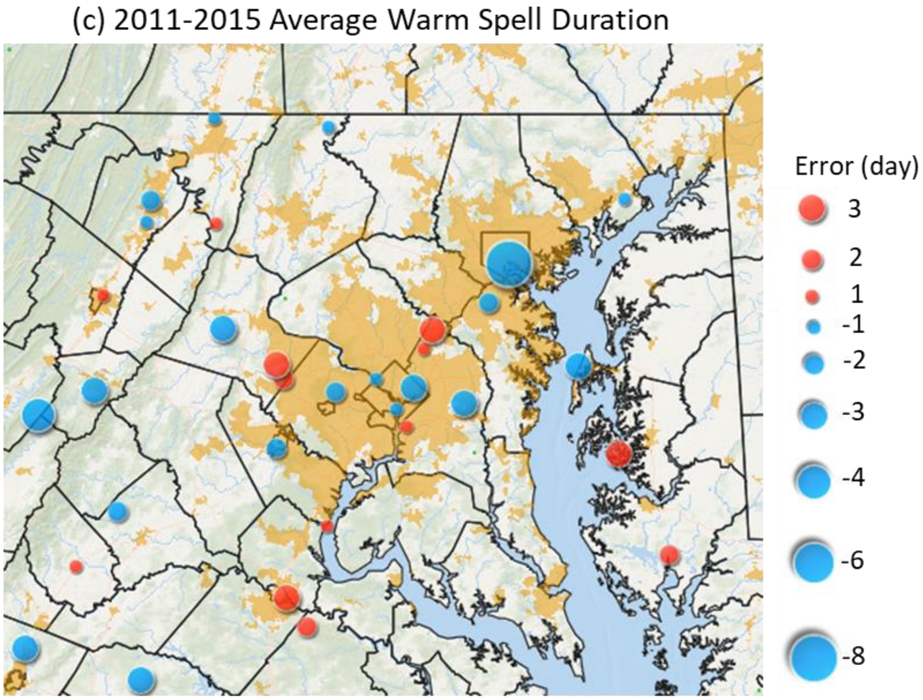
(c) 2011-2015 Average Warm Spell Duration

Figure 3.3 Simulation errors of (a) average heat wave amplitudes, (b) duration, and (c) warm spell duration. A positive value implies overestimation, and a negative value indicates underestimation.

Table 3.4 Observed and Weather Research and Forecast (WRF) model simulated heat waves in the Washington metropolitan region for the period 2011–2015.

Station ID	Observation			WRF model simulation						
	Average amplitude (°C)	Average duration (days/event)	Average warm spell duration (day)	Average amplitude (°C)	Error (°C)	Average duration (days/event)	Error (days/ event)	Average warm spell duration (day)	Error (day)
1	36.4	10.7	9.6	35.4	-1.0	7.5	-3.2	7.2	-2.4
2	36.1	10.8	11.0	35.5	-0.6	8.0	-2.8	8.0	-3.0
3	36.3	11.3	8.0	35.6	-0.6	8.4	-2.9	9.4	1.4
4	37.0	12.0	9.6	36.0	-1.0	8.7	-3.3	12.2	2.6
5	36.9	11.0	6.6	35.3	-1.5	7.5	-3.5	7.2	0.6
6	36.7	8.5	6.6	35.6	-1.1	8.8	0.3	8.2	1.6
7	36.7	11.0	11.8	36.0	-0.6	8.9	-2.1	12.6	0.8
8	36.4	6.5	5.4	36.1	-0.3	7.0	0.5	4.2	-1.2
9	37.3	9.0	7.2	36.0	-1.3	8.5	-0.5	10.2	3.0
10	38.0	9.2	11.4	35.8	-2.2	8.2	-1.0	10.2	-1.2
11	37.6	12.0	7.2	35.9	-1.7	8.4	-3.6	7.6	0.4
12	38.0	11.3	5.6	34.6	-3.4	8.0	-3.3	1.6	-4.0

Note: Positive errors indicate overestimation, and negative errors imply underestimation.

Table 3.4 Observed and Weather Research and Forecast (WRF) model simulated heat waves in the Washington metropolitan region for the period 2011-2015 (Continued).

Station ID	Observation			WRF model simulation					
	Average amplitude (°C)	Average duration (days/event)	Average warm spell duration (day)	Average amplitude (°C)	Error (°C)	Average duration (days/event)	Error (days/ event)	Average warm spell duration (day)	Error (day)
13	37.3	9.5	13.8	36.5	-0.8	10.4	0.9	13.6	-0.2
14	37.1	11.3	8.0	35.9	-1.2	7.7	-3.7	5.6	-2.4
15	36.2	7.3	7.0	35.8	-0.4	7.7	0.3	5.6	-1.4
16	36.6	8.2	5.2	34.3	-2.3	7.0	-1.2	2.8	-2.4
17	36.6	8.6	13.6	36.4	-0.2	8.4	-0.2	11.2	-2.4
18	38.3	10.7	8.0	35.9	-2.4	7.6	-3.1	7.2	-0.8
19	38.3	11.3	6.8	36.1	-2.2	9.0	-2.3	8.2	1.4
20	36.7	6.8	5.6	34.4	-2.3	7.5	0.7	3.0	-2.6
21	37.3	11.5	8.8	36.3	-1.1	9.1	-2.4	11.4	2.6
22	37.1	8.5	6.6	35.9	-1.2	7.6	-0.9	7.2	0.6
23	36.7	9.0	4.8	35.6	-1.1	7.6	-1.4	7.2	2.4
24	35.9	6.3	5.2	35.1	-0.8	7.5	1.2	3.0	-2.2

Note: Positive errors indicate overestimation, and negative errors imply underestimation.

Table 3.4 Observed and Weather Research and Forecast (WRF) model simulated heat waves in the Washington metropolitan region for the period 2011-2015 (Continued).

Station ID	Observation			WRF model simulation					
	Average amplitude (°C)	Average duration (days/event)	Average warm spell duration (day)	Average amplitude (°C)	Error (°C)	Average duration (days/event)	Error (days/ event)	Average warm spell duration (day)	Error (day)
25	39.1	12.0	7.2	35.9	-3.2	7.7	-4.3	6.0	-1.2
26	36.1	6.3	3.8	34.7	-1.4	6.8	0.5	4.2	0.4
27	37.1	11.0	15.6	36.9	-0.2	9.2	-1.8	7.0	-8.6
28	36.9	8.2	6.4	35.2	-1.8	7.7	-0.5	6.8	0.4
29	38.0	10.7	5.2	35.3	-2.6	7.3	-3.3	4.4	-0.8
30	37.7	8.7	6.8	35.4	-2.3	6.5	-2.2	5.0	-1.8
31	37.4	10.0	4.8	35.9	-1.5	8.0	-2.0	4.6	-0.2
32	36.7	6.5	2.6	34.7	-2.0	6.0	-0.5	2.4	-0.2
33	38.1	8.0	3.2	35.1	-3.0	6.5	-1.5	2.6	-0.6

Note: Positive errors indicate overestimation, and negative errors imply underestimation.

Observing Figure 3.3, heat wave amplitudes are underestimated by the WRF model by 0.2–3.4°C. This indicates that the WRF model may not perfectly capture extreme hot temperatures, which is a common issue of climate models. The error in simulating heat wave duration ranges between -4.3 and 1.2 days/event, and there is no clear rule for overestimation or underestimation. The error in simulating warm spell duration varies between -3.0 and 3.0 days. The greatest error appears in Station 27 (-8.6 days), which is largely attributable to two reasons. First, the UCM is developed based on the zone regulation of Washington D.C., which may not precisely describe other urban areas. Station 27 is in Baltimore, MD, where buildings are denser and taller, and human activities are greater compared to Washington D.C. Second, the grid cell where Station 27 is located contains river, and the temperature of the river is significantly lower than that of the land, which reduces the average temperature simulated in the grid cell. Overall, the accuracy of the WRF model is sufficient for this study.

3.3.2. Projection results and discussion

Figure 3.4 presents projected heat wave amplitude and warm spell duration in three future periods for the Washington metro area. Higher intensity and longer duration of heat waves are expected in the rest of the century, and urban areas tend to experience hotter and longer heat waves compared to rural areas. Table 3.5 summarizes the mean and maximum values of heat wave characteristics in Washington D.C., which reflects the joint effect of climate change and UHI on heat wave evolution. The mean amplitude of heat waves may increase by 0.3–0.4°C per five years and can be 5.7 °C higher relative to the baseline (2011–2015) level by the end of the century. The warm spell duration may rise by 2.3–3.3 days per five years and can be nearly two-month-long by 2100, implying that the annual number of days with maximum temperatures above 31.7°C can be greater than two months by 2100. Although the mean frequency of heat waves may decrease in the second half of the century because of the increased mean duration, heat waves are expected to occur three times more often in 2096–2100. Mean duration of heat waves can be three times as much by 2100. The same pattern is shown in the maximum values of heat wave characteristics, implying that urban and rural areas may suffer from a similar increase of intensities and frequencies.

Projection results are compared between Washington D.C. and rural areas to assess the impact of UHI on heat wave growth. Figure 3.5 compares the probability distributions of heat wave amplitudes between the city and its surroundings. Although a small portion of two distributions is overlapped, the difference between the two is substantial. Table 3.6 summarizes the increase in heat wave characteristics contributed by the UHI effect. The influence of UHI is more striking on heat wave duration and warm spell duration compared to heat wave amplitude and frequency. Comparing Table 3.6 to Table 3.5, one can find that climate change dominates the growth of heat waves in Washington D.C. while UHI further intensifies the shift. The UHI may contribute to four-fifth, half, and one-fifth of the increment in warm spell duration in the next twenty, fifty, and eight years, respectively. Climate change would lead to the rest portion of the increment.

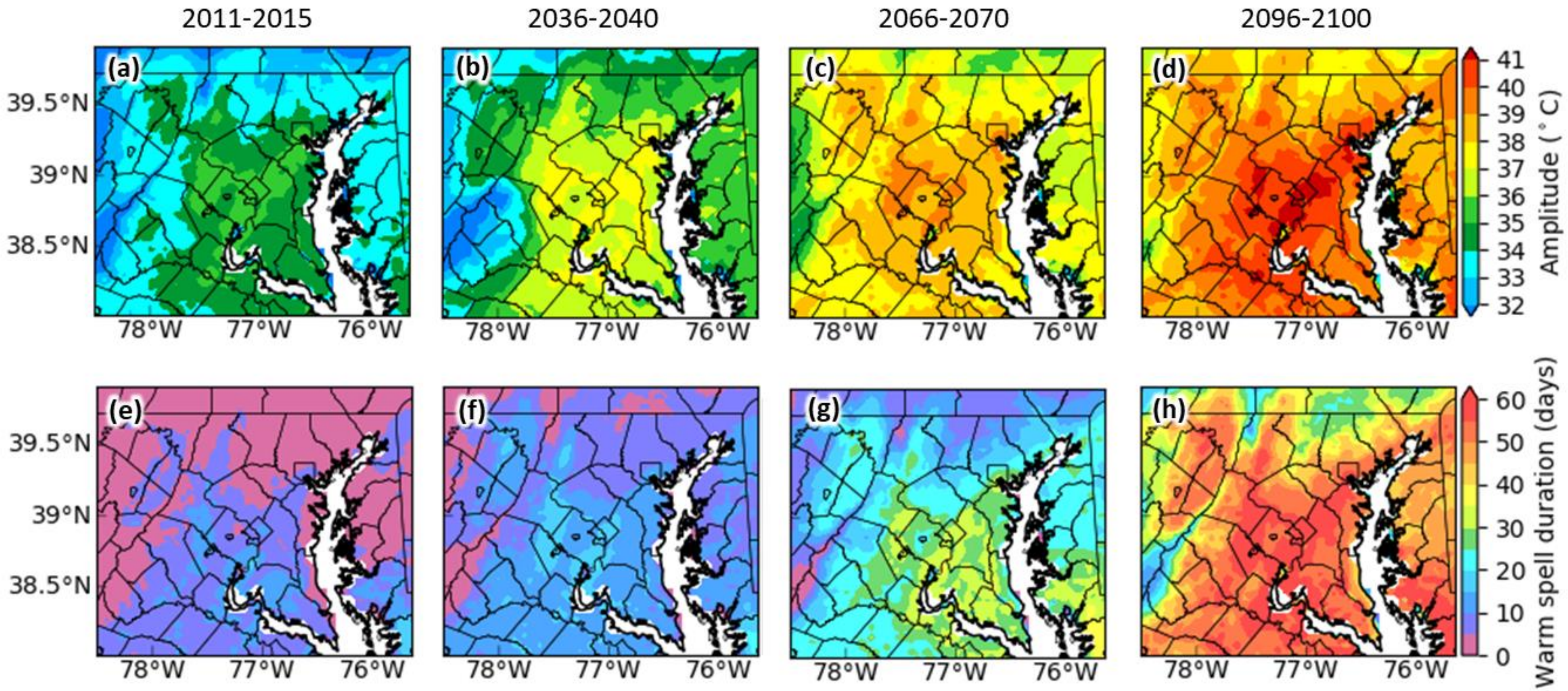

Figure 3.4 Variation of heat waves in Washington metropolitan region during the reference period, 2011–2005, and three future periods, 2036–2040, 2066–2070, and 2096–2100, plotted at 4-km grid intervals. (a)-(d) Heat wave amplitude; (e)-(h) Warm spell duration. The black lines are county boundaries, and the white area is waters.

Table 3.5 Heat wave characteristics in Washington D.C.

Characteristics	Period			
	2011–2015	2036–2040	2066–2070	2096–2100
Mean (Standard deviation)				
Amplitude (°C)	35.2 (0.3)	37.1 (0.3)	39.0 (0.3)	40.9 (0.4)
Frequency (events/year)	0.9 (0.3)	2.0 (0.3)	4.2 (0.3)	3.1 (0.2)
Duration (days/event)	8.0 (0.7)	9.1 (0.6)	10.0 (1.6)	25.5 (1.2)
Warm spell duration (days)	7.0 (2.3)	18.3 (3.0)	41.3 (5.2)	56.2 (2.7)
Maximum				
Amplitude (°C)	35.9	37.8	39.9	41.8
Frequency (events/year)	1.6	2.8	5.2	3.6
Duration (days/event)	10.8	11.5	14.7	27.5
Warm spell duration (days)	14.2	26.8	51.6	64.2

Note: The ‘mean’ implies the mean value over thousands of urban grid cells in Domain 4. The ‘maximum’ denotes the maximum value of urban grid cells in Domain 4.

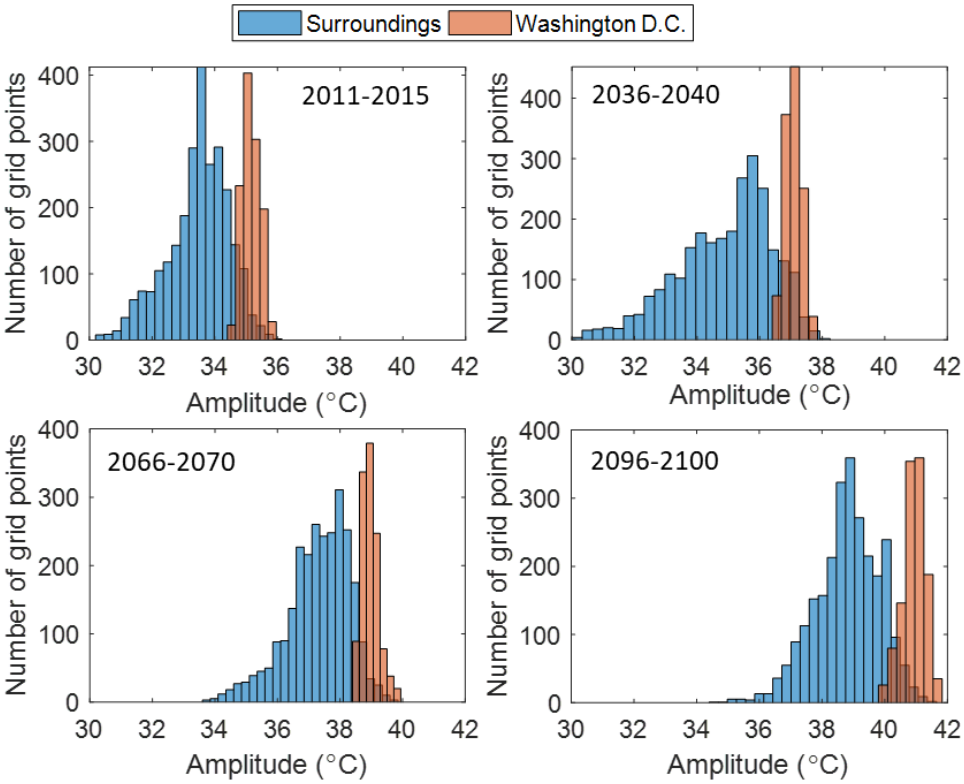

Figure 3.5 Histograms of heat wave amplitudes in Washington D.C. and its surroundings during the reference period 2011–2015, and three future periods 2036–2040, 2066–2070, and 2096–2100.

Table 3.6 The mean difference of heat wave characteristics between Washington D.C. and its surroundings.

Characteristics	Period			
	2011–2015	2036–2040	2066–2070	2096–2100
Amplitude (℃)	1.69	2.19	1.65	2.11
Frequency (events/year)	0.32	0.70	1.15	-0.11
Duration (days/event)	1.32	0.32	0.66	10.60
Warm spell duration (days)	2.32	9.04	18.42	12.08

Note: The 'mean difference' refers to the difference of mean values in the distributions of Washington D.C and its surroundings.

3.4. Evaluation of mitigation strategies

3.4.1. Evaluation results and discussion

Figure 3.6 shows the impacts of five mitigation strategies on heat wave amplitude and warm spell duration at Washington D.C. Cool roof (AR100) and green roof (GR50 and GR100) strategies may be slightly less effective in reducing heat wave amplitude in the future (Figure 3.6a). while the opposite trend is true for reflective pavement strategies (AP100 and AP200). This is attributable to increased Earth's net radiation as a result of future increased greenhouse gases, which amplifies sensible heat transmitting to the air. Increased sensible heat warms the near-surface atmosphere and elevates evapotranspiration rate of green roofs. However, increased radiative heating is greater than enhanced evaporative cooling, the temperature reduced by green roofs may decrease. Cool roofs and reflective pavements reflect sunlight and lessen heat absorption of urban surfaces. In this simulation, solar radiation increases over the three analysis periods, as the hottest heat wave tends to occur earlier in summer (closer to summer solstice). This can lead to increased cooling effects of cool roofs and reflective pavements. However, cool roofs and reflective pavements can weaken evaporative cooling over urban surfaces, and increased temperature can intensify such impact. When reduced radiative heating overpasses decreased evaporative cooling, temperature reduction increases, which applies to reflective pavements. Cool roofs are the opposite case.

Although there is no evaporation on cool roofs and reflective pavements, they can affect the evaporation of vegetation fraction in cities. The reduced solar radiation leads to decreased sensible heat in the low-level atmosphere, which cools low-level atmosphere, increases atmospheric stability, and results in less growth of the boundary layer. Since advective winds from moist rural regions are closer to the surface, they can interact more directly with the surface, increase humidity in the urban atmosphere, and ultimately reduce vapor pressure deficit and evaporative capacity over urban areas. Figure 3.7 shows the vertical profile of temperature and humidity when cool roof strategy (AR100) is taken on the peak day of the hottest heat wave in 2096–2100. Urban areas are in the middle of each plot, where low-level atmosphere temperature is lower and high-level atmosphere temperature is higher than that of the reference case (Figure 3.7a). This indicates the less growth of the boundary layer due to mitigation actions. Humidity is greater at low-level atmosphere compared to the reference case (Figure 3.7b), which explains the reason for reduced evaporation. Li *et al*. (2014) and Sharma *et al*. (2016) have found similar results when investigating cool roofs and green roofs as UHI mitigation strategies.

Figure 3.6a illustrates that elevating albedo of urban roofs by 100% can lead to 0.6–0.8°C decline in heat wave amplitude, while raising urban pavement albedo by 100% or 200% has a negligible effect. Green roofs show a better performance in heat wave mitigation compared to cool roofs and reflective pavements. Replacing conventional roofs with 50% and 100% green roofs can reduce heat wave amplitude by 0.5–0.7°C and 0.9–1.3°C, respectively. Figure 3.6b shows that the greatest decrease in annual warm spell duration is in 2066–2070 among the three periods. This is because annual warm spell duration in 2036–2040 is one half of that in 2066–2070, which limits the reduction potential. In addition, the amplitudes of heat waves in 2096–2100 are greater than those of 2066–2070 while amplitude decline is similar (Figure 3.6a). Elevating albedo of urban roofs by 100% can reduce warm spell duration by 6–9 days, while raising urban pavement albedo by 100% or 200% can result in less than 3 days of decline (Figure 3.6b). Increasing green roof fractions by 50% and 100% can lessen warm spell duration by 5–8 and 9–13 days, respectively (Figure 3.6b). The impacts of five mitigation strategies on surface temperatures are similar and depicted in Appendix B.

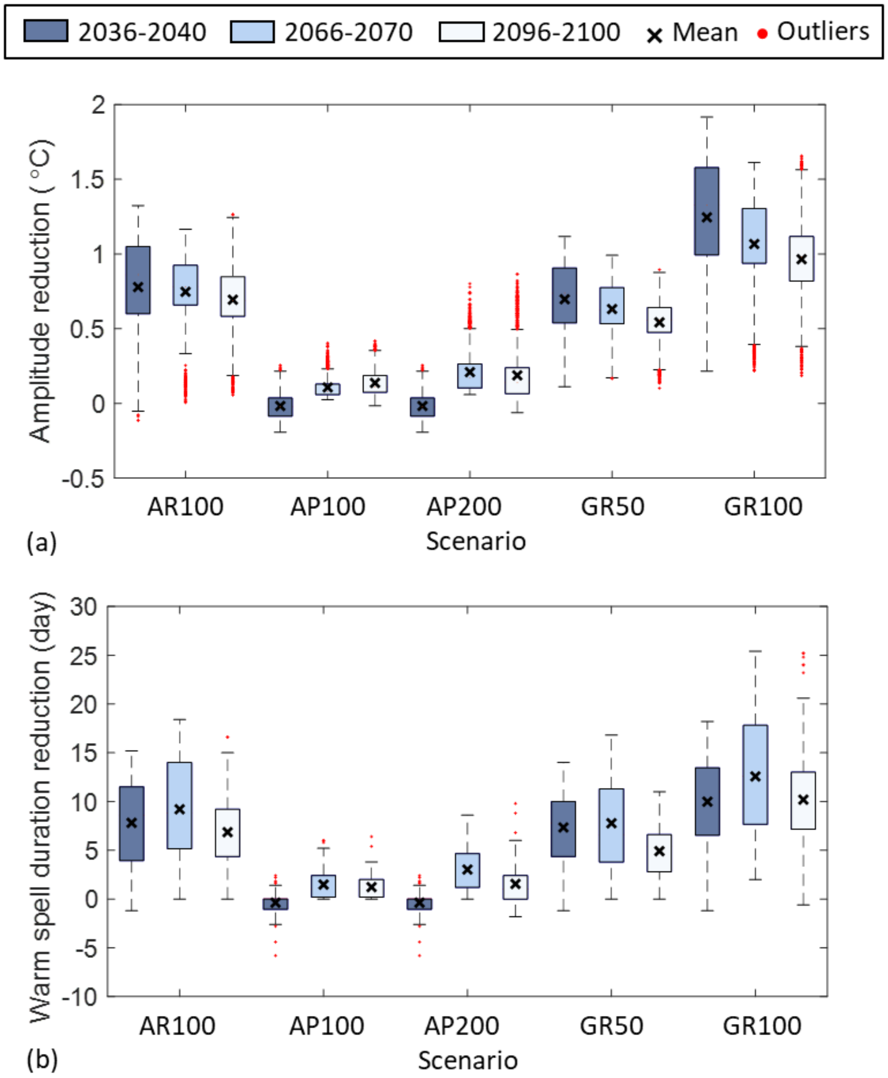

Figure 3.6 Impact of five mitigation strategies on heat waves in Washington D.C. for three time periods, 2036–2040, 2066–2070, and 2096–2100. (a) Reduced amplitude of the hottest heat wave; (b) Reduced warm spell duration. All results are averaged over urban grid cells in Domain 4. The top and bottom of each box are the 25th and 75th percentiles. Whisker corresponds to approximately +/–2.7σ and 99.3 percent coverage. Values beyond the whisker length are marked as outliers.

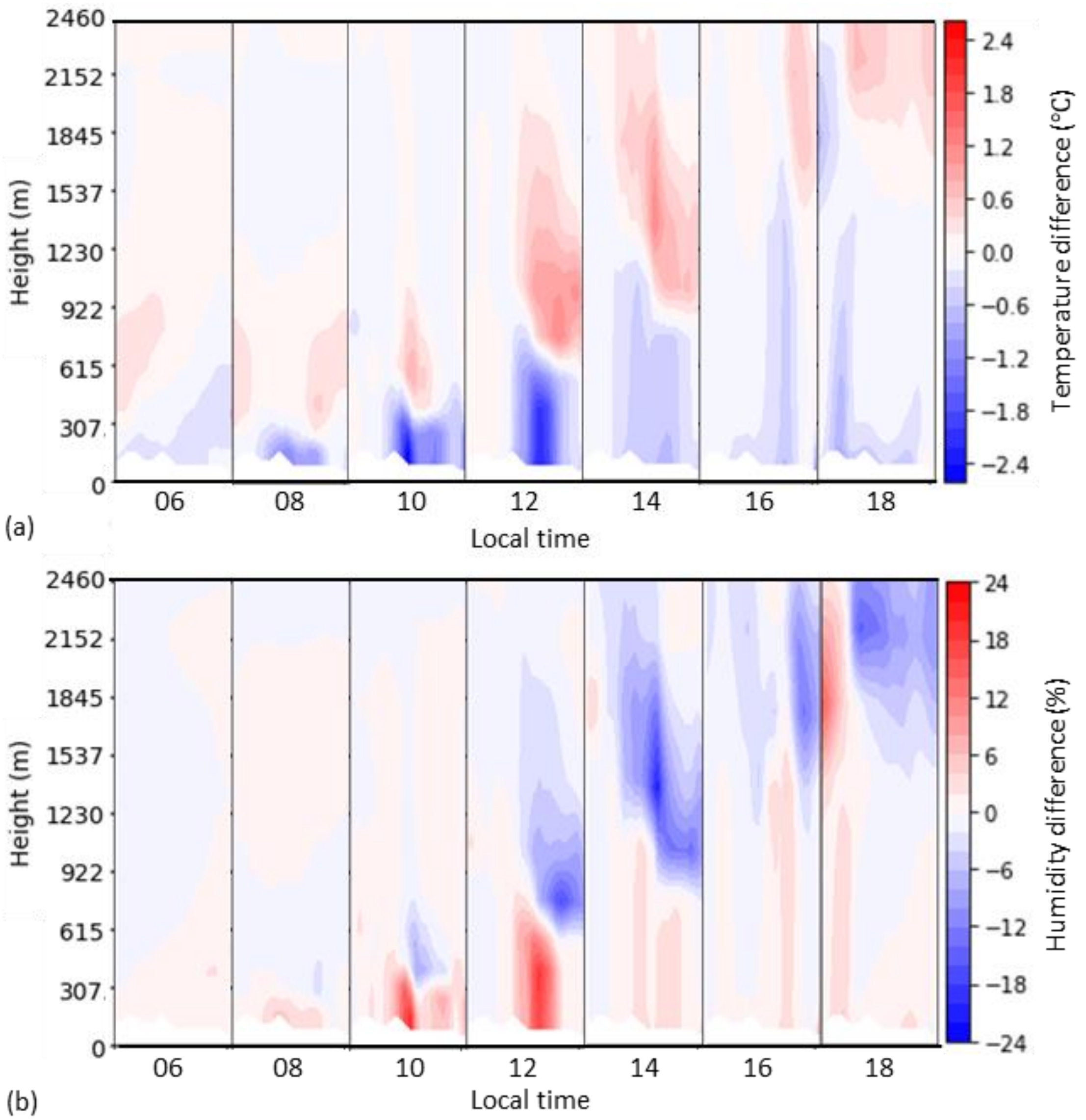

Figure 3.7 Impacts of cool roof strategy (AR100) on the vertical profile of temperature and humidity (Transect AB in Figure 3.1) on the peak day of the hottest heat wave in 2096–2100. (a) temperature difference between AR100 and the reference; (b) Humidity difference between AR100 and the reference. Positive means a higher temperature or humidity after mitigation actions, and negative implies a lower temperature or humidity after mitigation actions.

The above results indicate that elevating pavement albedo may not be as effective as other strategies in moderating heat waves for Washington D.C. This is because cool roofs reflect more solar radiation than reflective pavements do because of a higher albedo of cool roofs (Figure 3.8a), and green roofs enhance evaporative cooling while reflective pavements hinder it (Figure 3.8b). Moreover, Qin (2015) indicated that reflective pavements may not help reduce ambient temperature if the ratio of building height to road width, termed aspect ratio, is greater than 1.0. The reason is that reflective pavements can reflect sunlight to buildings, and tall buildings can cause multiple reflections, which results in most solar radiation absorbed by road and building surfaces. The multiple reflections cannot be simulated in the WRF model, implying that the performance of reflective pavements can be lower than the one predicted in this study. However, increasing pavement albedo has many benefits that should be considered when planning climate adaptation, such as protecting pavement surface from overheating and reducing the risk of pavement melting or breaking during extremely hot weather.

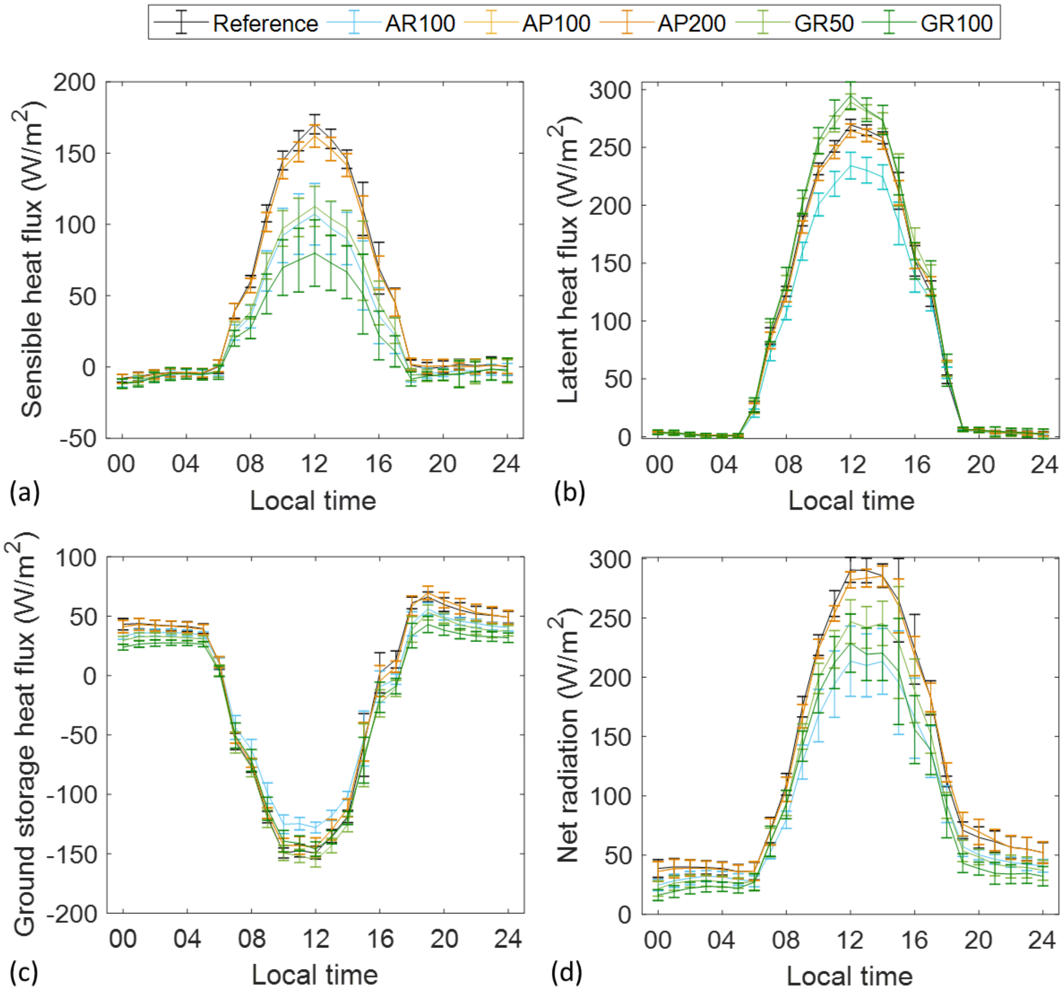

Figure 3.8 Impacts of five adaptation strategies on the surface energy balance at the peak day of the hottest heat wave in Washington D.C. for the period 2036–2040. (a) Sensible heat flux; (b) Latent heat flux; (c) Ground storage heat flux; (d) Net radiation. All results are averaged over urban grid cells in Domain 4. Error bars denote standard deviation over those grid cells. AP100 and AP200 are almost overlapped.

3.4.2. Sensitivity analysis

This study further investigates mitigation performance at different surface albedos and green roof fractions. As shown in Figure 3.9, heat wave amplitudes and warm spell duration decrease almost linearly as roof and pavement albedo and green roof increase. Li *et al*. (2014) have a similar finding that UHI intensity declines in a linear manner with green roofs increasing in a city. Heat waves amplitude and warm spell duration may decrease by 0.40–0.43°C and 2.8–5.2 days per 0.15 rise of roof albedo starting from 0.3, decline by 0.22–0.28°C and 2.3–2.9 days per 25% addition of green roof fraction starting from 0, and reduce by 0.07–0.11°C and 0.7–1.4 days per 0.15 increment of pavement albedo in the city range (Figure 3.9).

Figure 3.10 shows the mitigation effects of five strategies on fourteen less hot heat wave days in 2096–2100. The amplitude reductions of the hottest heat wave are used as references. The cool roof strategy AR100 and green roof strategy GR100 exhibit greater variabilities in temperature reduction compared to others, but their variations are less than 0.4°C as background temperature varies between 33–42°C (Figure 3.10). The average reductions over the fourteen days are overall comparable to the amplitude reductions of the hottest heat wave. Therefore, using adjusted daily maximum temperatures, which subtracts the decline in the maximum amplitude of heat wave from daily maximum temperatures, can generate reliable estimations of warm spell duration.

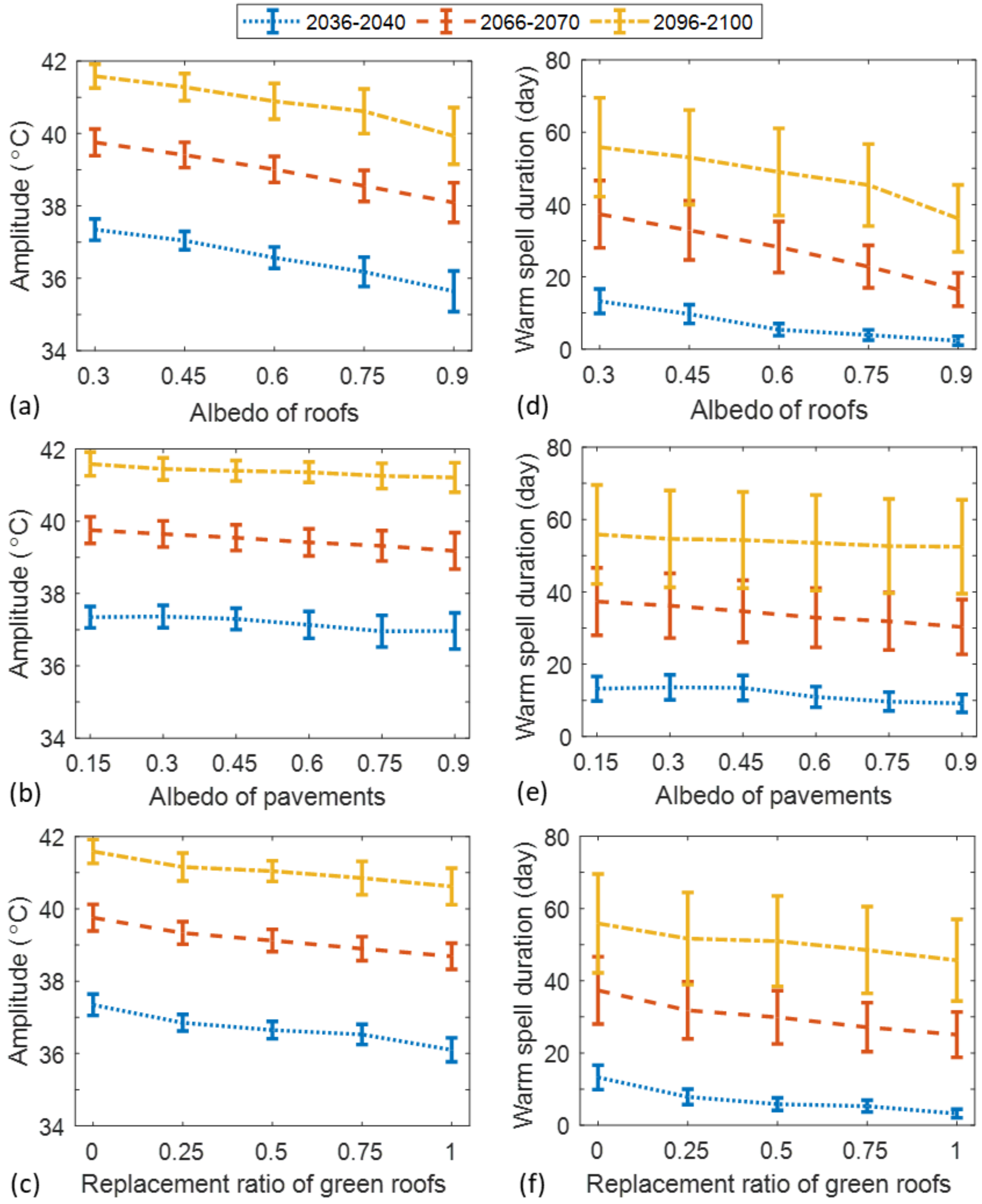

Figure 3.9 Amplitude of the hottest heat wave and warm spell duration in Washington D.C. for three time periods, 2036–2040, 2066–2070 and 2096–2100. (a)-(c) Amplitude changes as a function of roof albedo, pavement albedo, and green roof fraction. (d)-(f) Warm spell duration changes as a function of roof albedo, pavement

albedo, and green roof fraction. All results are averaged over urban grid cells in Domain 4. Error bars represent one standard deviation above and below the mean.

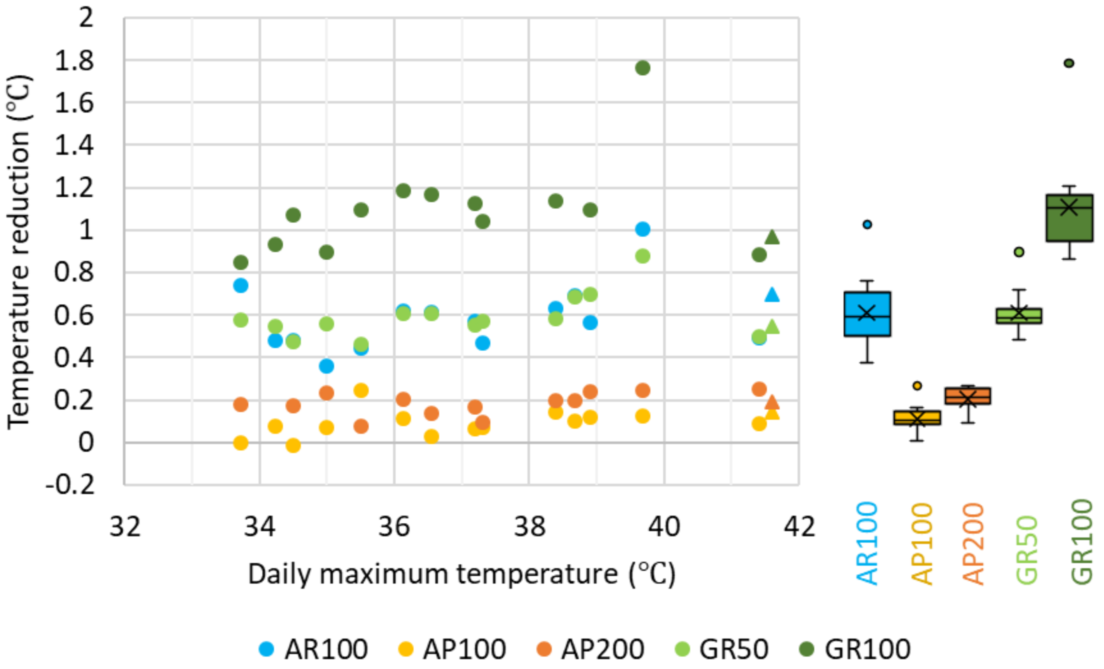

Figure 3.10 Impacts of mitigation strategies on daily maximum temperatures during heat waves in 2096–2100. The triangle makers are references. The cross “x” denotes mean; the top, middle, and bottom lines of the box represent 25th, 50th, and 75th quantiles, respectively; the top and bottom of whisker imply the minimum and maximum values, respectively; and outside dots are outliers.

There are many other factors that can affect mitigation effects. First, elevating surface albedos or increasing green roofs is more effective in reducing hot temperatures during the day compared to this night, because at night the cooling function is dominated by the reduced heat storage in the urban canopy during the day (Figure 3.8). Second, the cooling effect of green roofs can be affected by rooftop soil moisture. Li *et al*. (2014) indicated that the cooling effect of green roofs is eliminated when the soil moisture is less than 0.15 m^3/m^3. Third, the albedo of cool roofs and reflective pavements may decline due to material aging and dirt accumulation, which may degrade their performances. Fourth, when utilizing these technologies together, the benefits can be less than the sum of their parts, such as raising urban albedo and increasing green areas simultaneously (Zhou 2010; Jacobs *et al.* 2018).

3.4.3. Cost-effectiveness analysis

Kats and Glassbrook (2016) reported that in Washington D.C., cool roofs with an albedo of 0.65–0.75 may cost \$2,573/m^2 (2015 dollars) in a 40-year period. The cost of reflective pavements with an albedo of 0.3–0.45 is comparable to that of cool roofs around \$2,301/m^2. Cool roofs and reflective pavements require coating replacement after 20 years of use, which is counted in the above costs. Installing and maintaining green roofs are relatively expensive. Green roofs, with a growing media depth of 0.1 m and a leaf area index of 2, cost about \$112,633/m^2 in 40 years. Comparing the costs to the mitigation effects of the five strategies (Table 6), one can find that cool roof strategy (AR100) reduces heat wave amplitude and duration two or three times greater than reflective pavement strategies (AP100 and AP200) do for the same price. In addition, green roof strategies (GR50 and GR100) costs ten times more compared to reflective pavements in reducing the same amount of heat wave amplitude and duration.

Then a comprehensive assessment is conducted to quantify the cost-effectiveness of the five mitigation strategies. The benefits include energy conservation, stormwater reduction, human health improvement, climate change mitigation, and job creation. Energy conservation involves decreasing the cooling and heating energy consumption of buildings. The benefits on human health include reducing heat-related mortality risks and lessening ozone and fine particle (PM2.5) contents. Climate change mitigation involves reducing greenhouse gas emissions through energy savings and reducing solar radiation via albedo modification. To enable a comparison between those strategies, the benefit and cost values are normalized to unit prices ($\$/m^2$), as shown in Table 3.7. The detailed calculation is presented in the Appendix D.

Table 3.7 indicates that green roof strategies (GR50 and GR100) can generate greater net benefits compared to cool roof (AR100) and reflective pavement strategies (AP100 and AP200). The advantage of reducing stormwater makes green roofs to be a superior choice for temperate regions. Green roofs also exhibit better performance in saving energy and improving human health. However, high installation and maintenance cost makes green roofs less cost-effective compared to cool roofs. Cool roof strategy produces the highest benefit-cost ratio among the five options because of low costs and considerable benefits. The reflective pavement strategy AP200 generates two times greater net benefits than the strategy AP100 does, implying raising the albedo of pavements can increase cost-effectiveness. This applies to cool roofs, as increased costs due to albedo improvement are much lower than consequent benefits generated.

Table 3.7 Cost-benefit analysis on five mitigation strategies in a 40-year period (2017–2056), 2015 dollars, 3% annual discount rate.

Items	Strategies ($\$/m^2$)				
	AR100	AP100	AP200	GR50	GR100
Total costs	2.6	2.3	2.3	112.6	112.6
Total benefits	16.6	4.7	9.4	215.5	222.5
Energy savings	1.6	0.03	0.1	8.2	8.5
Stormwater reduction	0	0	0	190.6	190.6
Health benefits	9.5	0.7	1.3	10.0	16.6
Climate change mitigation	5.4	2.5	4.9	1.7	1.8
Job creation	0	0	0	5.0	5.0
Net benefits	14.0	0.8	4.0	102.8	109.8
Benefit-cost ratio	6.4	1.4	2.7	1.9	2.0

3.5. Conclusions

Adapting cities to increased heat waves is important and urgent. This study projects the variation of heat waves in the Washington DC metro area under the high concentration scenario RCP 8.5, representing the most severe emission and warming trajectory. The high-resolution projections can help governments and stakeholders foresee potential heat-related risks and plan appropriate adaptations for local communities. The UHI effect plays an important role in heat wave growth even though global climate change dominates the change. Implementing cool roofs and green roofs in the city range can effectively moderate heat waves, whereas reflective pavements have little impact. However, the high installation and maintenance cost may make green roofs less cost-efficient compared to reflective pavements. Cool roofs and green roofs may be slightly less effective in reducing heat wave amplitude in the future while the opposite trend is true for reflective pavements. In addition, the mitigation effect increases almost linearly as the albedo of roofs and pavements rises and as green roof fraction increases. Overall, the mitigation assessment based on Washington D.C. improves the understanding of utilizing these technologies in a dynamic environment and has significant implications for other metropolitan regions.

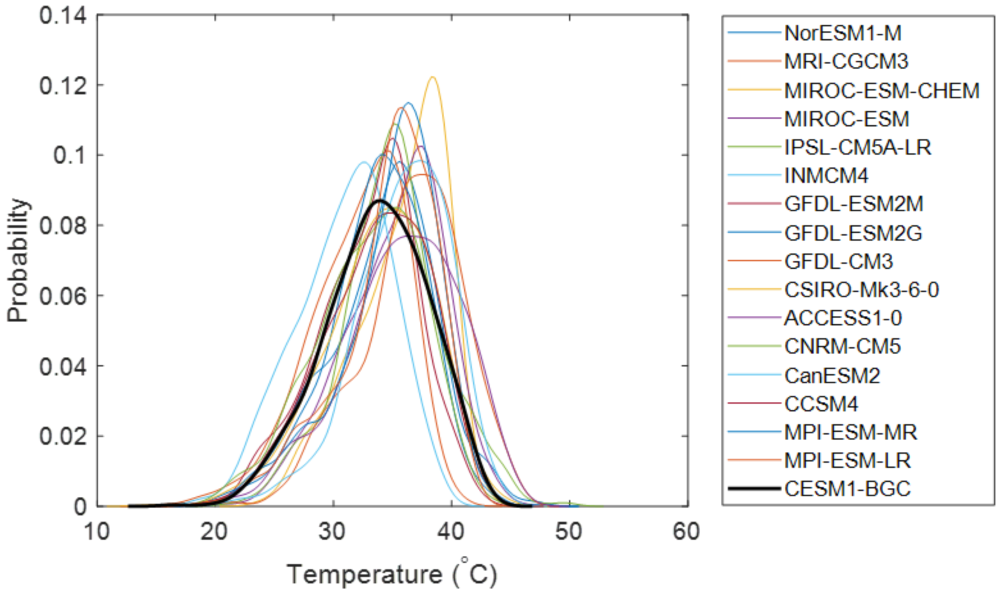

Figure 3.11 Summer (May-September) daily maximum temperature distributions for Washington D.C. in 2096–2100.

There are four major uncertainties associated with the projections in this study. First, the future emission trajectory is uncertain. This study uses the higher scenario RCP 8.5, which may lead to an overprediction or underprediction of heat wave growth if the increase in greenhouse concentration is lower or greater than the one assumed by RCP 8.5. Second, the WRF simulation is forced by one global climate model. Using the data of a different global climate model may produce different heat wave projections. Figure 3.11 presents the summer (May-September) daily maximum temperature distributions projected by global climate models archived in CMIP5 for the time period 2096–2100. The data are derived from the Lawrence Livermore National Laboratory (2019) at the same grid point that is nearest to Washington D.C. with a grid resolution of 1×1°. The figure illustrates that the shift in the mean of these distributions can be up to 7°C. However, using a different climate model may not affect mitigation strategy assessment, as mitigation effect is measured as the difference between mitigation and reference cases, which cancels the biases of heat wave projections. Third, land cover and urban morphology may change in the future. Heat waves in rural areas may increase more than this projection as a result of urbanization. The zone regulation of Washington D.C. may be adjusted to meet new requirements of development, which can affect heat wave projections and mitigation strategy assessments. Fourth, anthropogenic heat emission is uncertain, as intensified heat waves in the future may increase air conditioning use, but new technologies may improve energy efficiency and reduce waste heat. The uncertainties associated with heat emissions and new technologies can affect heat wave projections in this study.

Chapter 4: Electricity System Assessment and Adaptation to Rising Temperatures in a Changing Climate with Washington Metro Area as a Case Study

4.1 Introduction

Annual average temperatures across the contiguous United States have increased by 1°C since the beginning of the 20th century, and additional increment of 2.8–4.8°C is expected by the end of the current century (USGCRP 2018). Rising summer temperatures lead to escalated cooling demand and intensified electricity consumption (Wang and Chen 2014). Moreover, hot environment reduces the efficiency of air conditioners and increases the requirement for larger sizes of air conditioner systems, which further intensifies energy use (Santamouris et al. 2001). Santamouris et al. (2015) estimated that one degree of temperature rise that starts from 18°C can lead to 0.45–4.6% increase of peak electricity load and 0.5–8.5% growth of total electricity demand, dependent on the characteristics of building stocks, climate zones, urban morphologies, and the type of energy services (*e.g.*, cooling, lighting) provided. The electricity demand of the contiguous United States was projected to increase by 1% per year for the next 30 years, with a 0.2% deviation for lower and higher economic growth scenarios (EIA 2019a).

The increase in temperatures reduces the capacity and efficiency of power generation, transmission, and distribution, and increases the risk of power outages. The generation capacity of natural gas-fired power plants can decline by 0.7% per 1°C rise of temperature that starts from 15°C (Maulbetsch and DiFilippo 2006; Sathaye et al. 2013; Sen et al. 2018). The capacity of power lines may drop by 1.5%, and efficiency may decrease by 0.5% per 1°C rise of temperature (Burillo et al. 2016). Li et al. (2005) estimated an average loss of 0.7% in transformer capacity as the ambient temperature increases by 1°C. Sathaye et al. (2013) projected that rising temperatures in California may lead to 2–5% loss of natural gas plant capacity, 2–4% decrease of substation capacity, and 7–8% decline of transmission capacity in 2070–2099 relative to 1961–1990. Bartos et al. (2016) stated that increased summer temperatures in the United States can reduce electric transmission ampacity by 1.9–5.8% in 2040–2060 relative to 1990–2010. Larsen et al. (2018) projected that annual customer (residential, commercial and industrial customers) costs for power interruptions may reach $1.5–3.4 trillion by the middle of the 21st century and $1.9–5.6 trillion by the end of the century underlying a warming climate.

Grid construction projects require typically many years and millions of dollars to complete, and therefore improving the understanding of potential risks in the future is important to maintain reliable infrastructure systems and reduce property loss. Previous studies have assessed coarsely impacts of rising temperatures on the national power grids (*e.g.*, Bartos et al. 2016; DOE 2013), and suggested that climate impact varies regionally and depends on technology and socioeconomic conditions. However, local impact assessments are limited to the west region, such as California (Sathaye et al. 2013), Arizona (Burillo et al. 2016), and fourteen western states

(Bartos and Chester 2015), which cannot reflect the situation of other geographic regions. Washington metro area is the sixth most populous metropolitan area in the United States (Census 2019), and the vulnerability of its electrical grid to increased temperatures has not been well studied. This study fills the gap by evaluating the operation failure probability of current electrical grid when exposed to intensified hot weather in the next twenty, fifty, and eighty years for the Washington metro area. The impact of cooling demand growth and temperature rise together on the electrical grid is analyzed to provide a comprehensive view of potential susceptibilities. Such quantitative and systematical assessment would help local governments and stakeholders plan and initiate appropriate adaptations for energy infrastructure.

Rooftop photovoltaics (PV) is gaining increased attention as a clean energy technology that converts the sun’s rays into electricity directly for building use. The benefits of solar PV have been discussed extensively in the literature, including lowering energy costs, reducing greenhouse gas emissions, decreasing harmful air pollutants, improving public health, providing work opportunities, and enhancing the reliability and security of electric power systems (Tsoutsos et al. 2005; Kats and Glassbrook 2016). The government of Washington D.C. has taken action to maximize renewable energy generation especially solar energy in order to achieve the goal of carbon neutrality by 2050 (DOEE 2018). The launched Smart Roof Program and employed solar incentive measures have accelerated rooftop PV installation in the district (BLUEFIN 2013; DOEE 2016). To help make the best use of solar energy, this study investigates adoption potential of rooftop PV for the Washington metro area, and analyzes the cost-benefit of PV strategies in reducing peak cooling load on the electric grid. Such analyses would provide references for policies and actions in relation to resilience and sustainability goal.

The Intergovernmental Panel on Climate Change (IPCC) proposed a linear process for climate adaptation (Carter et al. 1994), which is considered as the mainstreaming of adaptation nowadays. The process starts with scientific analysis of climate change including variability, then measures residual or net climate impacts after autonomous adaptations, and finally determines adaptation needs. Subsequently introduced frameworks for climate adaptation accounted for policy criteria, population growth, economic development, and other non-climate factors, generating accessible and affordable options (*e.g.*, Fussel 2007; Bollinger et al. 2014; Munaretto et al. 2014). This study extends these frameworks to a generalized form by incorporating into the probabilistic risk method in order to appropriately model uncertainties and sophisticated relations. The underlying probabilistic risk method starts with climate scenarios and projections, and inputs them into impact models to generate loss estimation (Stewart and Deng 2015; Ayyub et al. 2018). A set of conditional probabilities are employed to quantify the likelihood of intensified climate stressors, climate impacts, monetized losses, and adaptation potential. The method has the following advantages compared to other hazard-based and vulnerability-based approaches reviewed by Fussel (2007). Firstly, probabilities can describe the uncertainties in outcomes that are propagated from climate projection to impact evaluation, failure assessment, and loss estimation. Secondly, multiple climate stressors, various systems and assets, and different failure and damage types can be assessed simultaneously through the linkage of conditional probabilities, providing a systematic risk profile suitable for risk management. Like the Bayesian decision network approach (Catenacci and Giupponi 2013), the probabilistic risk analysis allows combining historical data and expert judgment into planning assessment. The former focus on eliciting and combining expert opinions, while the latter emphasizes scientific analysis based on observation and model simulation.

The objectives of this study are to assess the vulnerability of the electric grid in the rest of the current century for the Washington metro area, evaluate the cost-effectiveness of using rooftop PV to enhance the resilience of the power system, and improve adaptation planning and decision making with quantitative probabilistic risk analysis. The next section of this chapter introduces the framework of adaptation planning incorporating in the probabilistic risk method, and the model for failure analysis of the electricity system. The section that follows provides projection results of summer temperatures and peak electricity demands. Then future vulnerability of the electrical grid in the Washington metro area is quantified using failure probabilities as indicators. Three adaptation strategies based on rooftop PV technology are evaluated and compared through the life-cycle benefit-cost analysis. The last section concludes and discusses the implications of this study.

4.2 Methodology

4.2.1 Probabilistic risk method

Risks incurred by climate change is defined as a summation of possible losses due to different climate scenarios, climate stressors, and system failures (Stewart and Deng 2015; Ayyub et al. 2018). The following equation calculates the net present value of climate risks as a loss (L):

$$L = \sum_{t=t_0}^{n} [\sum_{C_C} \sum_{C_S} \sum_{F} \sum_{L} P(C_C)P(C_S|C_C)P(F|C_S)P(L|F)L](1 + r)^{-(t-t_0)} \tag{4.1}$$

where $P(C_C)$ is the probability that a climate-change scenario occurs. $P(C_S|C_C)$ is the probability that a stressor intensifies when climate changes. $P(F|C_S)$ is the probability of system failure when the stressor intensifies. $P(L|F)$ is the probability of a loss when the system fails. r is the annual discount rate. t is the time in years starting from the year t_0. n is the number of years accounted for risk estimation.

If only one climate scenario and climate stressor are considered, and one type of failure and loss is analyzed, Equation 4.1 can be rewritten as follows.

$$L = P(C_S|C_C) \sum_{t=t_0}^{n} [P(F|C_S)P(L|F)L]\,(1 + r)^{-(t-t_0)} \tag{4.2}$$

After taking adaption actions, the risk is reduced as follows.

$$L_{adapt} = P(C_S|C_C)\sum_{t=t_0}^{n}[(1-\Delta R)P(F|C_S)P(L|F)L](1+r)^{-(t-t_0)} \tag{4.3}$$

where ΔR is the coefficient of risk reduction due to climate adaptation, ranging between 0 and 1.

4.2.2 Framework for adaptation planning

Figure 4.1 shows the four steps of adaptation planning that define the framework that incorporates the probabilistic risk method. The first step selects climate stressors and projects future exposures. A climate stressor can be a temperature shift, precipitation change, or sea level rise, *etc*. The probability that the stressor intensifies, $P(C_S|C_C)$, can be estimated based on projection results of climate models supplemented with professional judgment in some cases. The second step identifies vulnerable systems and assets and measures the sensitivity of each system to the stressor. This is the most important part of planning, which determines the targets and goals of adaptation activities. The failure probability of a system when exposed to the climate stressor, $P(F|C_S)$, can be estimated using historical data, model simulation results, or expert opinion elicitation (Ayyub 2001). The third step selects adaptation schemes and assesses risk reductions associated with the respective implementation of the schemes. Adaptation options may include new techniques and equipment, new regulations on some industry sectors, and incentive programs for some practices.

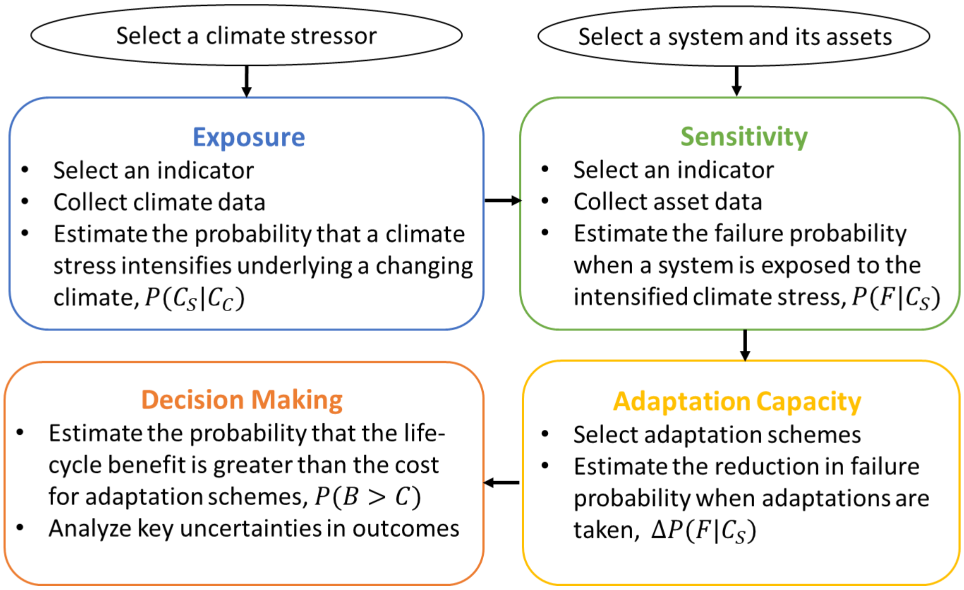

Figure 4.1 The framework for climate adaptation planning incorporated in the probabilistic risk method.

The adaptation capacity, $\Delta P(F|C_S)$, is measured as the reduction in failure probability of a system when adaptation actions are taken. The capacity may vary with different geographic regions and system characteristics. The last step conducts a life-cycle benefit-cost analysis to compare and optimize adaptation schemes. Benefit-cost analysis is widely used in the engineering decision-making process (Ayyub 2014). The benefit (B) means potential reductions in climate event losses, and cost (C) implies investments for mitigating climate events, improving system resilience, or both. Comparisons aim to find the option that reduces the risk in cost-effective terms within any budgetary or regulatory constraints. Optimization intends to seek the appropriate timing for the adaptation to enable the investment to be most cost-effective.

4.2.3 Failure model for electricity systems

Natural gas is the largest source for electricity generation in the mid-Atlantic region and contributed to 39% of generation in 2018, while coal, nuclear, petroleum and renewable energy sources produced 31%, 18%, 7% and 5% electricity, respectively (NERC 2018). Natural gas-fired power plants suffer greatly from temperature rise, because power produced by turbines is dependent on air mass flow rate, and air mass flow that enters the gas turbine compressor decreases as ambient temperature increases (Kehlhofer et al. 2009; González-Díaz 2017). The decreased air mass flow rate also reduces turbine pressure ratio, and thereby lowers temperature difference between inlet and outlet airflow, resulting in an efficiency loss of gas turbines (Kehlhofer et al. 2009; González-Díaz 2017). Coal-fired and nuclear power plants are affected by temperature rise, as the hot environment reduces the cooling efficiency of air-cooled condensers and water-cooling towers by elevating air and water temperatures (González-Díaz 2017).

The increase of temperature lowers performance of power grids, because the capacity of transmission lines is restricted by the operating temperature that is typically 100°C, and hot environment hinders the natural cooling process of electrical lines (Sathaye et al. 2013). Similarly, the capacity of substations is constrained by the operating temperature of transformers. The loss of substation capacity occurs when the ambient temperature exceeds 30 °C, approximately to a 120°C hot spot temperature for a typical transformer (Li et al. 2005). The hot spot temperature measures the temperature of the hottest section of a transformer.

Service interruption occurs when the total power generation cannot meet the total demand, or when the capacity of the pathway (transmission lines and substations) is insufficient to deliver the power to the load (Burillo et al. 2016). Figure 4.2 presents the fault tree analysis of service interruption in the power system. Three major components in the system are generation, transmission, and substation that delivers electricity to customers. Figure 4.3 illustrates the procedure in analyzing the failure probability of the power system as temperature changes. Literature indicated that the generation capacity (β_{GC}) of power plants, the transmission capacity (β_{TC}) and efficiency (β_{TDE}) of power lines, and the capacity (β_{SC}) of substation decline by 0.7%, 1.5% and 0.5%, and 0.7% respectively per 1°C temperature rise (Li et al. 2005; Maulbetsch and DiFilippo 2006; Sathaye et al. 2013; Burillo et al. 2016; Sen et al. 2018). The peak load (β_{PKload}) increases by 7.5% per 1°C temperature increase, with details provided in a later section. The increase in peak load is treated as capacity loss in generation, transmission, and substation sectors in order to simplify the calculation. Therefore, the equivalent generation capacity (β_{G}), transmission capacity (β_{T}) and substation capacity (β_{S}), which add up capacity loss, effeciciy decline, and peak load shift, drop by 8.7%, 9%, and 8.2% respectively per 1°C temperature increase (Figure 4.3).

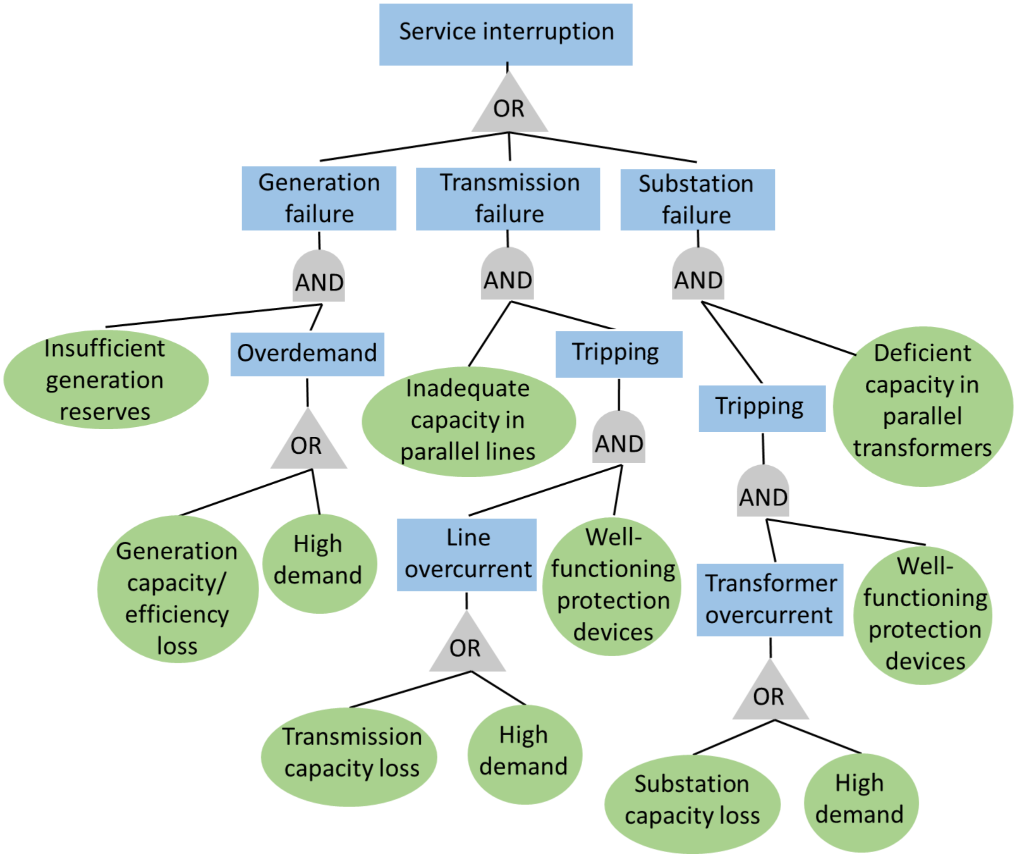

Figure 4.2 Fault tree analysis for service failures in the electricity system.

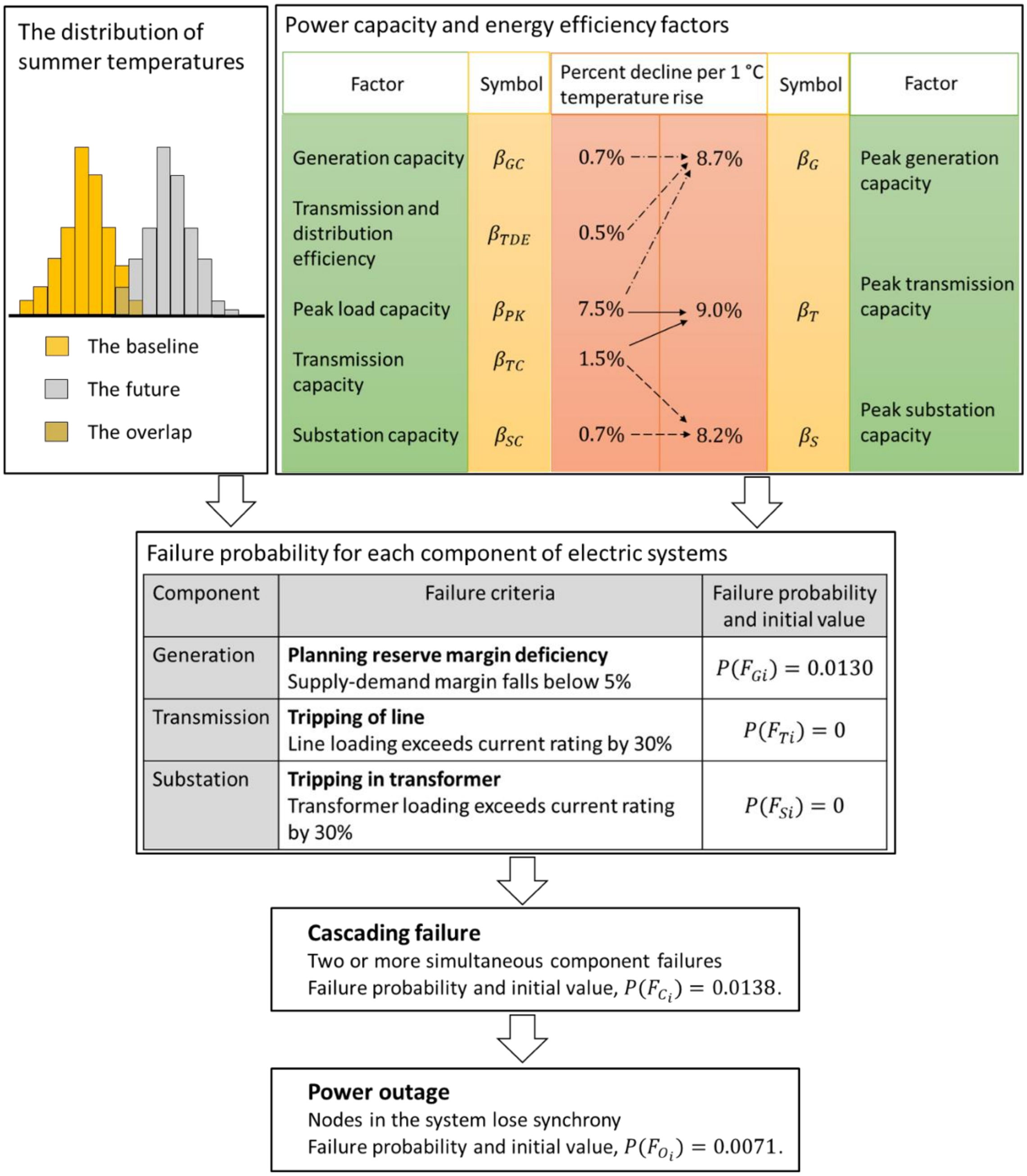

Factor	Symbol	Percent decline per 1 °C temperature rise		Symbol	Factor
Generation capacity	β_{GC}	0.7%	8.7%	β_G	Peak generation capacity
Transmission and distribution efficiency	β_{TDE}	0.5%			
Peak load capacity	β_{PK}	7.5%	9.0%	β_T	Peak transmission capacity
Transmission capacity	β_{TC}	1.5%			
Substation capacity	β_{SC}	0.7%	8.2%	β_S	Peak substation capacity

Component	Failure criteria	Failure probability and initial value
Generation	**Planning reserve margin deficiency** Supply-demand margin falls below 5%	$P(F_{Gi}) = 0.0130$
Transmission	**Tripping of line** Line loading exceeds current rating by 30%	$P(F_{Ti}) = 0$
Substation	**Tripping in transformer** Transformer loading exceeds current rating by 30%	$P(F_{Si}) = 0$

Figure 4.3 Failure analysis procedure for the electricity system. Failure probability is calculated in summers (June–August). Initial value refers to the one in the baseline period, 2011–2015.

The change ratio of failure probability for each component in the power system, $\Delta p(F)$, is calculated as the difference between failure probability in the future $P(F_f)$, and in the baseline period $P(F_i)$, divided by the failure probability in the baseline period as follows:

$$\Delta p(F_a) = \frac{P(F_{af}) - P(F_{ai})}{P(F_{ai})} \tag{4.4}$$

where the subscript *a* is generation (*G*), transmission (*T*), or substation (*S*). The *f* denotes the future, and *i* means the baseline or initial period.

A cascading failure is a process in a system of interconnected parts in which the failure of one or few parts can trigger the failure of other parts and so on. In electrical grids, one or several elements disrupted by a shock will shift their loads to nearby elements, and nearby elements that fail to bear the superimposed load will shift the load to others. The *N*-1 criterion, typically used to design high-voltage transmission systems, requires that the failure of any single component (*e.g.*, generator, transmission line branch, substation) at any time cannot disturb the service. In other words, more than one major component fails at the same time may cause service interruption. Therefore, the probability of cascading failure, $P(F_C)$, is calculated as one minus the probability that no element failure, minus the probability that one element failure as follows:

$$P(F_C) = 1 - \prod_{a}^{m}(1 - P(F_a)) - \sum_{a}^{m}[P(F_a) \cdot \prod_{a}^{m-1}(1 - P(F_a))] \qquad (4.5)$$

where a values are for the products and summation cover all the generators (G's), transmission lines (T's), and substations (S's) in the electric network; and m is a sum of the number of generators, transmission lines, and substations in the electrical grid.

The probability of power outage, $P(F_O)$, is calculated as the probability of cascading failure times a cascade trigger coefficient (α) as follows:

$$P(F_O) = P(F_O|F_C) \cdot P(F_C) = \alpha \cdot P(F_C) \qquad (4.6)$$

The cascade trigger coefficient quantifies the probability of power outage when the system is exposed to a shock. The coefficient is measured as the percent of node failures in a system and determined in a later section. In most cases, a shock affects only part of the electrical network because of system redundancy. Literature indicated that cascading process is dependent on the initially damaged lines and the scale or topology of the system (Song et al. 2016; Schafer et al. 2018).

4.3 Vulnerability assessment

4.3.1 Temperature projection

Temperature projection is the first step of failure analysis. The layout of the electrical grid in the Washington metro area is shown in Figure 4.4a (EIA 2019b), and the network model with 109 nodes and 131 branches is displayed in Figure 4.4b. Summer (June–August) daily maximum temperatures are projected using the Weather Research and Forecasting (WRF) model (Skamarock et al. 2008) that downscales Community Earth System Model (CESM) version 1.0 data (Monaghan et al. 2014). Projections are forced by the highest Representative Concentration Pathway (RCP) 8.5 (IPCC 2013), which is recognized as the business-as-usual scenario. Four time periods 2011–2015, 2036–2040, 2066–2070 and 2096–2100 are analyzed, representing the present and the next twenty, fifty and eighty years, respectively.

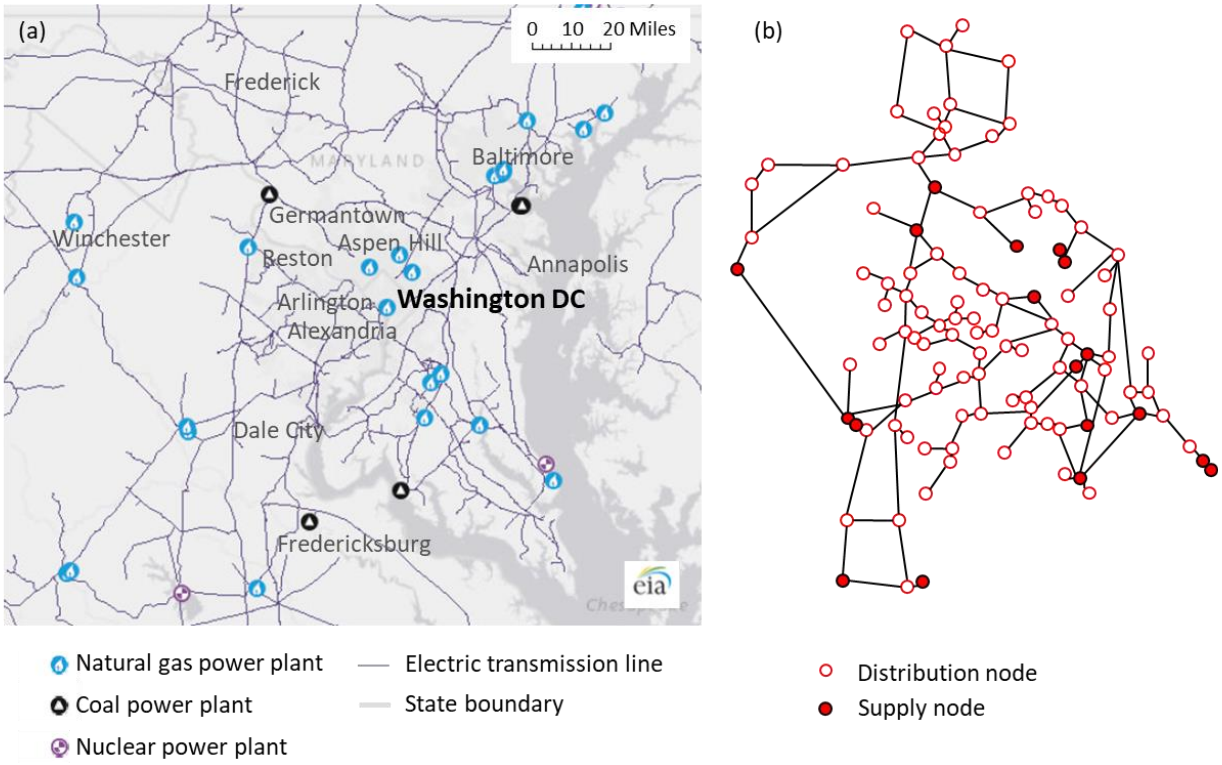

Figure 4.4 Spatial distribution of electric transmission lines and power plants in the Washington metro area. (a) The map for the electric network (EIA 2019b); (b) Electric network model with 109 nodes and 131 branches.

Projection results for summer daily maximum temperatures are presented in Figure 4.5 and Figure 4.6. Figure 4.5 shows a growing trend of temperature in the Washington metro area, indicating the increased vulnerability of electrical grids in the future. Figure 4.6 illustrates a shift of temperature distribution towards a warmer climate at Washington D.C. The localized temperature of Washington D.C. is used in the failure analysis because the urban temperature is typically warmer than that of rural areas and can lead to a higher susceptibility.

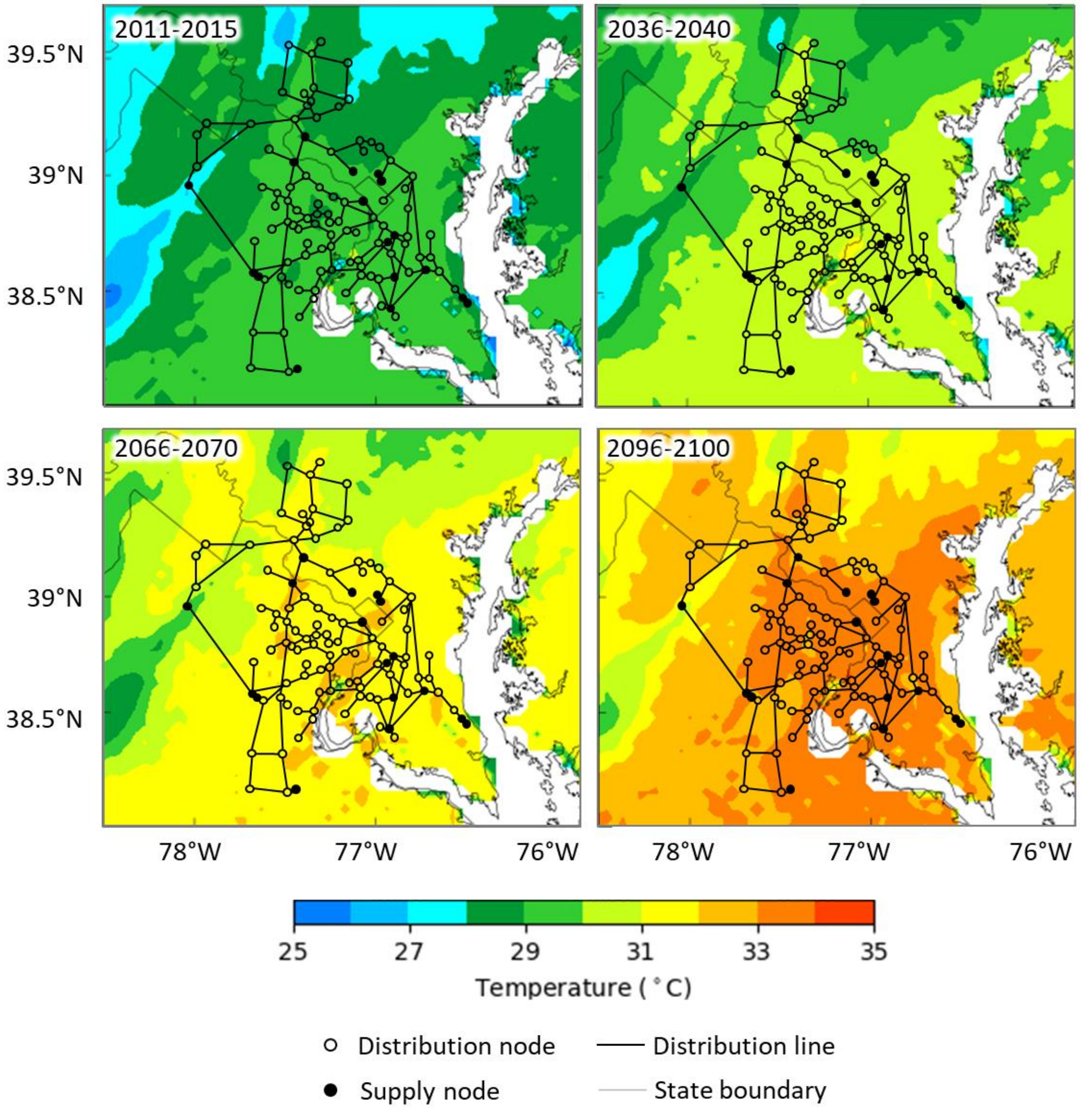

Figure 4.5 Averaged summer (June–August) daily maximum temperatures of Washington metro area in three future periods, 2036–2040, 2066–2070 and 2096–2100, and the baseline period 2011–2015, with a grid resolution of 4×4 km. The white areas are waters.

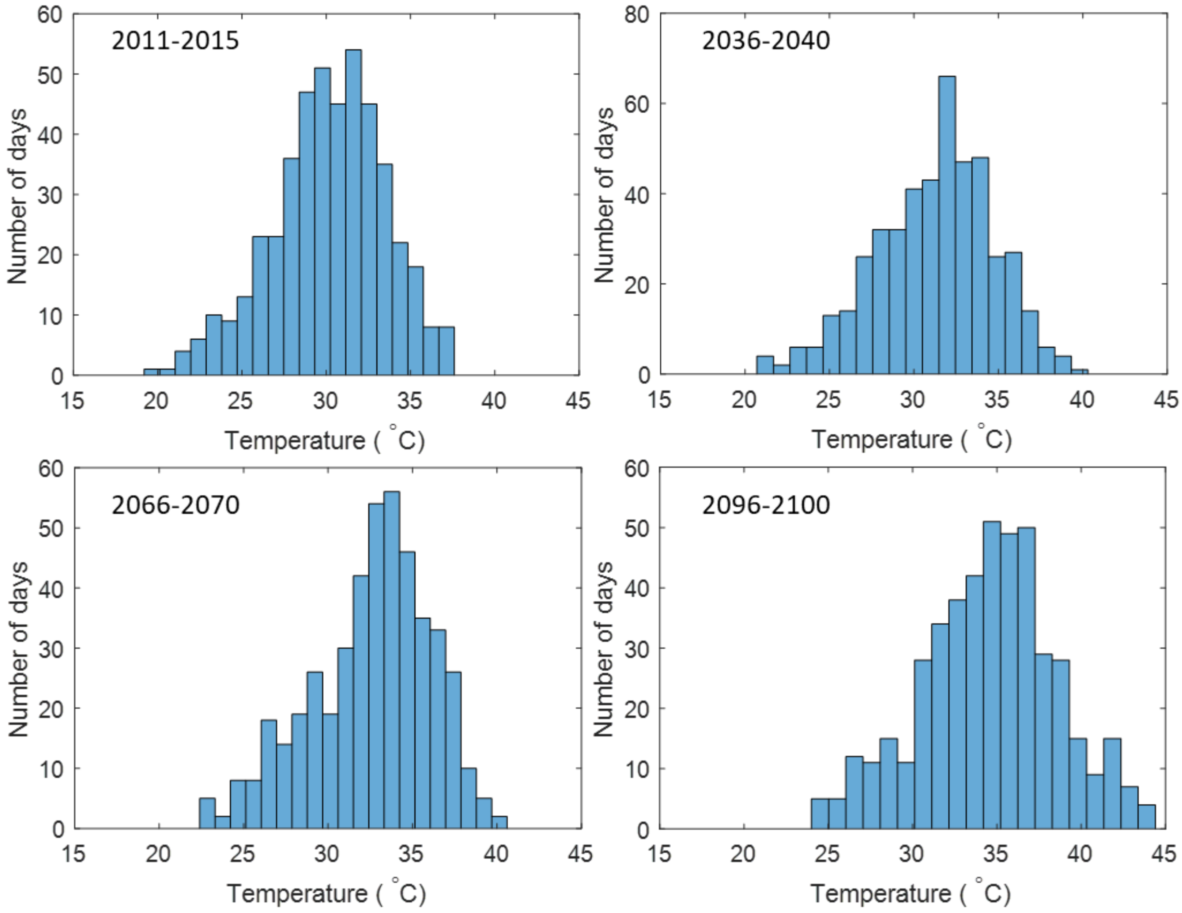

Figure 4.6 Summer (June–August) daily maximum temperature distributions for Washington D.C. in three future periods, 2036–2040, 2066–2070 and 2096–2100, and the baseline period 2011–2015.

4.3.2 Electricity demand projection

This study conducts a range of statistical tests to determine which mathematical function (linear, polynomial and exponential) best describe the relationships between the peak electricity demand and temperature (daily maximum, mean and minimum temperatures). The results suggest that peak electricity demand is most correlated to daily maximum temperatures, and second-order polynomial function can characterize the relationship well, as shown in Figure 4.7a. The daily mean temperature of 18°C is regarded as the threshold for building cooling needs (NOAA 2019). Considering that summer daily temperatures vary around 10°C, the daily maximum temperature of 23°C is used as the threshold for cooling energy needs. Since peak load at 23°C is 92 GW for the mid-Atlantic region in recent years (Figure 4.7a), peak load above 92 GW is attributable to building cooling. Figure 4.7b shows the change of peak cooling load as temperature increases starting from 23°C. Average summer daily maximum temperature is projected to grow from 34–38°C in the baseline period to 40–46°C by the end of the century. In the temperature range of 35–45°C, peak cooling demand shows a growing trend of 7.5% per 1°C temperature rise on average, and therefore 7.5% is used in this analysis as the coefficient of peak generation capacity (β_{PK}). By the end of the century, the average peak cooling load may rise by 40% relative to the baseline (Figure 4.7b), and equal to peak load excluding cooling portion.

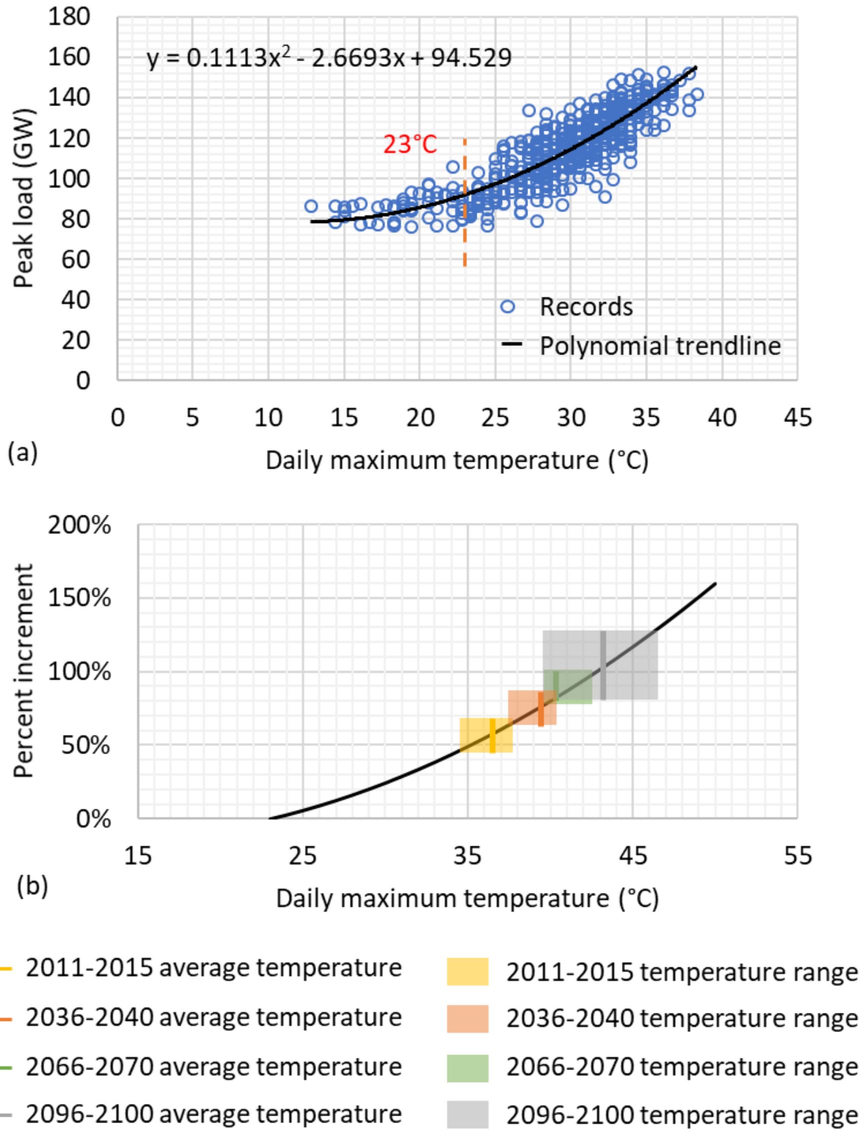

Figure 4.7 Peak load in mid-Atlantic region as a function of temperature at Washington D.C. (a) The second-order polynomial relationship between peak load and temperature based on records from May–September 2015–2018; (b) Percent increment in peak cooling load in the baseline period 2011–2015, and three future periods 2036–2040, 2066–2070 and 2096–2100.

4.3.3 Failure probability of major elements

Planning reserve margin deficiency

The planning reserve margin is the amount of generation capacity available to meet expected demand, and is measured as the difference in prospective resources and internal demands divided by internal demands. System operators typically issue alerts when the reserve margin falls below 5%. The 5% is therefore used as the critical value (PRM_{crit}) in this dissertation to indicate the failure of power plants in meeting electricity demands. The planning reserve margin of the 2018/2019 delivery year is 16.1% (PRM_i) in the mid-Atlantic region (PJM 2017). The 95th percentile of daily maximum temperature distribution is 35°C (T_{PRM}) in 2018 summer, based on the observed data at Ronald Reagan Washington National Airport (NOAA 2019). The temperature when planning reserve margin ($T_{PRMcrit}$) reaches 5% is estimated using the following equation (Burillo et al. 2016).

$$T_{PRMcrit} = T_{PRM} + \frac{PRM_i - PRM_{crit}}{\beta_G} \tag{4.7}$$

where β_G is the coefficient of peak generation capacity, as described in Figure 4.3. The failure probability due to insufficient planning reserve margin, $P(F_G)$, is estimated as the area under the temperature distribution and above $T_{PRMcrit}$.

Line overcurrent

Overcurrent is the state that power flow exceeds the rated ampacity of transmission lines. Excess load in summer due to the use of air conditioners can cause line overcurrent and serious equipment damage. If protection devices function correctly, overcurrent lines will trip and shift their loads to nearby lines. Service interruption may occur if the capacity of parallel branches is insufficient to carry power to the load, causing cascading line tripping. This study assumes that the mean summer current corresponds to mean summer daily maximum temperature and equals to 60% of line conductors' ampacity. This assumption is also used by Burillo et al. (2016) to investigate line tripping likelihood. The failure probability of transmission lines due to overcurrent is estimated as the area under the summer daily maximum temperature distribution and above the temperature that causes the conductor to exceed its rated ampacity by 30%. Overload protection devices cut the power based on the percent exceedance of ampacity, and the higher the current exceeding conductor's ampacity, the shorter the tripping time. The breaking time for 30% of ampacity exceedance is pretty short, which is suitable for cascading simulation in this study. The daily maximum temperature that causes conductor failure, T_T, is therefore estimated as follows:

$$T_T = T_{mean} + \frac{130\% - 60\%}{\beta_T} \tag{4.8}$$

where T_{mean} is the average summer daily maximum temperature.

Transformer overcurrent

Similarly, overcurrent is the state that power flow exceeds the safe operating capacity of transformers, which leads to the tripping of transformers, and perhaps cascading tripping and service interruption. The mean current flow is assumed to correspond to the mean of summer daily maximum temperature, and to be 60% of the transformer ampacity. The failure probability of transformers due to overcurrent, $P(F_S)$, is estimated as the area under the temperature distribution and above the temperature that causes the transformer to exceed its rated ampacity by 30%. The daily maximum temperature that causes transformer failure, T_S, is therefore estimated as follows:

$$T_S = T_{mean} + \frac{130\% - 60\%}{\beta_S} \tag{4.9}$$

4.3.4 Failure probability of the electricity system

Swing equations

To determine the cascade trigger coefficient (α), dynamic swing equations (Schafer et al. 2018) are employed to simulate the cascading process of the electric power system after disruption in the Washington metro area. The swing equations are given as follows:

$$\frac{d}{dt}\theta_i = \omega_i \tag{4.10}$$

$$\frac{d}{dt}\omega_i = P_i - \gamma\omega_i + \sum_{j=1}^{N} K_{ij}\sin\left(\theta_j(t) - \theta_i(t)\right) \tag{4.11}$$

where ω_i is the angular velocity at node i. θ_i and θ_j are voltage phase angles at nodes i and j. P_i is the power generated or consumed at the node i. P_i is positive when the node feeds power into the network and negative when the node absorbs power. ρ is a damping constant and assumed to be 0 for all nodes in this study. K_{ij} is the coupling strength of two connected nodes i and j.

To solve Equations 4.9 and 4.10, stable-state operation requirements are used as initial conditions. At the stable state, the voltage phase angles of all nodes are synchronous, and the differences between phase angles do not change over time. In other words, ω_i, θ_i and θ_j do not change over time and are termed fixed-point angular velocity (ω_i^*) and fixed-point angles (θ_i^* and θ_j^*). The initial conditions are given as follows:

$$\omega_i^* = 0 \tag{4.12}$$

$$P_i + \sum_{j=1}^{N} K_{ij}\sin\left(\theta_j^* - \theta_i^*\right) = 0 \tag{4.13}$$

A line is overloaded when the power flow ($F_{ij}(t)$) exceeds its capacity. The capacity of a line, C_{ij}, is defined as K_{ij} multiplying a tolerance parameter, β. The K_{ij} and β are constants and predefined. The capacity of lines is therefore constant and dependent on the physical properties instead of the initial state of a system. The overloaded line *i-j* can be expressed as follows:

$$F_{ij}(t) = K_{ij}\sin\left(\theta_j(t) - \theta_i(t)\right) \tag{4.14}$$

$$F_{ij}^{*} = K_{ij} sin\left(\theta_j^{*} - \theta_i^{*}\right) \tag{4.15}$$

$$\left|F_{ij}\right| > C_{ij} = \beta \cdot K_{ij}, \qquad \beta \in [0, 1] \tag{4.16}$$

Equation 4.13 calculates dynamic power flow, while Equation 4.14 computes power flow at the stable state.

It worths noting that branch failure may not cause a power outage, but node failure can lead to blackout in the served area. A node is failed when the angular velocity at the end of the simulation (t_{max}) surpasses the stable operation boundary as follows (Schafer et al. 2018):

$$|\omega_i(t_{max})| > 2\pi \cdot \Delta f \tag{4.17}$$

where Δf is the frequency deviation, and 20 mHz is used in this study to ensure that the system can operate at a stable state. The duration of the simulation t_{max} is 50 s to ensure that the failure process is completed by the end of the simulation.

Failure model

As shown in Figure 4.4a, eighteen power plants are located in the Washington metro area, including fourteen natural gas plants, two coal plants, and two nuclear plants. The three plant types are characterized by a positive power P^+ of 4.75/s^2, 4.25/s^2 and 8/s^2 respectively, based on their average generation capacities (EIA 2019b). Ninety-one consumers are characterized by a negative power P^- of -1/s^2. The power values used above are per-unit quantities in order to simplify power system calculation. The electric network is assumed to be isolated, and therefore no external power feeds in or internal power flows out of the system (Figure 4.4b). The total positive power equals to the total negative power.

The capacity of each line is supposed to be proportional to the power flow at the stable state, in order to maximize the efficiency of line elements and minimize the cost of grid construction projects (Schafer et al. 2018). Specifically, the maximum capacity of transmission lines is designed to be twice of carried power flow at the stable state; that is, $F_{ij} \approx 0.5K_{ij}$ and $\beta \approx 0.5$. In the real world, the dimension of transmission lines is fixed, and designers choose the appropriate one from the manual to meat capacity requirement. This study initiates K_{ij} with 5/s^2, and updates K_{ij} iteratively using the equation below. The old values of K_{ij}^{old} and F_{ij}^{old} are calculated using Equations 4.13 and 4.15.

$$K_{ij}^{new} = 0.99K_{ij}^{old} + 0.01 \times (2F_{ij}^{old}) \tag{4.18}$$

Iterating 150 times produces the most robust network in this analysis, whereas raising or reducing loop numbers causes increased line failures for a given tolerance. To ensure that the network meets the N-1 criterion, the K_{ij} values are elevated for several vulnerable branches so that any branch failed cannot trigger other failures. The results of K_{ij} are presented in Table C1. When the tolerance (β) is set to 1, the 131 different N-1 grids and 8,515 different N-2 grids pass the failure tests at the stable state using Equation 4.16. This means that the system can reach a new steady state after randomly removing one or two branches.

Then dynamic testing is conducted to capture transient voltage violation, which has a very small chance in causing cascading failure unless the numbers are big enough. The results of the static test above are used as initial conditions. The dynamic testing based on Equations 4.10, 4.11 and 4.17 shows that 8,515 different N-2 grids generate an average failure of about 56 nodes. Therefore, the cascade trigger coefficient (α) is determined to be 0.514 (56/109). Using the value of 0.514 may underestimate failure probability of the network, because N-3 grids, N-4 grids, and so on can generate a greater number of node failures, and the whole system may fail when the initial failure number is large enough. However, the small probability that many components fail simultaneously at the beginning offsets the high probability of secondary (cascading) failure. Moreover, the electricity system simulated in this study is a small portion of the national electrical network, making it more sensitive to a shock compared to the regional or national one because of less system redundancy. This can lead to somewhat overestimation of the cascade trigger coefficient.

The probability of power outage is calculated using Equation 4.7. The results are presented in Figure 4.8 and more detailly in Tables C2–C5. Four scenarios are considered, where the business-as-usual scenario assumes that summer peak cooling load will increase by 7.5% per 1^{o}C rise of temperature in the future. Another three scenarios describe the situation that peak load will rise by 5.625%, 3.75%, and 1.875% per 1^{o}C temperature rise because new technologies are deployed to reduce loads on power grids. The assumed increase rates are three quarters, a half, and one quarter of the business-as-usual scenario.

Figure 4.8 illustrates that failure probability may grow expeditiously in the rest of the century because of a warming climate. The cascading failure probability reaches one in summers of 2066–2070 and 2096–2100 under the 7.5% scenario, and in summers of 2096–2100 under the 5.625% scenario, and hence the power outage probability of the three cases equal to the maximum likelihood of 0.514 (Figure 4.8d). Reducing the peak electricity load on power grids can significantly lower the failure probability of each component and the entire system (Figure 4.8). This is because the system encompasses a large number of elements, a small increment or reduction in the failure probability of elements can greatly elevate or decrease the chance of service interruption. Transmission lines and transformers are more sensitive to the peak load compared to power generation sectors (Figures 4.8a-c), because the failure of power plants is dominant by the loss of generation capacity and efficiency. Therefore, additional adaptation actions are necessary for generation sectors, such as increasing power plant capacities and deploying advanced cooling technologies.

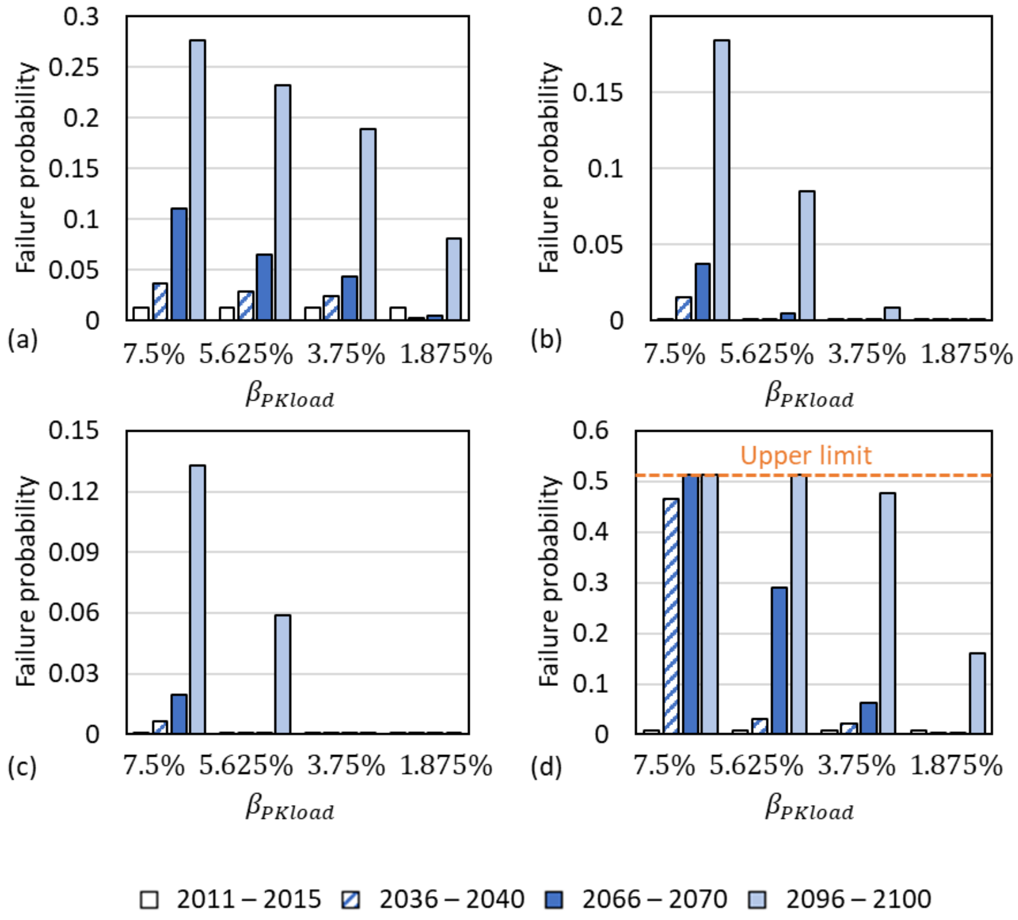

Figure 4.8 Failure probabilities of the electricity system during summer in three future periods, 2036–2040, 2066–2070, 2096–2100, and the baseline period 2011–2015: (a) Generation failure; (b) Transmission failure; (c) Substation failure; (d) Power outage. The upper limit indicates a cascading failure probability of one. Four scenarios assume that peak load (β_{PKload}) increases by 7.5%, 5.625%, 3.75% and 1.875% respectively per 1°C temperature rise.

Figure 4.9 presents the change ratio of power outage probability (see Equation 4.4 for calculation) in three future periods relative to the baseline case. Without any adaptations, the likelihood of service interruption may increase more than seventyfold by the end of the century, meaning the event of two or more simultaneous element failures in the power grids is 70 times more likely to cause power outage in the Washington metro area during summers. Surprisingly, the 1.875% scenario results in lower service interruption chance in the summers of 2036–2040 and 2066–2070 compared to the baseline period 2011–2015, because the reduced failure probability of each element exceeds the increment caused by temperature rise.

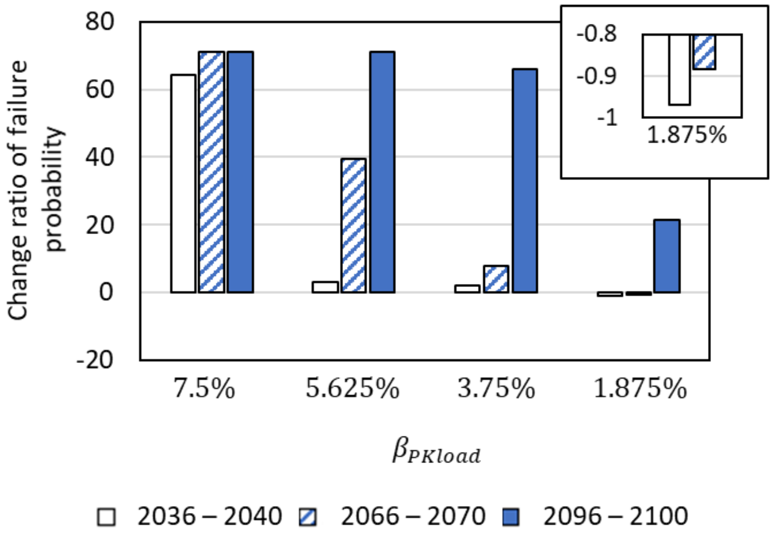

Figure 4.9 Change ratios for the probability of power outage in three future periods, 2036–2040, 2066–2070, 2096–2100, relative to the baseline period 2011–2015. Four scenarios assume that peak load (β_{PKload}) increases by 7.5%, 5.625%, 3.75% and 1.875% respectively per 1°C temperature rise.

4.4 Adaptation assessment

4.4.1 Rooftop photovoltaics

Solar photovoltaic (PV) panels installed on roofs can provide on-site electricity generation. The performance of PV panels is affected by sun intensity, cloud cover, relative humidity, and ambient temperature. Sun intensity dominants the power production of PV panels. Electricity production grows as solar radiation increases. Clouds can reduce sun intensity and adversely affect the productivity of PV panels. Humidity can penetrate solar panel frames, lower power generation efficiency, and deteriorate PV modules. Hot temperatures increase the conductivity of semiconductor, lower the magnitude of the electrical field, and thereby reduce power generation of PV panels.

4.4.2 Potential for adaptation

Roofs facing southwest to southeast with tilt value less than 60 degrees and projected horizontal footprint greater than 10 m^2 are suitable for PV panels (Gagnon et al. 2016). The suitable roof areas estimated by Phillips and Melius (2016) using lidar technology and model simulation are employed in this study. Data at the state level are adjusted to the county level based on population weight in 2010 (Census 2010). This adjustment may lead to underestimated roof areas if buildings in the area are above-average building counts per capita, and overestimation if buildings in the area are below-average building counts per capita. The following assumptions made by Gagnon et al. (2016) regarding the productivity of PV modules are employed in this study: (1) The power density value of PV systems is 160 w/m^2, corresponding to a module efficiency of 16%; (2) Energy loss due to the system itself is 14.08%, and the efficiency in inverting direct current to alternating current is 96%; (3) Every 1.2 kW direct current can be converted to 1 kW alternating current. The mean power generation capacity of rooftop PV in the Washington metropolitan is calculated to be 8.44 GW, 1.61 GW and 2.97 GW for small, medium and large buildings, respectively. The mean total generation capacity is 13.02 GW. The detailed calculation is presented in Table 4.1.

4.4.3 Cost-benefit analysis

The peak electricity load of the mid-Atlantic region is 152.89 GW during May–September 2015–2018 (EIA 2019c), and hence the peak load of Washington metro area is estimated to be 14.42 GW based on population weight in 2016. Considering that the total generation capacity of rooftop PVs is about 13.02 GW, three strategies are devised to reduce 25%, 50% and 75% of peak load on the electrical grid by applying PV panels to 28%, 55%, and 83% roof areas, respectively. The three strategies are denoted by ‘PV25’, ‘PV50’ and ‘PV75’, and evaluated using the life-cycle benefit-cost analysis.

Table 4.1 Rooftop photovoltaics potential for the Washington metropolitan region.

Building class	Building footprint (m^2)	Statistics	Suitable roof areas (km^2)	Power generation capacity (GW)
Small	1,000 – 5,000	Mean	81.07	8.44
		95th confidence interval of mean	62.39 – 220.64	6.52 – 22.48
Medium	5,000 – 10,000	Mean	18.22	1.61
		95th confidence interval of mean	13.97 – 58.00	1.24 – 5.09
Large	> 10,000	Mean	37.16	2.97
		95th confidence interval of mean	22.73 – 118.10	1.81 – 9.47
Total		Mean	136.45	13.02
		95th confidence interval of mean	99.09 – 396.74	9.57 – 37.04

The installation and annual maintenance costs of rooftop PV are \$2.6/W and \$0.19/W respectively for commercial buildings, and \$3.2/W and \$0.21/kW respectively for residential buildings at Washington D.C. in 2015 (Kats and Glassbrook 2016). These unit prices are employed in the following analysis. The lifespan of solar panels ranges between 20–30 years, and hence 30 years is used as the analyzed period. The discount rate is 3%, and the residual value of PV panels at the end of life is 0. Energy is required for material production, module manufacture, and transportation. Bhandari et al. (2015) harmonized the results of 34 studies that evaluate life-cycle (30 years) energy consumption of solar PV. On average, mono- and poly-crystalline silicon PV consume the energy of 6225 and 3914 MJ/m^2, respectively. Cadmium telluride (CdTe), copper indium gallium diselenide (CIGS), and amorphous silicon (a-Si) PV require less energy of 1575, 2276, and 1708 MJ/m^2, respectively. The energy cost of solar PV is calculated as electricity expenditure at the beginning of the life cycle. The electricity price of Washington D.C. in 2018 summer ranged between \$0.125–0.132/kWh (BLS 2019), and these values are used in the calculation.

About 60–70% of greenhouse gas emission from solar PV is involved with material extraction and production, module and system component manufacture, and installation process (NREL 2012). The rest of greenhouse gas emission is associated with power generation, system operation and maintenance, and system decommissioning and disposal (NREL 2012). Hsu et al. (2012) harmonized the results of 13 studies that contain 42 estimates of greenhouse gas emission in the life cycle (30 years) of solar PV. The median emission of crystalline silicon PV (monoand poly-crystalline) is about 45 g of equivalent CO_2 per kWh electricity generation (Hsu et al. 2012), which is similar to thin-film PV (CdTe, CIGS, and a-Si) based on the harmonized estimates of five studies (NREL 2012). The unit price recommended by the U.S. Environmental Protection Agency (EPA 2019) is employed to calculate incurred social cost for carbon. The life-cycle cost of solar PV including installation and maintenance, energy consumption, and carbon footprint is summarized in Table 4.2.

Table 4.2 Life-cycle benefits and costs of rooftop photovoltaics (PV) in the Washington metro area, $t_0 = 2015$, $n = 30$ years, $r = 3\%$.

Strategy	Cost (2015 million dollars)	Direct benefit (2015 million dollars)	Direct and indirect benefit (2015 million dollars)
PV25	11,735 – 20,559	10,142 – 12,795	30,501 – 35,330
PV50	23,397 – 40,806	19,997 – 24,410	60,715 – 69,480
PV75	35,132 – 61,365	29,820 – 35,892	90,896 – 103,498

Note: t_0 is the time that the strategy is implemented; n is the number of years; r is the discount ratio. See Equations 4.1–4.3 for details.

The direct benefits from rooftop PV are producing electricity and reducing power outage risks. The annual electricity generation of PV panels in the metro area is about

127.6–141.2 kWh/m^2 (the U.S. average is 216 kWh/m^2), dependent on the tilt degree of roofs (Gagnon et al. 2016). Solar panels degrade at a median rate of 0.5% per year (Jordan and Kurtz 2013), and hence the produced electricity is assumed to decrease by 0.5% per year. Bartos and Chester (2015) predicted that utility-scale PV in the western U.S. may suffer from 0.7–1.7% of capacity reduction in the next forty years due to the rise of summer temperatures. However, the prediction is associated with many uncertainties such as the variation of solar radiation (Bartos and Chester 2015). Therefore, the impacts of temperature rise on PV performance is not considered herein. The calculated annual value of electricity generated by PV panels is $447–611 million for strategy 'PV25', $894–1222 million for strategy 'PV50', and $134–1833 million for strategy 'PV75'.

Momentary disruption (less than 30 minutes) of electricity service can cause a loss of $16,172 per medium and large commercial and industrial customer (over 50,000 annual kWh), $372 per small commercial and industrial customer (under 50,000 annual kWh), and $5.6 per residential customer in 2013 dollars (Sullivan et al. 2015). Long-duration power outages (greater than 30 minutes) are not considered in this study because they are typically caused by catastrophic events such as hurricanes, wind storms, earthquakes. There are about 6,131,977 residents, 209,996 small commercial and industrial customers (employees less than 500), and 3,883 medium and large commercial and industrial customers (employees greater than 500) in the Washington metro area by 2016 (Census 2018), calculated based on population weight in 2016. A power outage has the largest effects on commercial and industrial customers in the morning and afternoon and the greatest impacts on residential customers in the morning and night. Therefore, per disruption of electricity service can cause an economic loss of $34,339,071–140,914,388, dependent on the disruption time (*e.g.*, morning, afternoon, night).

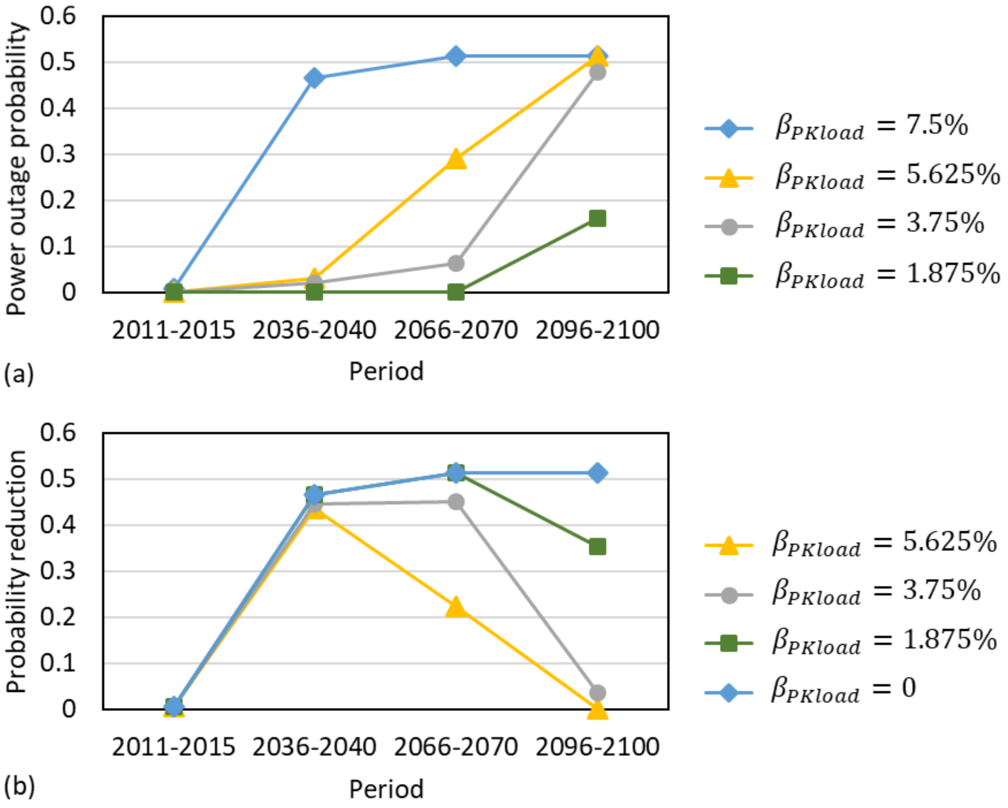

Figure 4.10 Change in power outage probability when peak load factor is reduced. (a) Power outage probability; (b) Reduction in outage probability.

Figure 4.10 shows the change in power outage probability when peak load factor (β_{PKload}) is reduced from 7.5% (reference) to 5.625%, 3.75%, 1.875%, and 0. The change in years out of the periods analyzed is linearly interpolated. The effectiveness of adaptations peaks around the middle of the century, because adaptations lower the growth rate of power outage probability and enlarge outcome difference between adaptation and reference cases. In the second half of the century, the outage probability of the reference case approaches the upper limit (0.514) and grows at an extremely low rate until reaching it, whereas the outage probability of adaptation scenarios rises at a relatively high rate. By the end of the century, peak load may increase by 7.2 GW. Strategies ‘PV25’, ‘PV50’, and ‘PV75’ can add a generation capacity of 3.6, 7.2, and 10.8 GW respectively, which can offset the impact of increased peak load on the grid by 50%, 100%, and 100% respectively. The benefits of the three strategies in mitigating power outage risk is calculated using Equation 4.3 and summarized in Table D3.

The indirect benefits (co-benefits) of rooftop PV analyzed in this study include reducing fine particles PM2.5 concentration and decreasing greenhouse gases emission. Machol and Rizk (2013) indicated that PM2.5 discharged by coal, natural gas and oil power plants can lead to public health loss of $0.19/ kWh, $0.01/kWh and $0.08/kWh, respectively. In 2018, the natural gas, coal, and petroleum contributed to 39%, 31%, and 7% of total electricity generation respectively in the mid-Atlantic region (NERC 2018), meaning per unit (kWh) electricity production in the Washington metro area can result in $0.0684 equivalent loss of public health. Greenhouse gas emitted from power plants contains Carbon Dioxide (CO_2), Methane (CH_4) and Nitrous Oxide (N_2O). The U.S. Environmental Protection Agency (EPA) published greenhouse gas inventories per unit electricity production (EPA 2018), and the projected social cost per unit emission of CO_2, CH_4, and N_2O for the years 2015–2050 (EPA 2019). The social costs later than 2050 are calculated by linear extrapolation in this study. The social cost for greenhouse gases and extrapolation results are presented in Table D4 and Table D5, respectively. Three discount rates (5%, 3%, and 2.5%) are adopted by EPA to account for uncertainties associated with socioeconomic conditions. The 3% discount rate is employed in this study to keep consistent with the above analysis. The life-cycle benefit of PV including direct and indirect benefits are summarized in Table 4.2.

This study assumes that the benefit and cost are normally distributed, the mean for the two distributions are the averages of upper and lower boundaries, and the standard deviation for the two distributions are one-sixth of the differences between upper and lower boundaries. The mean and standard deviation of the cost distribution $C \sim N(\mu_C, \sigma_C^2)$ and benefit distribution $B \sim N(\mu_B, \sigma_B^2)$ is delineated in Table D6.

Table 4.3 compares the three strategies based on four decision metrics. The mean net present value (NPV) measures the present value of mean net benefits, and results indicate that using more rooftop PV tends to produce more benefits. The probability that direct benefit is greater than the cost, $P(B_{direct} > C)$, decreases as the use of PV panels increases, because the direct benefit increases slightly but the cost rises greatly for per unit increment of PV panels. The benefit-cost ratio (γ) of the three strategies is around 2.0, and the ratio drops slightly as the use of PV panels increases due to the same reason. The total benefit is certain to be greater than the cost of the three strategies.

Table 4.3 Benefit-cost analysis for rooftop photovoltaics (PV) in the Washington metro area, $t_0 = 2015$, $n = 30$ years, $r = 3\%$, 2015 dollars.

Strategy	Decision metrics			
	Mean net present value ($NPV = \mu_B - \mu_C$)	Benefit-cost ratio ($\gamma = \mu_B/\mu_C$)	$P(B > C)$	$P(B_{direct} > C)$
PV25	$16,769 million	2.0385	1	0.0012
PV50	$32,996 million	2.0279	1	0.0005
PV75	$48,249 million	2.0145	1	0.0003

Note: t_0 is the time that the strategy is implemented; n is the number of years; r is the discount ratio. See Equations 4.1–4.3 for details.

4.4.4 Timing of adaptation

Strategy optimization seeks appropriate timing for the adaptation to enable the investment to be most cost-effective. This study compares the cost and benefit of installing PV panels in later years 2040 and 2070 to the baseline year 2015. The summer peak electricity load of Washington metropolitan area is assumed to be constant, and thereby the strategies ‘PV25’, ‘PV50’ and ‘PV75’ imply the same amount of roof areas as the baseline case. This assumption enables that adaptation timing is the only variable in the analysis. Moreover, the installation price for PV panels drops by 1% each year, considering that decreased materials prices, government funds and supports, and improved technology and productivity have caused a significant decline of PV installation cost (Kavlak et al. 2018).

Table 4.4 and Table 4.5 present the benefit-cost results for the three strategies implemented in 2040 and 2070, respectively. Comparing Table 4.3–Table 4.5, the mean net present value and the benefit-cost ratio are greater for rooftop PVs installed in later years because of the decreased costs of PV panels and increased potential benefits over time. The direct benefits decrease due to declined risk reduction on power outages in the second half of the century, and the 3% discount rate that reduces the present value. Elevating discount rate can lower decision metric values while reducing the discount rate can increase decision metric values. Increases in decision metric values imply increases in the cost-effectiveness of investments. Although direct benefits are unlikely to surpass the costs of rooftop PVs ($P(B_{direct} > C) = 0$) installed in 2040 and 2070, the total benefits that account for environmental impacts are certain to be greater than the costs ($P(B > C) = 1$).

Table 4.4 Benefit-cost analysis for rooftop photovoltaics (PV) in the Washington metro area, $t_0 = 2040$, $n = 30$ years, $r = 3\%$, 2015 dollars.

Strategy	Decision metrics			
	Mean net present value ($NPV = \mu_B - \mu_C$)	Benefit-cost ratio ($\gamma = \mu_B/\mu_C$)	$P(B > C)$	$P(B_{direct} > C)$
PV25	\$20,534 million	2.9002	1	0
PV50	\$40,807 million	2.8963	1	0
PV75	\$60,947 million	2.8854	1	0

Note: t_0 is the time that the strategy is implemented; n is the number of years; r is the discount ratio. See Equations 4.1–4.3 for details.

Table 4.5 Benefit-cost analysis for rooftop photovoltaics (PV) in the Washington metro area, $t_0 = 2070$, $n = 30$ years, $r = 3\%$, 2015 dollars.

Strategy	Decision metrics			
	Mean net present value ($NPV = \mu_B - \mu_C$)	Benefit-cost ratio ($\gamma = \mu_B/\mu_C$)	$P(B > C)$	$P(B_{direct} > C)$
PV25	\$22,976 million	4.7136	1	0
PV50	\$45,952 million	4.7252	1	0
PV75	\$68,820 million	4.7155	1	0

Note: t_0 is the time that the strategy is implemented; n is the analyzed period; r is the discount ratio. See Equations 1–3 for details.

4.5 Conclusions

Adapting electricity systems to rising temperatures is important to the nation's energy security. This study systematically and quantitatively evaluates the vulnerability of the electricity system in the rest of the 21st century for the Washington metro area, comprehensively assesses the cost-effectiveness of implementing rooftop photovoltaics (PV) in the area, and creatively employs probabilistic risk analysis to enhance climate adaptation planning. Based on the RCP 8.5 scenario, the failure probability of the electrical grid is projected to grow continuously and at a greater rate in the second half the century. By 2100s, the probability of power outage in this area may increase seventyfold if no adaptation action is taken.

The roof area suitable for solar PV is about 136.45 km^2 in the Washington metro area, which can add an average generation capacity of 13.02 GW to the existing power system. The capacity can vary with weather conditions and decrease over time due to module degradation. In addition, there is no electricity generation from PV panels at night, and battery storage technology can be employed to fill the gap. Deploying rooftop PV helps lower summer cooling loads on power grids and reduce the risk of power outages. The life-cycle benefit-cost analysis suggests that increasing the usage of PV panels can improve cost effectiveness, and implementing PV strategies at an earlier time can elevate cumulative benefits in the long run. The net benefits of PVs may be more pronounced in the future because of declined material and installation prices and increased social cost for carbon emission.

Overall, the findings of this study would help local governments and stakeholders foresee potential risks and plan and initiate appropriate adaptations for the electric power system. The assessment on rooftop PV strategies would help improve regional energy system resilience and sustainability. The methods presented in this study are transferrable to the analysis of other places.

Chapter 5: Conclusions and Implications

5.1 Major findings

This dissertation projected future trends and levels of the UHI effect and heat waves in Washington D.C. and its surrounding areas. The projection was made by using the ARRM to downscale CMIP5 data into the location of observing stations. The ARRMs developed in this research shows satisfactory performance in reproducing observed temperatures and temperature distributions, although the errors of projection caused by the shift of the observation-simulation relationship are not treatable by statistical means. Projections of the higher scenario RCP 8.5 suggested that the UHI effect would be stronger in summer, especially at nighttime, and weaker in winter. The daytime and nighttime UHI intensity may increase to about 2.7°C and 6.5°C on an extremely hot summer day (the 99th percentile of temperature distribution) by 2100, respectively. The maximum amplitude of heat waves may increase continually to around 52.4°C by 2100. Annual duration counts the number of heat wave days in a year, and can increase to three months by 2100. In addition, warm days and nights may triple by the end of the century. Projections of the lower scenario RCP 2.6 indicated that the UHI effect of Washington D.C. would be similar to the current condition. The nighttime intensity may increase slightly in summer and decrease slightly in winter. The maximum amplitude and annual duration of heat waves may decline after a half-century of growth. Warm days and nights may share the same pattern of change.

This dissertation further investigated the temporal and spatial variation of heat waves in the Washington metro area. The WRF model was used to downscale CESM1 data into fine-grid results, and this method shows remarkable performance in reproducing heat wave characteristics. Projections forced by the higher scenario RCP 8.5 indicated that the amplitude of heat waves may grow by 5.7°C, and frequency and duration may triple in Washington D.C. by the end of the century. Urban areas tend to suffer from higher amplitude and longer duration compared to other places. Rural areas may experience at least one heat wave every five years by the mid of the century. Warm spell duration counts the number of heat wave days in a year, and can increase to two months in urban areas and more than one month in rural areas by the end of the century. Moreover, UHIs play an important role in heat wave growth even though global climate change may dominate the evolution.

Five mitigation strategies for heat waves were evaluated in three future periods using the WRF model. Results indicated that elevating albedo of roofs from 0.3 (conventional roofs) to 0.6 (cool roofs) can lead to 0.6–0.8°C drop in heat wave amplitude and 6–9 days decline in warm spell duration at Washington D.C. Raising urban pavement albedo from 0.15 (asphalt pavements) to 0.3 or 0.45 (reflective pavements) has a negligible effect on heat wave amplitude but can reduce warm spell duration by about 2 days. Green roofs show a better performance in heat wave mitigation compared to cool roofs and reflective pavements. Replacing conventional roofs with 50% and 100% green roofs can reduce heat wave amplitude by 0.5–0.7°C and 0.9–1.3°C and lessen warm spell duration by 5–8 and 9–13 days, respectively. In addition to moderating urban temperatures, the five strategies weaken the wind flowing from rural to urban areas and increase humidity in the metropolitan region during the day. Heat wave amplitudes and warm spell duration decrease almost linearly as roof and pavement albedo and green roof fraction increase. Elevating surface albedos or increasing green roofs is more effective in reducing hot temperatures during the day compared to the night.

Evaluation results indicated that reflective pavements may not be as effective as green roofs and cool roofs in moderating heat waves for Washington D.C. This is because cool roofs are typical of a higher albedo and reflect more solar radiation than reflective pavements do, and green roofs enhance evaporative cooling while reflective pavements hinder it (see Chapter 3). In addition, tall buildings surrounding reflective pavements can cause multiple reflections, resulting in most solar radiation absorbed by road and building surfaces (Qin 2015). The multiple reflections were not simulated in the WRF model, meaning the performance of reflective pavements can be lower than our simulation. However, the low cost in installation and maintenance may make reflective pavements to be a cost-effective strategy and even more cost-efficient than green roofs (see Appendix E).

This dissertation also projected the vulnerability of the electricity system to temperature rise in the Washington metro area. Results indicated that by the end of the century, the probability of power outage may increase seventyfold if no adaptation action is taken. If the peak load on the electrical grid is cut by three quarters, the outage probability may rise twentyfold instead. This reduction is achievable by installing solar panels on building roofs. The suitable roof area for solar PV in the metro area is about 136.45 m^2, which can add a generation capacity of 13.02 GW to the existing power system.

A comprehensive cost-benefit assessment on rooftop PV strategies suggested that the benefits of using rooftop PV to reduce peak load on power grids by 25%, 50%, and 75% are significantly greater than the costs when environmental impacts are considered. In addition, increasing the usage of PV panels can enhance cost effectiveness, and implementing PV strategies at an earlier time can increase cumulative benefits in the long run. The net benefits of PVs may be more pronounced in the future because of declined material and installation prices and increased social cost for carbon emission.

5.2 Major contributions

The first major contribution of this dissertation is providing accurate and reliable future projections on the UHI effect and heat waves for the Washington metro area. Previous projections either covered a broad region that cannot properly represent local conditions, or downscaled the old version of global climate models that cannot reflect the latest worldwide experiments on climate modeling. This dissertation overcame those limitations and produced station-based projections in Table 2.2 and Table 2.3, and fine-grid projections in Figure 3.4, which can be used by climate researchers, stakeholders, policymakers, and engineering participators for impact assessment, adaptation planning, and policy analysis.

Secondly, the trend and level of the UHI effect and heat waves characterized in this research would help cities, particularly Washington D.C., foresee potential risks in the future. The potential risks may include heat-related illness and deaths, power outage, road damage, and air and water quality deterioration. The fine-grid projection of heat waves in this research would help locate vulnerable populations and assets in the Washington metro area and assist local climate preparation.

Thirdly, this dissertation improved the understanding of heat wave mitigation techniques for cities. Compared to accommodating cities to increased extreme heat, mitigation has the advantages in addressing such a challenge from its root cause and enabling long-term risk reduction. The effectiveness of cool roofs, green roofs, and reflective pavements was assessed under intensified future climate conditions. The uncertainties associated with the efficacy of mitigation strategies were analyzed to assist decision making.

Fourthly, this dissertation provided new insights into the vulnerability assessment of electricity systems. In this assessment, high-resolution temperature projections, summer cooling load predictions, electrical network model, and system failure model were incorporated to quantitively and systematically evaluate the change of grid vulnerability in the future. In addition, this research revealed that cooling load growth may dominate the increase of grid vulnerability during summer, and reducing peak load on power grids can reduce the susceptibility level considerably during hot days. These findings, among others, may help governments and stakeholders take appropriate actions to improve the resilience of electricity systems.

Lastly, this dissertation proposed a new framework to support adaptation planning and decision making. This framework incorporating probabilistic risk approach to improve uncertainty and sophisticated relations modeling. This framework was utilized to assess and optimize rooftop PV strategies for the Washington metro area, which would assist in adaptation and resilience planning for the electric sector.

Overall, this research is especially timely in the aftermath of the Paris Agreement taking effect in 2016, which calls on climate-change mitigation and adaptation efforts in global and local communities. The findings of this dissertation would assist in ongoing climate and energy planning of Washington D.C. and provide guidance for other cities. The methods proposed and employed in this dissertation can be modified to study other regions.

5.3 Implications for future research

The limitations of this dissertation are addressed as implicit recommendations for future research. First and foremost, this dissertation defined a heat wave as at least six consecutive days in which maximum temperatures exceed the local 90th percentile of the control period from 1961 to 1990. This definition has been employed by a number of studies. However, human's bearing capacity to extreme heat may change over time because of acclimatization. Using the definition designed for the period of 1961–1990 may be unsuitable for future time periods. For example, the annual duration of heat waves projected in this dissertation is surprisingly long (2–3 months) by the end of the 21st century. This limitation can be solved by setting the control period closer to the projected period.

Secondly, the statistical downscaling method is built on the assumption that the relationship between model simulation and observation is time invariant. In this research, observational analysis indicates that the temperature difference between the city and suburbs was decreasing because of the rapid development of suburbs. However, the future projection shows a growing trend of the temperature difference, because the urbanization process of suburbs is not simulated in the model. To account for urban growth, the statistical relationship between model simulation and observation should be updated periodically based on assumed socioeconomic development scenarios. Furthermore, the quantile relationship between observation and simulation is developed based on historical datasets, and data points exceeding historical range are hard to predict. This research used linear extrapolation to treat those data points but resulted in an overestimation of extreme hot temperatures. Therefore, this statistical method is suitable for projecting relatively stable climate variables or short-term change of climate conditions.

Thirdly, urban climate modeling can greatly affect dynamical downscaling results. This research incorporated the single-layer urban canopy model into the WRF model in order to improve urban climate simulation. Choosing a more sophisticated model (*e.g.*, multiple-layer urban canopy model, Princeton urban canopy model) can help improve projection accuracy although this typically requires more computation resource. In addition, using appropriate values for urban parameters is important to climate modeling. This research determined those values based on district regulations, which may not match real-world conditions. The most effective way is to use local data for building height and width, road width, anthropogenic heat, and other variables. Moreover, this research used land information collected in 2011 to project future temperatures, which may weaken the accuracy of projection results, because land use is very likely to change in the future, and the change in land cover can greatly affect local climate. Unfortunately, reliable projections for land cover were unavailable at the time of this research. Future research may use projected land information in the WRF model to avoid accuracy loss.

Lastly, the failure probability measured in this dissertation is an indicator of grid vulnerability to temperature rise, rather than the likelihood of service interruption in the real world, because service failure can also be triggered by equipment aging, extreme weather (e.g., hurricane, windstorm), wildlife, and other factors. Future research can expand the probabilistic risk model (adding up conditional probabilities of other events) to account for the impacts of multiple factors on electricity system failure. Moreover, the electrical power grid assessed in this research for the

Washington metro area is affected by the national grid. The national grid may feed additional power into the system or consume power generated by the system, which is not considered. Future research can use historical operation data to update the network model. In addition, this research assumed identical electricity demand in each supply node, but real-world energy demands can be spatially uneven. Future research may use high-resolution population data or other available data to determine the spatial distribution of electricity demands and update the network model.

Appendix A: Comparisons of statistical and dynamical downscaling results

This dissertation utilized two methods to project the urban heat island (UHI) effect and heat waves for Washington D.C. The first method uses the Asynchronies Regional Regression Model (ARRM) that statistically downscales the Coupled Model Intercomparison Project Phase Five (CMIP5) data to the location of station-based observation. The second method employs Weather Research and Forecasting (WRM) model that dynamically downscales the Community Earth System Model version one (CESM1) data to finer grid results. The following section compares the results generated by the two methods.

Table A1. A comparison of statistical and dynamical downscaling methods.

Model	ARRM	WRF model
Purpose	Statistical downscaling	Dynamical downscaling
Input GCM data	10 GCMs of CMIP5	Bias corrected CESM1
Climate scenario	RCP 2.6, RCP 8.5	RCP 8.5
Training period	1965–2000	N/A
Validation period	1965–2000 2001–2005	2011–2015
Projected periods	2016–2035 2046–2065 2086–2099	2036–2040 2066–2070 2096–2100

Projected items	Daily maximum and minimum temperatures at the locations of four observing stations	3-hourly temperature, humidity, and wind speed at a grid resolution of 4×4 km for Domain 3 and 1.3×1.3 km for Domain 4
Projection of UHI intensity	Temperature difference between the average of two stations at the city and the average of two stations at suburbs	Temperature difference between Domain 4 (excluding nonurban areas) and Domain 3 (excluding urban areas)
Projection of heat waves*	Maximum amplitude, annual duration	Mean and maximum amplitude, frequency, duration, warm spell duration
Projection of warm days and nights	TX90p, TN90p	N/A
Projection of heat wave mitigation outcomes	N/A	Reduction of heat wave amplitude, reduction of warm spell duration

Note: *Only the year with at least a heat wave is considered in the statistical downscaling results, while all years in the analyzed period are counted in the dynamical downscaling results.

Table A2. Station comparisons between statistical and dynamical downscaling methods.

Location	ARRM	WRF
38.91°N, -76.97°W	Station 1	Station 17
38.94°N, -77.11°W	Station 2	Station 19
38.94°N, -77.46°W	Station 3	Station 18
38.87°N, -76.78°W	Station 4	Station 14

Figures A1-A4 present simulated and observed daily maximum temperature distributions (May–September) at the locations of four weather stations. The ARRM shows satisfactory performance in simulating the mean and right tail of historical temperature distribution but fails to capture the left tail (Figures A1a, A2a, A3a, and A4a). However, in chapter 2, ARRM perfectly captures observation distributions during 1965–2000 (Figure 2.5). This is because the ARRM is developed based on datasets of 1965–2000, but the statistical relationship between the observation and simulation changes over time (Figure 2.9). The WRF model shows remarkable performance in reproducing temperature distributions at the four stations (Figures A1b, A2b, A3b, and A4b). However, the mean of the temperature distribution at Station 1 is slightly underestimated (Figure A1b).

The projection results of ARRM and WRF model are compared in three time periods. The scenario RCP 8.5 is adopted in the projection. The ARRM projects a significant shift in the distribution towards high temperatures. The number of days with high temperatures may increase considerably, while the number of days with medium and low temperatures may decrease substantially. The projection of the WRF model is more conservative compared to the ARRM. The WRF model projects a relatively small shift of the distribution towards high temperatures, and the shape of the distribution hardly changes over time. The low, medium, and high temperatures may increase at the same rate.

A recent report from Vox Media in collaboration with NASA’s Jet Propulsion Laboratory and the Scripps Institution of Oceanography (Irfan et al. 2019) suggested that summer high temperature of Washington D.C. may increase by 2.3–2.7°C (4.1–4.8°F) in 2036–2065. This prediction is close to WRF’s projection of 2.9°C in 2066–2070 and is lower than ARRM’s projection of 5.3°C in 2046–2065. The ARRM may overpredict extreme hot temperatures, and the degree of overestimation may increase when the predicted period is far away from the baseline period. The overprediction is attributable to the linear extrapolation method used in this research to project data points out of the historical range.

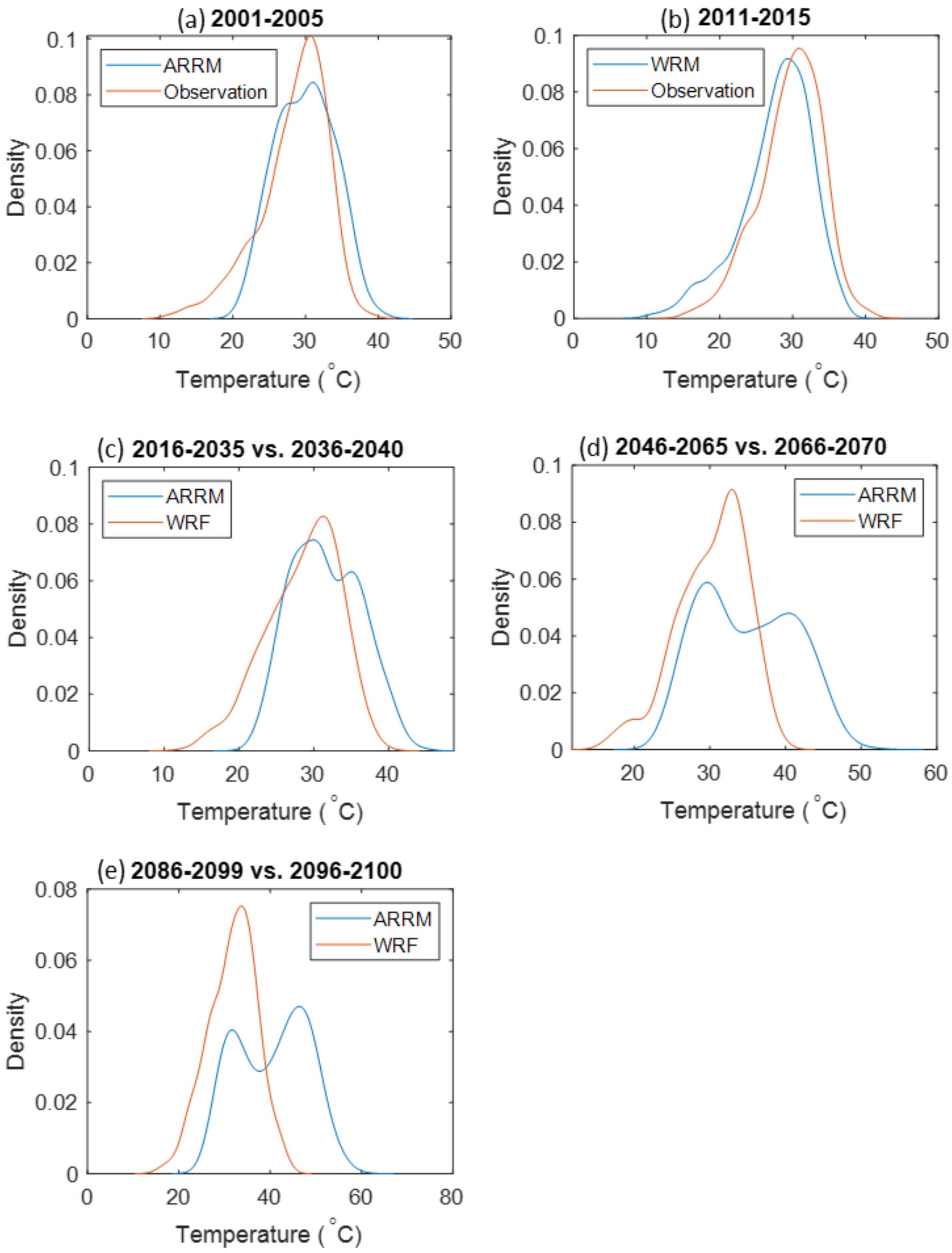

Figure A1. Daily maximum temperature distribution at Station 1. (a) ARRM simulation compared to observation during 2001–2005; (b) WRF simulation compared to observation during 2011–2015; (c) ARRM projection for 2016–2035 compared to WRF projection for 2036–2040 under RCP 8.5; (d) ARRM projection for 2046–2065 compared to WRF projection for 2066–2070 under RCP 8.5; (e) ARRM projection for 2086–2099 compared to WRF projection for 2096–2100 under RCP 8.5.

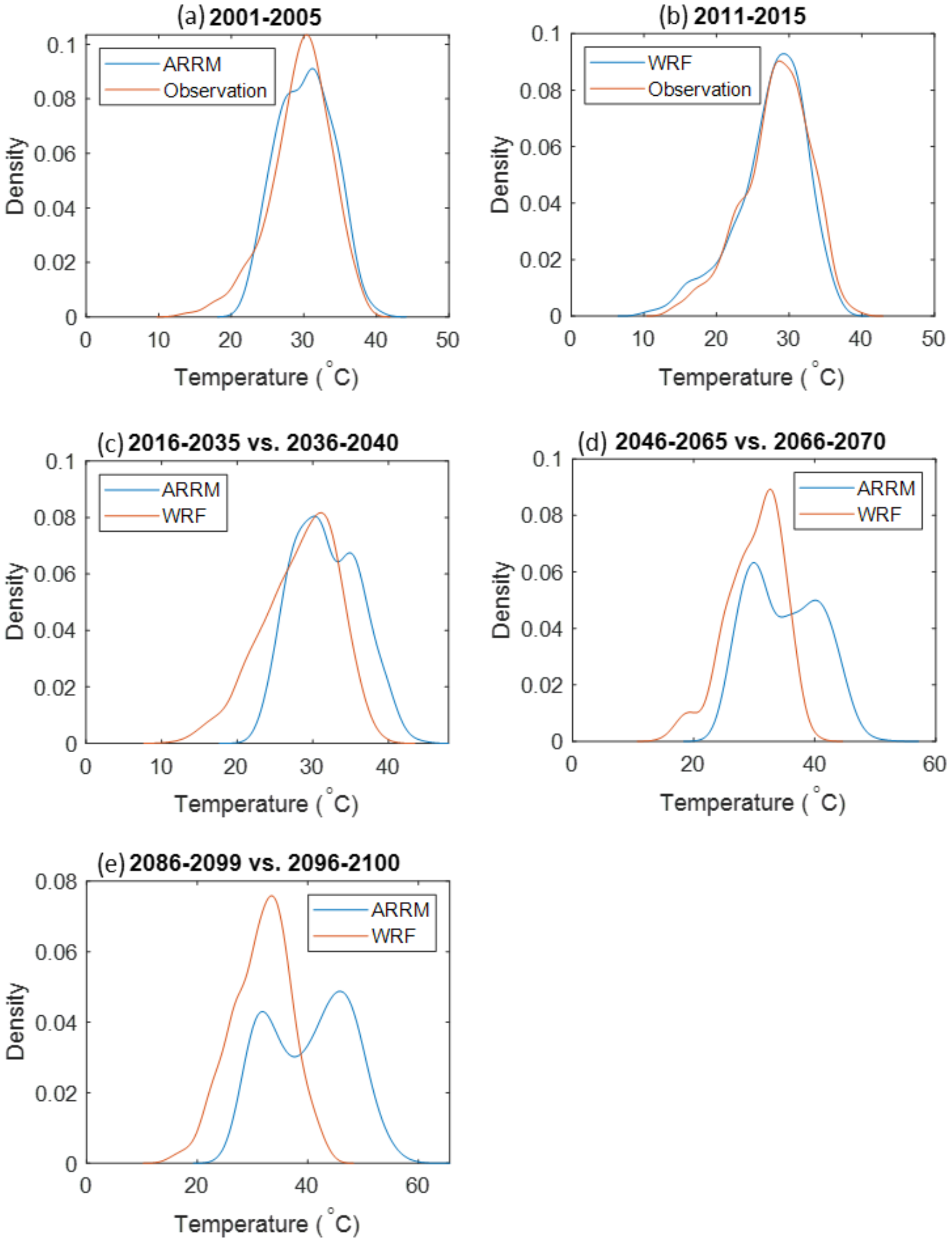

Figure A2. Daily maximum temperature distribution at Station 2. (a) ARRM simulation compared to observation during 2001–2005; (b) WRF simulation compared to observation during 2011–2015; (c) ARRM projection for 2016–2035 compared to WRF projection for 2036–2040 under RCP 8.5; (d) ARRM projection for 2046–2065 compared to WRF projection for 2066–2070 under RCP 8.5; (e) ARRM projection for 2086–2099 compared to WRF projection for 2096–2100 under RCP 8.5.

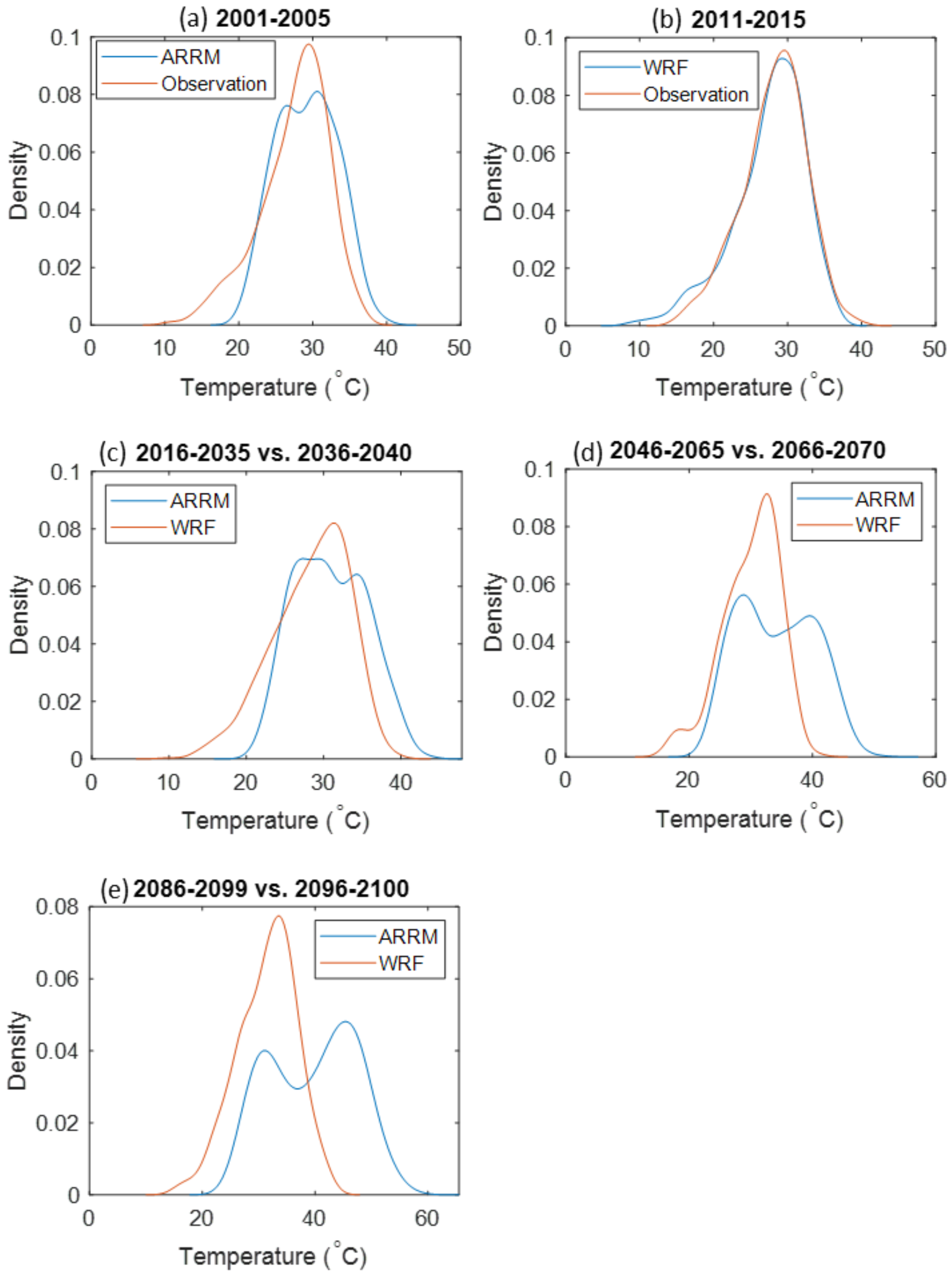

Figure A3. Daily maximum temperature distribution at Station 3. (a) ARRM simulation compared to observation during 2001–2005; (b) WRF simulation compared to observation during 2011–2015; (c) ARRM projection for 2016–2035 compared to WRF projection for 2036–2040 under RCP 8.5; (d) ARRM projection for 2046–2065 compared to WRF projection for 2066–2070 under RCP 8.5; (e) ARRM projection for 2086–2099 compared to WRF projection for 2096–2100 under RCP 8.5.

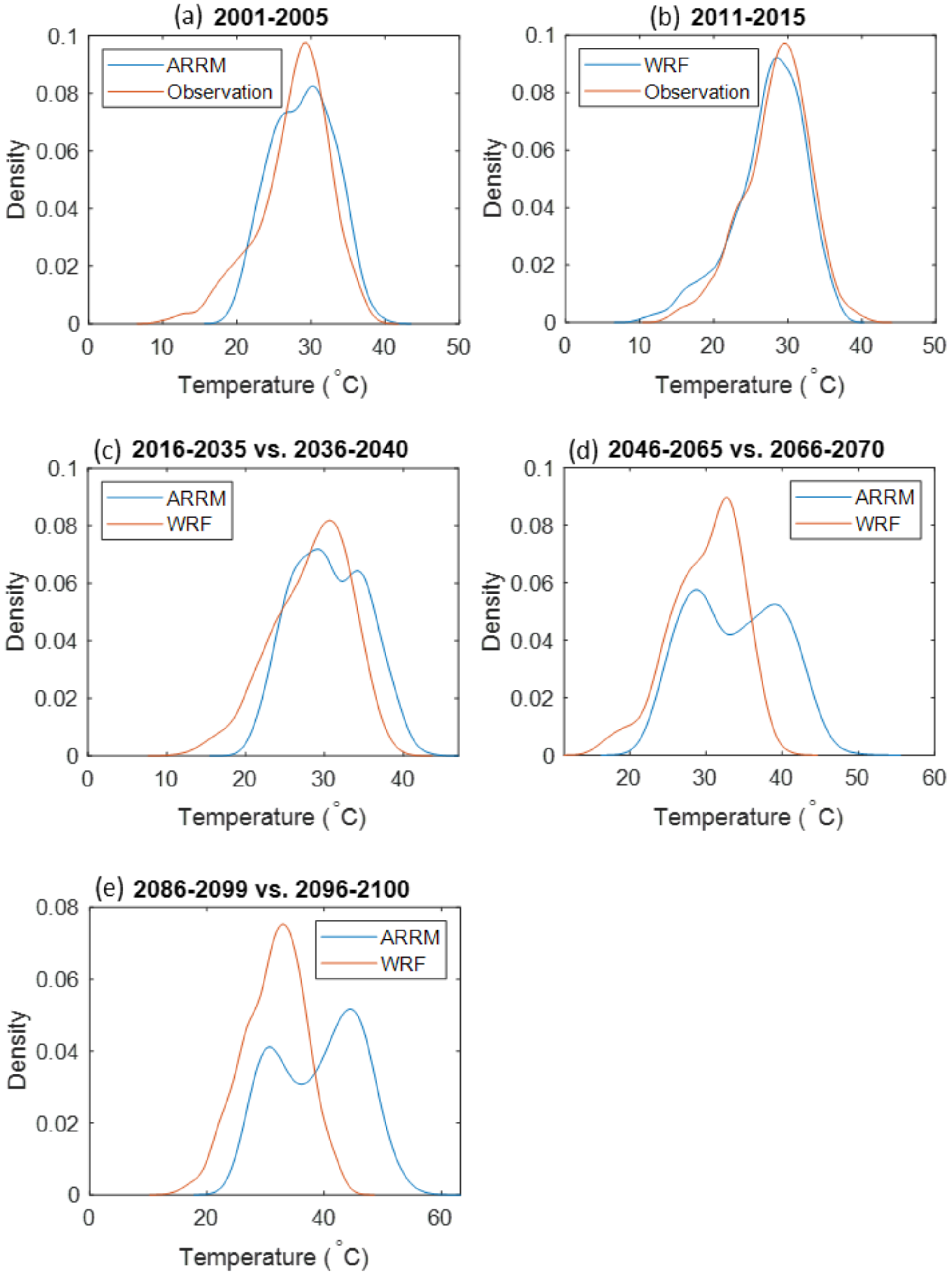

Figure A4. Daily maximum temperature distribution at Station 4. (a) ARRM simulation compared to observation during 2001–2005; (b) WRF simulation compared to observation during 2011–2015; (c) ARRM projection for 2016–2035 compared to WRF projection for 2036–2040 under RCP 8.5; (d) ARRM projection for 2046–2065 compared to WRF projection for 2066–2070 under RCP 8.5; (e) ARRM projection for 2086–2099 compared to WRF projection for 2096–2100 under RCP 8.5.

Appendix B: Mechanisms of dynamical downscaling

The Weather Research and Forecasting (WRF) model has been developed to a software program for convenient use and easy access. The software provides a set of services before, during and after running WRF simulation, including data preprocessing, data assimilation, dynamics solvers, and post-processing. The Advanced Research WRF (ARW) is one of the dynamics solvers that deal with model initialization and simulation under predetermined physical schemes and numerics/dynamics options. Detailed information on the software and the ARW solver are documented in the NCAR technical note (NCAR 2017a). The WRF model requires 3-dimensional inputs of temperature, wind speed, geopotential height, and relative or specific humidity, and 2-dimensional inputs of surface pressure, mean sea level pressure, skin temperature, 2-meter temperature, 2-meter relative or specific humidity and 10-meter wind speed. Optional inputs include soil temperature, soil moisture and so on, depending on research needs. For the downscaling purpose, inputs are obtained from global climate models.

Table 3.1 lists the physical schemes employed in this study. The single-moment 6-class (WSM6) microphysics scheme is used to simulate the microphysics of water vapor, cloud, and precipitation processes (Hong and Lim 2006). The Noah land surface model is a four-layer soil temperature and moisture model that calculates sensible and latent heat fluxes for the boundary layer scheme (Chen and Dudhia 2001). Urban canopy model estimates the surface temperature and heat fluxes from the roof, wall and road surfaces, and computes the momentum exchange between urban surface and atmosphere. Urban canopy model (UCM) and Noah land surface model (LSM) together can categorize urban land uses to three types: low-density residential, high-density residential, and commercial/high-intensity industrial lands. Mellor-Yamada-Janjic (MYJ) planetary boundary layer scheme solves vertical fluxes (Janjic, 1996, 2002). The Eta surface layer scheme (Janjic 1996, Janjic 2002) deals with friction velocities and exchange coefficients for the land surface model and planetary boundary layer scheme. The rapid radiative transfer model (RRTM) (Mlawer et al. 1997) is responsible for the radiative flux divergence and surface downward longwave. Dudiha scheme (Stephens 1978) is accountable for shortwave radiation for the ground heat budget.

The following section gives a brief introduction to the physical mechanisms of the (WRF) model in simulating 2-m air temperatures. More detailed information is provided by Skamarock *et al*. (2008) and Li *et al.* (2014). In the Earth's surface energy balance, the net radiation/ radiative flux (R_n) is a sum of three kinds of energy: the heat energy transferring from Earth's surface to atmosphere by conduction and convection, termed sensible heat flux (H_S); the heat energy transferred through water evaporation or condensation (*e.g.*, soil evaporation, plant evapotranspiration), called latent heat flux (H_L); and the heat energy transferring from Earth's surface to its subsurface via conduction (*e.g.*, buildings, grounds), named ground/ storage heat flux (H_G). The subsurface absorbs solar radiation during the day and emits heat energy at night. The equation of the energy balance can be expressed as follows:

$$R_n = H_S + H_L + H_G \tag{B1}$$

2-m air temperature (T_2) refers to the air temperature at two meters above the surface. T_2 is directly associated with skin surface temperature (T_s), and is calculated as follows:

$$T_2 = T_s - \frac{H_S}{\rho_a C_{h2} U_2} \tag{B2}$$

where ρ_a is the air density. U_2 is the wind speed at 2 m above the surface. C_{h2} is the heat transfer coefficient at 2 m above the surface.

For urban grid cells, urban canopy model calculates heat flux of impervious surfaces like buildings, roads, while the Noah land surface model computes heat flux of vegetated areas such as parks, grasslands, trees. Urban percentage ($f_{imprevious}$), also called urban fraction, is the ratio of impervious area to an urban grid-cell area (Chen *et al.* 2011). The sensible heat flux of an urban grid can be expressed as follows:

$$H_s = f_{imprevious} \times H_{s,imprevious} + (1 - f_{imprevious}) \times H_{s,vegetated} \tag{B3}$$

where $H_{s,imprevious}$ and $H_{s,vegetated}$ are sensible heat flux on the impervious part and vegetated part, respectively. Inserting Equation B3 to Equation B2 yields the expression of 2-m air temperature as follows:

$$T_2 = T_s - \frac{f_{imprevious} \times H_{s,imprevious} + (1 - f_{imprevious}) \times H_{s,vegetated}}{\rho C_{h2} U_2} \quad \text{(B4)}$$

For nonurban grid cells, Noah LSM generates all the heat flux results for the boundary layer scheme.

In this study, the vertical dimension of the WRF model comprises 35 sigma vertical levels from the Earth’s surface to the 50-hPa pressure level. The height and thickness of the vertical levels are as follows:

Level = 1 Height = 0.0 m (surface)
Level = 2 Height = 56.6 m Thickness = 56.6 m
Level = 3 Height = 137.9 m Thickness = 81.4 m
Level = 4 Height = 244.7 m Thickness = 106.8 m
Level = 5 Height = 377.6 m Thickness = 132.9 m
Level = 6 Height = 546.3 m Thickness = 168.7 m
Level = 7 Height = 761.1 m Thickness = 214.8 m
Level = 8 Height = 1016.2 m Thickness = 255.0 m
Level = 9 Height = 1372.7 m Thickness = 356.6 m
Level = 10 Height = 1742.4 m Thickness = 369.7 m

Level = 11 Height = 2126.4 m Thickness = 384.0 m

Level = 12 Height = 2525.9 m Thickness = 399.5 m

Level = 13 Height = 3280.4 m Thickness = 754.6 m

Level = 14 Height = 4035.0 m Thickness = 754.6 m

Level = 15 Height = 4789.5 m Thickness = 754.6 m

Level = 16 Height = 5544.1 m Thickness = 754.6 m

Level = 17 Height = 6298.6 m Thickness = 754.6 m

Level = 18 Height = 7053.2 m Thickness = 754.6 m

Level = 19 Height = 7807.7 m Thickness = 754.6 m

Level = 20 Height = 8562.3 m Thickness = 754.6 m

Level = 21 Height = 9316.9 m Thickness = 754.6 m

Level = 22 Height = 10071.4 m Thickness = 754.6 m

Level = 23 Height = 10826.0 m Thickness = 754.6 m

Level = 24 Height = 11580.5 m Thickness = 754.6 m

Level = 25 Height = 12335.1 m Thickness = 754.6 m

Level = 26 Height = 13089.6 m Thickness = 754.6 m

Level = 27 Height = 13844.2 m Thickness = 754.6 m

Level = 28 Height = 14598.7 m Thickness = 754.6 m

Level = 29 Height = 15353.3 m Thickness = 754.6 m

Level = 30 Height = 16107.9 m Thickness = 754.6 m

Level = 31 Height = 16862.4 m Thickness = 754.6 m

Level = 32 Height = 17617.0 m Thickness = 754.6 m

Level = 33 Height = 18371.5 m Thickness = 754.6 m

Level = 34 Height = 19126.1 m Thickness = 754.6 m

Level = 35 Height = 19880.6 m Thickness = 754.6 m

The impacts of five adaptation strategies on surface temperature are illustrated in Figure B1. Figure B2 shows surface temperature shift as the albedo of roofs and pavements rises and as the fraction of green roofs increases.

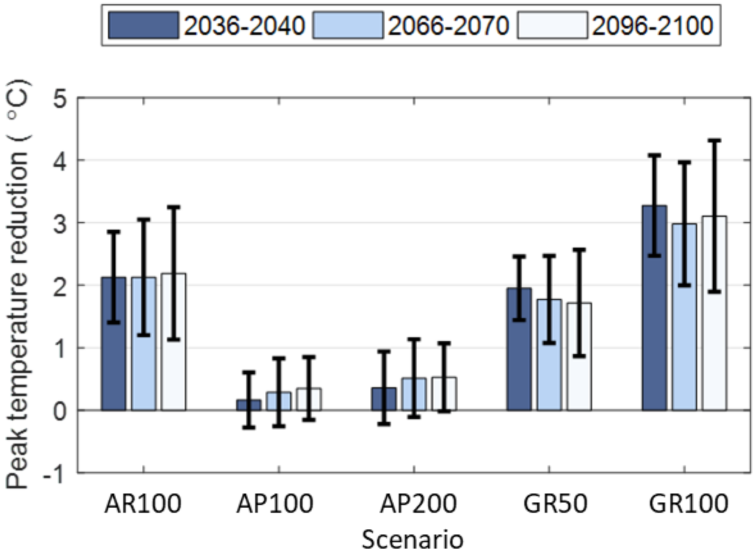

Figure B1. Impacts of five adaptation strategies on the peak surface temperature of the hottest heat wave in the periods of 2036–2040, 2066–2070, and 2096–2100 at Washington D.C. All results are averaged over urban grid cells in Domain 4. Error bars denote standard deviation over those grid cells.

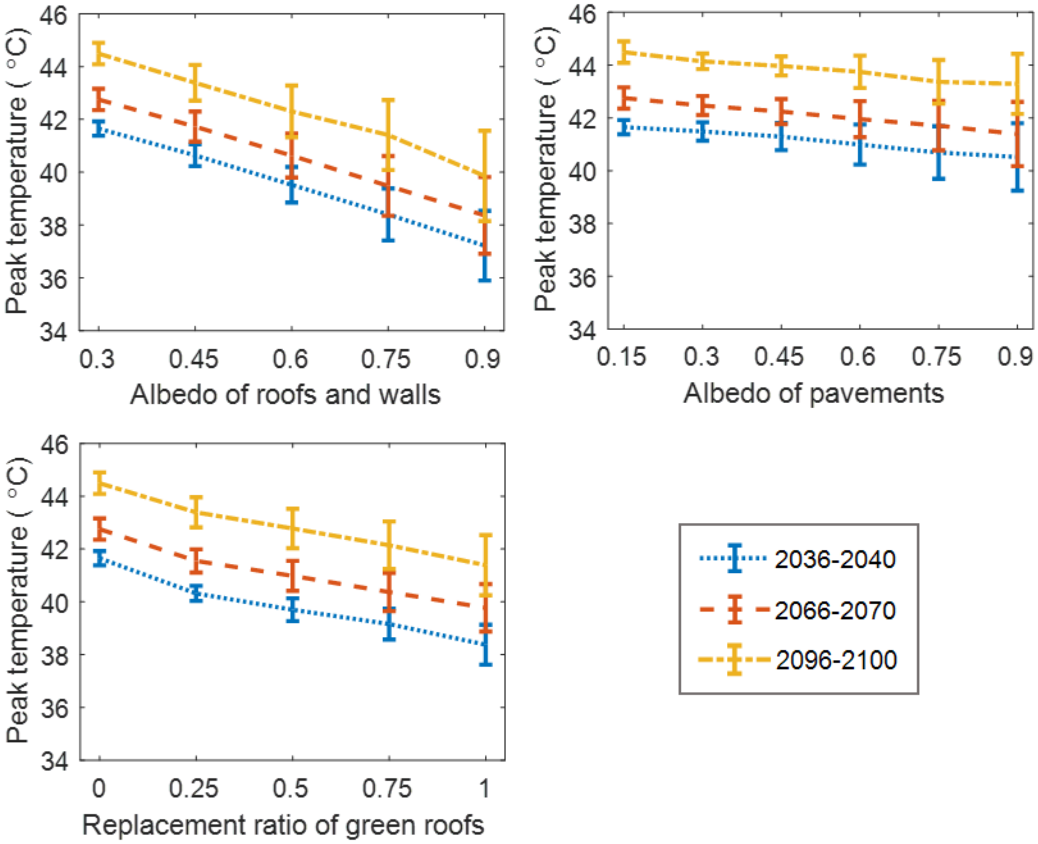

Figure B2. Peak surface temperature of the hottest heat wave as a function of roof and wall albedo, pavement albedo, and green roof fraction in Washington D.C. for the period 2036–2040, 2066–2070, and 2096–2100. All results are averaged over urban grid cells in Domain 4. Error bars denote standard deviation over those grid cells.

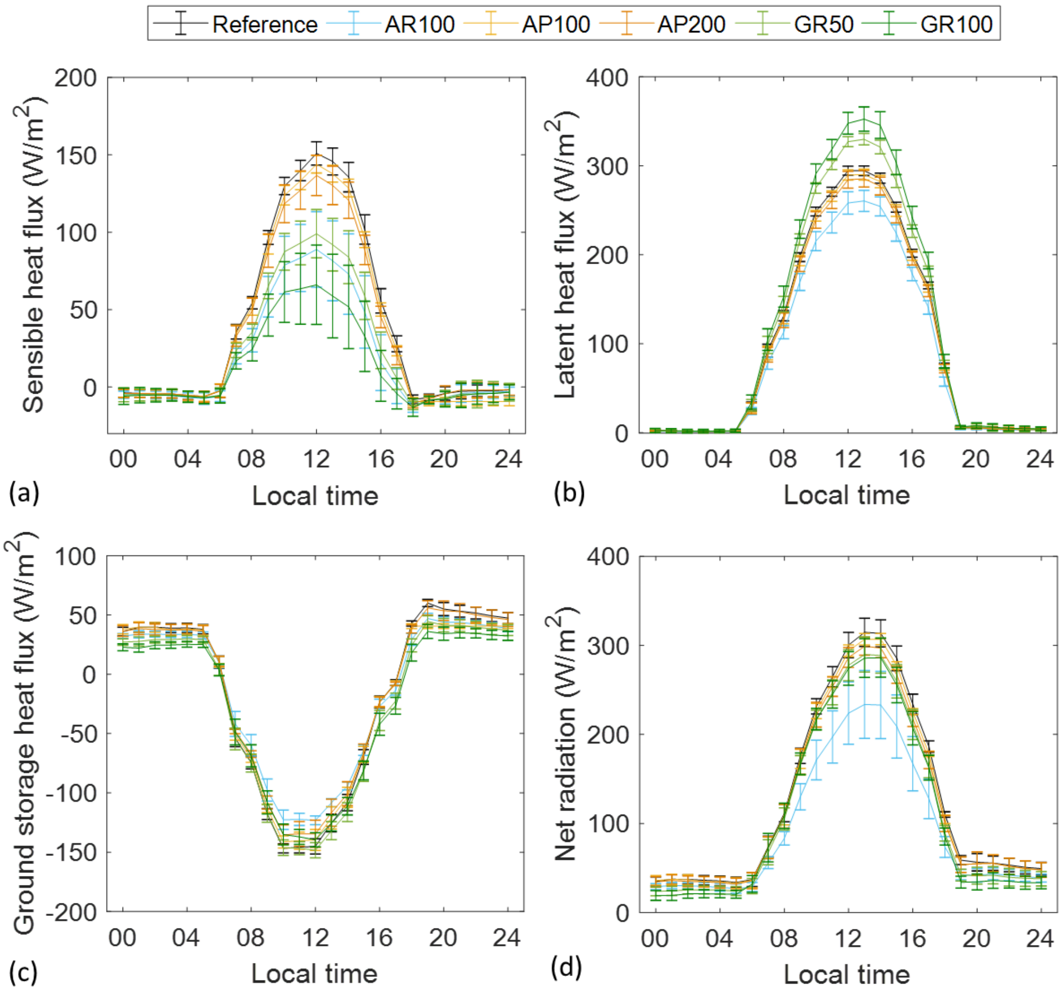

Figure B3. Impacts of five adaptation strategies on the surface energy balance at the peak day of the hottest heat wave in Washington D.C. for the period 2066–2070. (a) Sensible heat flux; (b) Latent heat flux; (c) Ground storage heat flux; (d) Net radiation. All results are averaged over urban grid cells in Domain 4. Error bars denote standard deviation over those grid cells. AP100 and AP200 are almost overlapped.

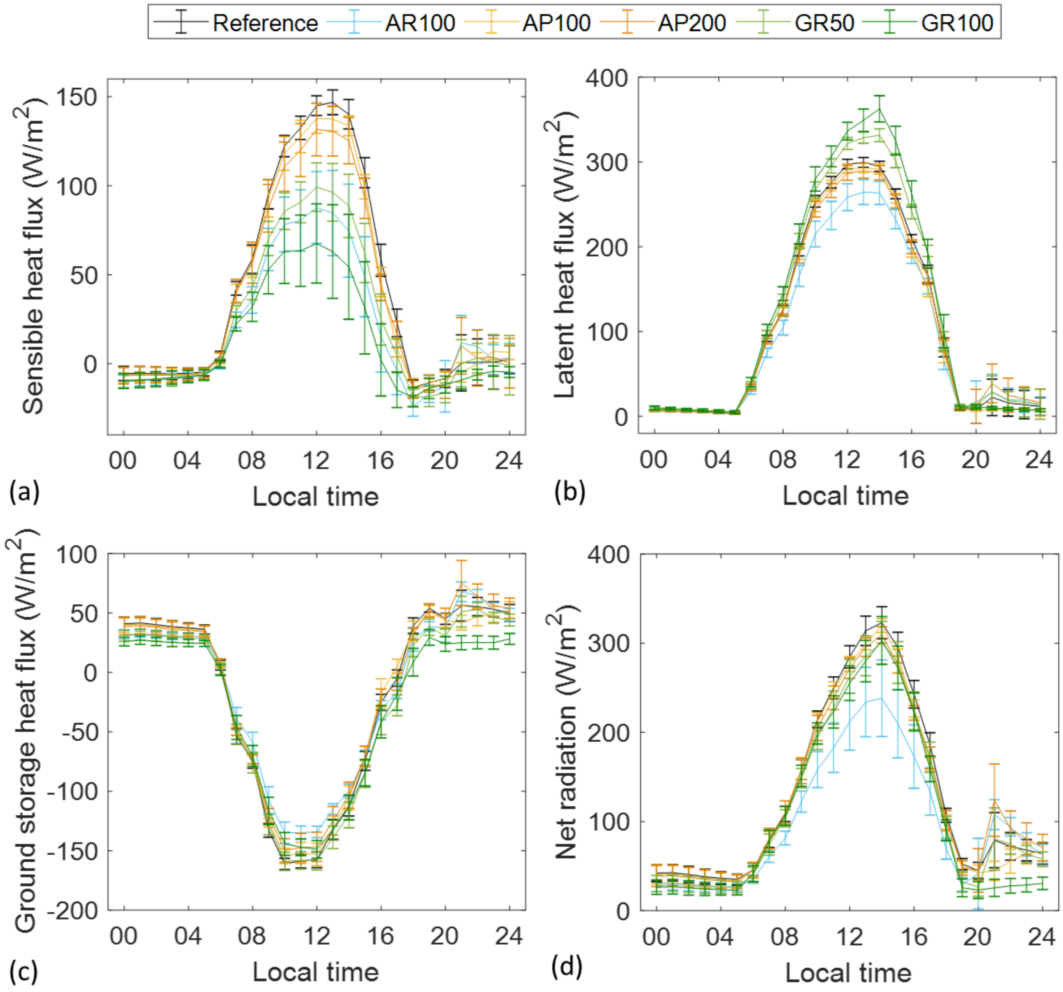

Figure B4. Impacts of five adaptation strategies on the surface energy balance at the peak day of the hottest heat wave in Washington D.C. for the period 2096–2100. (a) Sensible heat flux; (b) Latent heat flux; (c) Ground storage heat flux; (d) Net radiation. All results are averaged over urban grid cells in Domain 4. Error bars denote standard deviation over those grid cells. AP100 and AP200 are almost overlapped.

Useful links

To compile and run WRF under Linux:

http://www2.mmm.ucar.edu/wrf/OnLineTutorial/compilation_tutorial.php

To use UMD High Performance Computing (HPC):

http://www.glue.umd.edu/hpcc/

To upload or download files from HPC:

https://umd.service-now.com/itsupport/?id=kb_article&article=KB0010646

Appendix C: Electrical network analysis using swing equations

The electrical network of the Washington metro area is presented in Figure C1, with 18 supply nodes, 91 distribution nodes, and 131 branches. The branch and node data are presented in Table C1. The *K* values are updated for 150 times to generate the most robust grid. The *K* values of the branches connecting generators are greater than the others, because generators feed a large amount of power into the system. Tables C2-C5 summarize the change of failure probabilities in three future periods if the peak load increases by 7.5%, 5.625%, 3.75% or 2.5% per 1°C temperature rise.

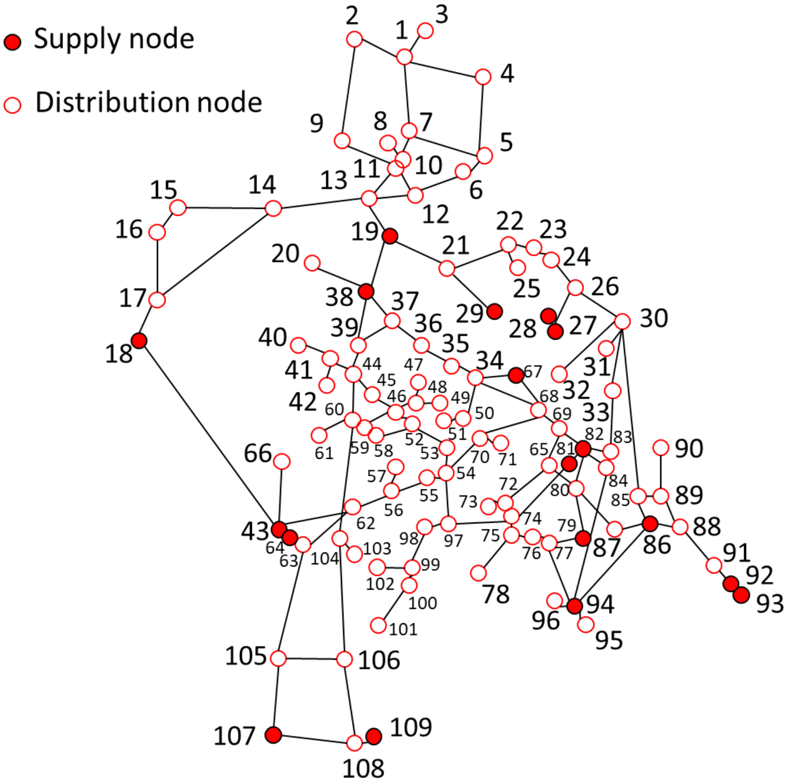

Figure C1. The electrical grid model for the Washington metro area.

Table C1. Brach and node data for the electrical model.

Branch Data				Node data	
Branch #	From bus *i*	To bus *j*	K_{ij} (Iteration =150, β=1)	Node #	P_i (s/^{2})
1	1	2	1.251161457	1	-1
2	1	3	1.920215664	2	-1
3	1	4	1.335750794	3	-1
4	1	7	2.479361991	4	-1
5	2	9	2.043778742	5	-1
6	4	5	2.378360154	6	-1
7	5	6	1.741753757	7	-1
8	5	7	1.279459345	8	-1
9	6	12	2.448229629	9	-1
10	7	10	1.302507304	10	-1
11	8	10	1.552319852	11	-1
12	9	11	3.193567894	12	-1
13	10	11	2.557265531	13	-1
14	11	12	1.648156333	14	-1
15	11	13	7.299859353	15	-1
16	12	13	5.326427341	16	-1
17	13	14	3.570722908	17	-1
18	13	19	17.1225779	18	4.75
19	14	15	3.814380593	19	4.25
20	14	17	5.035873396	20	-1
21	15	16	3.73700364	21	-1
22	16	17	2.961821997	22	-1
23	17	18	21.15434975	23	-1
24	18	43	1.6643502	24	-1
25	19	21	4.689206184	25	-1

26	19	38	4.095405134	26	-1
27	20	38	1.823825887	27	4.75
28	21	22	2.621377107	28	4.75
29	21	29	19.11593686	29	4.75
30	22	23	1.797765584	30	-1
31	22	25	2.10412974	31	-1
32	23	24	3.285174993	32	-1
33	24	26	6.61068404	33	-1
34	26	27	16.51953836	34	-1
35	26	28	16.51952391	35	-1
36	26	30	20.02873412	36	-1
37	30	31	2.282156184	37	-1
38	30	32	2.282156011	38	4.75
39	30	33	2.588046594	39	-1
40	30	85	2.431081502	40	-1
41	33	83	1.530747041	41	-1
42	34	35	1.282141019	42	-1
43	34	50	3.619133451	43	4.75
44	34	67	6.625482696	44	-1
45	34	68	2.386876067	45	-1
46	35	36	2.141577174	46	-1
47	36	37	3.5789979	47	-1
48	37	38	6.870673694	48	-1
49	37	39	1.304815613	49	-1
50	38	39	7.785480582	50	-1
51	39	44	5.740883416	51	-1
52	40	41	1.654918508	52	-1
53	41	42	1.654918927	53	-1
54	41	44	3.701611576	54	-1
55	43	62	9.863572604	55	-1

56	43	64	2.862250783	56	-1
57	43	66	2.778937259	57	-1
58	44	45	2.548701131	58	-1
59	44	60	2.51933249	59	-1
60	45	46	1.631558358	60	-1
61	46	48	2.542698108	61	-1
62	46	52	1.193424528	62	-1
63	46	59	2.971840499	63	-1
64	47	48	2.016100805	64	4.75
65	48	49	1.658653898	65	-1
66	50	51	1.999556459	66	-1
67	52	53	1.136688623	67	4.75
68	52	58	1.576229937	68	-1
69	53	54	1.8060747	69	-1
70	54	55	3.913005828	70	-1
71	54	70	2.698260824	71	-1
72	54	97	1.801833621	72	-1
73	55	56	6.580859193	73	-1
74	56	57	1.963396993	74	-1
75	56	62	20.39804003	75	-1
76	58	59	2.280835912	76	-1
77	59	60	3.097894052	77	-1
78	60	61	1.59112584	78	-1
79	60	104	14.20035599	79	4.75
80	62	63	5.730184514	80	-1
81	63	64	5.43550507	81	4.75
82	63	105	2.987423205	82	4.75
83	65	69	3.636807597	83	-1
84	65	72	3.504595002	84	-1
85	65	80	6.563564287	85	-1

86	67	68	3.378416415	86	4.75
87	68	69	4.862146658	87	-1
88	68	70	3.915023234	88	-1
89	69	82	8.790923249	89	-1
90	70	71	1.885478157	90	-1
91	72	73	2.016863315	91	-1
92	72	74	2.484387807	92	8
93	74	75	2.588198226	93	4.75
94	74	81	17.07718254	94	4.25
95	74	97	8.930329445	95	-1
96	75	76	3.615287583	96	-1
97	75	78	2.025844964	97	-1
98	76	77	6.753487756	98	-1
99	77	79	4.349263069	99	-1
100	77	94	3.321842363	100	-1
101	79	80	4.701164457	101	-1
102	80	82	1.630483263	102	-1
103	80	87	4.236243008	103	-1
104	81	82	1.29869036	104	-1
105	82	83	1.882349897	105	-1
106	82	84	1.313405873	106	-1
107	84	94	2.328928574	107	8
108	85	86	2.929115395	108	-1
109	85	89	1.300034086	109	4.75
110	86	87	3.980022642	Total	0
111	86	88	3.17667571		
112	86	94	2.334489153		
113	88	89	4.079838135		
114	88	91	10.27872541		
115	89	90	2.308897273		

116	91	92	22.10397291		
117	92	93	3.724208174		
118	94	95	2.188871935		
119	94	96	2.188871207		
120	97	98	8.300965004		
121	98	99	5.323635817		
122	99	100	2.372887858		
123	99	102	1.676956385		
124	100	101	1.615527782		
125	103	104	2.028294922		
126	104	106	20.05427524		
127	105	106	3.033358959		
128	105	107	21.17065141		
129	106	108	19.59080559		
130	107	108	4.737339573		
131	108	109	12.64186227		

Table C2. The failure probability of the electricity system ($\beta_{PKload} = 7.5\%$).

Analyzed period	Failure probability				Change ratio of failure probability			
	$P(F_G)$	$P(F_T)$	$P(F_S)$	$P(F_O)$	$\Delta p(F_G)$	$\Delta p(F_T)$	$\Delta p(F_S)$	$\Delta p(F_O)$
2011–2015	0.0130	0	0	0.0071	/	/	/	/
2036–2040	0.0370	0.0152	0.0065	0.4660	1.846	/	/	64.394
2066–2070	0.1109	0.0370	0.0196	0.5135	7.531	/	/	71.062
2096–2100	0.2761	0.1848	0.1326	0.5140	20.238	/	/	71.137

Table C3. The failure probability of the electricity system ($\beta_{PKload} = 5.625\%$).

Analyzed period	Failure probability				Change ratio of failure probability			
	$P(F_G)$	$P(F_T)$	$P(F_S)$	$P(F_O)$	$\Delta p(F_G)$	$\Delta p(F_T)$	$\Delta p(F_S)$	$\Delta p(F_O)$
2011–2015	0.0130	0	0	0.0071	/	/	/	/
2036–2040	0.0282	0	0	0.0297	0.838	/	/	3.170
2066–2070	0.0652	0.0043	0	0.2892	4.015	/	/	39.591
2096–2100	0.2326	0.0848	0.0587	0.5140	16.892	/	/	71.137

Table C4. The failure probability of the electricity system ($\beta_{PKload} = 3.75\%$).

Analyzed period	Failure probability				Change ratio of failure probability			
	$P(F_G)$	$P(F_T)$	$P(F_S)$	$P(F_O)$	$\Delta p(F_G)$	$\Delta p(F_T)$	$\Delta p(F_S)$	$\Delta p(F_O)$
2011–2015	0.0130	0	0	0.0071	/	/	/	/
2036–2040	0.0239	0	0	0.0221	1.169	/	/	2.099
2066–2070	0.0434	0	0	0.0624	2.338	/	/	7.758
2096–2100	0.1891	0.0087	0	0.4769	13.546	/	/	65.932

Table C5. The failure probability of the electricity system ($\beta_{PKload} = 1.875\%$).

Analyzed period	Failure probability				Change ratio of failure probability			
	$P(F_G)$	$P(F_T)$	$P(F_S)$	$P(F_O)$	$\Delta p(F_G)$	$\Delta p(F_T)$	$\Delta p(F_S)$	$\Delta p(F_O)$
2011–2015	0.0130	0	0	0.0071	/	/	/	/
2036–2040	0.0022	0	0	0.0002	-4.909	/	/	-0.969
2066–2070	0.0043	0	0	0.0008	-2.023	/	/	-0.883
2096–2100	0.0804	0	0	0.1604	5.185	/	/	21.514

Table C6. The failure probability of the electricity system ($\beta_{PKload} = 0$)

Analyzed period	Failure probability				Change ratio of failure probability			
	$P(F_G)$	$P(F_T)$	$P(F_S)$	$P(F_O)$	$\Delta p(F_G)$	$\Delta p(F_T)$	$\Delta p(F_S)$	$\Delta p(F_O)$
2011–2015	0.0130	0	0	0.0071	/	/	/	/
2036–2040	0	0	0	0	-1	/	/	-1
2066–2070	0	0	0	0	-1	/	/	-1
2096–2100	0	0	0	0	-1	/	/	-1

Appendix D: Cost-benefit analysis for rooftop photovoltaics

Table D1 shows the calculation process for upper and lower boundaries of annual electricity production value by photovoltaic (PV) panels. Table D2 presents the declined values of cascading failure probability (ΔP_c) when adaptation strategies are employed. Table D3 calculates the monetized benefits in preventing the disruption of electricity service due to adaptations. Table D4 summarizes greenhouse gases' emission factors per MWh electricity production. The data are obtained from EPA (2018). Table D5 lists social cost per metric ton of CO_2, CH_4, and N_2O with an annual discount rate of 5%, 3% and 2.5% from 2015 to 2050 suggested by EPA (2019). The social cost later than 2050 is computed by extrapolation. Table D6 lists mean (μ) and standard deviation (σ) of cost and benefit distributions for inthe stallation year 2015. Table D7 and Table D8 present life-cycle benefit and cost results of installing rooftop PV in 2040 and 2070 respectively at the Washington metro area.

Table D1. Values of annual electricity production by photovoltaic (PV) panels (2015 dollars).

Unit price ($/kWh)	Strategy	Annual productivity (kW)	Lower cost boundary	Upper cost boundary
0.125	PV25	3605000	$522,725,000	
	PV50	7210000	$1,045,450,000	
	PV75	10815000	$1,568,175,000	
	PV25	3605000		
	PV50	7210000		
	PV75	10815000		
0.132	PV25	3605000		
	PV50	7210000		
	PV75	10815000		
	PV25	3605000		$611,004,240
	PV50	7210000		$1,222,008,480
	PV75	10815000		$1,833,012,720

Table D2. Reduction in power outage probability (ΔP_O) when adaptation strategies are employed.

Period	Strategy		
	PV25	PV50	PV75
2036–2040	0.0106	0.0123	0.0124
2066–2070	0.0430	0.0549	0.0553
2096–2100	0.1061	0.1814	0.2040

Table D3. Benefits in preventing the disruption of electricity service in 2015 dollars.

Disruption cost (C_d)	Period	PV25		PV50/PV75	
		ΔP_O	$\Delta P_O \cdot C_d$	ΔP_O	$\Delta P_O \cdot C_d$
\$34,339,071 (lower boundary)	2036–2040	0.4660	16,002,007	0.4660	16,002,007
	2066–2070	0.5127	17,605,642	0.5135	17,633,113
	2096–2100	0.0371	1,273,980	0.5140	17,650,282
\$140,914,388 (higher boundary)	2036–2040	0.4660	65,666,105	0.4660	65,666,105
	2066–2070	0.5127	72,246,807	0.5135	72,359,538
	2096–2100	0.0371	5,227,924	0.5140	72,429,995

Note: ΔP_O is the reduction of power outage probability. C_d is the cost of power supply disruption.

Table D4. Greenhouse gases' emission factors per MWh electricity production (EPA 2018).

eGRID subregion	CO_2 factor		CH_4 factor		N_2O factor	
	lb/MWh	kg/MWh	lb/MWh	g/MWh	lb/MWh	g/MWh
RFCE (RFC East)	758.2	343.9134544	0.05	22.6796	0.009	4.082328

Table D5. Social cost per metric ton of CO_2, CH_4, and N_2O with an annual discount rate of 5%, 3% and 2.5% in 2017 dollars (EPA 2019).

Year	CO_2 (\$/ton)			CH_4 (\$/ton)			N_2O (\$/ton)		
	5%	3%	2.5%	5%	3%	2.5%	5%	3%	2.5%
2015	11	36	56	450	1,000	1,400	4,000	13,000	20,000
2020	12	42	62	540	1,200	1,600	4,700	15,000	22,000
2025	14	46	68	650	1,400	1,800	5,500	17,000	24,000
2030	16	50	73	760	1,600	2,000	6,300	19,000	27,000
2035	18	55	78	900	1,800	2,300	7,400	21,000	29,000
2040	21	60	84	1,000	2,000	2,600	8,400	23,000	32,000
2045	23	64	89	1,200	2,300	2,800	9,500	25,000	34,000
2050	26	69	95	1,300	2,500	3,100	11,000	27,000	37,000
2055	28	74	101	1,421	2,714	3,343	12,000	29,000	39,429
2060	30	78	106	1,543	2,929	3,586	13,000	31,000	41,857
2065	32	83	112	1,664	3,143	3,829	14,000	33,000	44,286
2070	35	88	117	1,786	3,357	4,071	15,000	35,000	46,714
2075	37	93	123	1,907	3,571	4,314	16,000	37,000	49,143
2080	39	97	128	2,029	3,786	4,557	17,000	39,000	51,571
2085	41	102	134	2,150	4,000	4,800	18,000	41,000	54,000
2090	43	107	140	2,271	4,214	5,043	19,000	43,000	56,429
2095	45	111	145	2,393	4,429	5,286	20,000	45,000	58,857
2100	47	116	151	2,514	4,643	5,529	21,000	47,000	61,286

Note: The values in blue are calculated by linear extrapolation. The costs for years between are interpolated from two nearby time points.

Table D6. Mean (μ) and standard deviation (σ) of cost and benefit distributions.

Strategy	Cost (2015 million dollars)		Direct benefit (2015 million dollars)		Direct and indirect benefit (2015 million dollars)	
	μ_C	σ_C	$\mu_{B,direct}$	$\sigma_{B,direct}$	μ_B	σ_B
PV25	16,147	1,471	11,074	362	32,521	725
PV50	32,102	2,902	21,747	643	64,641	1,368
PV75	48,249	4,372	32,419	924	96,760	2,012

Table D7. Life-cycle benefits and costs of rooftop photovoltaics (PV) in the Washington metro area, $t_0 = 2040$, $n = 30$ years, $r = 3\%$.

Strategy	Cost (2015 million dollars)	Direct benefit (2015 million dollars)	Direct and indirect benefit (2015 million dollars)
PV25	8,392 – 13,220	4,841 – 5,984	29,348 – 33,110
PV50	16,747 – 26,291	9,608– 11,665	58,621– 65,918
PV75	25,139 – 39,511	14,351 – 17,249	87,871– 98,628

Table D8. Life-cycle benefits and costs of rooftop photovoltaics (PV) in the Washington metro area, $t_0 = 2070$, $n = 30$ years, $r = 3\%$.

Strategy	Cost (2015 million dollars)	Direct benefit (2015 million dollars)	Direct and indirect benefit (2015 million dollars)
PV25	5,027 – 7,347	1,991 – 2,452	27,566 – 30,760
PV50	10,038 – 14,633	3,967 – 4,843	55,116 – 61,460
PV75	15,065 – 21,980	5,916 – 7,121	82,640 – 92,046

Due to temperature change, the three PV strategies may not cause peak electricity load on the power grid to decrease by 25%, 50%, and 75%. Table D10 shows the variation of reduction in analyzed periods.

Table D9. Percent reduction of peak electricity load on the power grid contributed by three PV strategies.

Period	Mean temperature (°C)	Peak electricity load (GW)	Strategy		
			PV25	PV50	PV75
2011–2015	36.59252	13.75928	-26.20%	-52.40%	-78.60%
2036–2040	39.29375	15.23105	-23.67%	-47.34%	-71.01%
2066–2070	40.86149	16.15549	-22.31%	-44.63%	-66.94%
2096–2100	43.24278	17.65836	-20.42%	-40.83%	-61.25%

Table D10. The growth of peak electricity loads relative to 2011–2015 and increased generation capacity contributed by three PV strategies.

Period	Peak electricity load growth (GW)	Strategy		
		PV25 (GW)	PV50 (GW)	PV75 (GW)
2036–2040	1.4718	3.605	7.21	10.815
2066–2070	2.3962	3.605	7.21	10.815
2096–2100	3.8991	3.605	7.21	10.815

Appendix E: Cost-benefit analysis for green roofs, cool roofs, and reflective pavements

The costs and benefits of green roofs, cool roofs, and reflective pavements have been estimated by a number of studies for different building types, geographical regions, and climate conditions, as shown in Tables E1-E6. Table E1 lists the benefit-to-cost ratios of cool roofs, green roofs, and reflective pavements estimated by Kats and Grassbrook (2016) for Washington D.C. The benefits they considered include energy savings, improved air quality, and public health, reduced stormwater runoff, climate change mitigation, and increased resilience and employment. Their estimated benefit-cost ratios are 7.3, 2.0 and 2.6 for cool roofs with an albedo of 0.65–0.75, green roofs with a growing media depth of 0.1 m and a leaf area index of 2, and reflective pavements with an albedo of 0.3–0.45 respectively.

Table E1. Cost effectiveness of cool roof, green roof, and reflective pavement strategies in Washington D.C. from 2017–2056 (Kats and Grassbrook 2016).

Technology	Benefit-to-cost ratio	Total cost	Total benefit
Cool roofs	7.3	$32,318,000	$236,960,000
Green roofs	2.0	$282,957,000	$563,636,000
Reflective pavements	2.6	$43,802,000	$112,377,000

Washington DC's 61 square miles (158 km^2) of surface is comprised of 15.9% roofs and 24.1% paved area. The data of Kats and Glassbrook (2016) are used in this research to assess five mitigation strategies for Washington D.C. The analysis period is 40 years from 2017–2056, where the paintings/coatings of cool roofs and reflective pavements are replaced after 20 years of use. The cost data derived from Kats and Glassbrook (2016) are converted to unit cost of each strategy (\$/m^2), as shown in Table E2.

Direct energy savings refer to decreased energy consumptions in buildings due to the installation of cool roofs and green roofs. Cool roofs reflect sunlight and reduce heat uptake of roof surface, which can decrease cooling energy demands in summer but increase heating energy needs in winter. Green roofs help to save energy in summer and winter, as the growing media and vegetation can absorb and store a large amount of heat. This can decrease temperature fluctuation in buildings and reduce the effect of extreme outdoor temperatures. For green roofs, the data obtained from Kats and Glassbrook (2016) are used directly. For cool roofs, the data are scaled based on the ratio of increased albedo relative to conventional ones. In the study of Kats and Glassbrook (2016), the albedo of cool roofs is 0.45 greater than that of conventional ones. Therefore, the result of Kats and Glassbrook (2016) times 0.3/0.45 yield the direct energy savings of the cool roof strategy (AR100).

Indirect energy savings are created by UHI mitigation, as weakening the UHI effect can reduce summer energy consumption; however, this can lead to increased winter energy usage. For cool roof strategy (AR100), the data of Kats and Glassbrook (2016) are scaled by the ratio of increased albedo (0.3/0.45). For reflective pavements and green roofs, the result of AR100 is rescaled by the ratio of temperature reductions to yield indirect energy savings of the four strategies. The ratios of AP100, AP200, GR50, and GR100 are 0.05/0.7, 0.1/0.7, 0.6/0.7, and 1.1/0.7, respectively.

The increase in temperature can raise ground-level ozone contents, which can impair human health. The health impact of ozone estimated by Kats and Glassbrook (2016) is scaled by the ratio of temperature reductions to yield the benefits of the five strategies on health. In addition, increased electricity production during hot days discharges a greater amount of PM2.5 into the atmosphere, which further exacerbates health problems. The health impact of PM2.5 estimated by Kats and Glassbrook (2016) is scaled by the ratio of direct and indirect energy savings to yield the benefits of the five strategies on health.

Heat-related mortality can be affected by the magnitude of temperature and humidity, the duration of high temperatures, and the time of the season (Kalkstein et al. 2013). For cool roof strategy (AR100), the data of Kats and Glassbrook (2016) are scaled by the ratio of increased albedo (0.3/0.45). For reflective pavements and green roofs, the result of AR100 is rescaled by the ratio of temperature reductions to yield the benefits of the four strategies in reducing mortality risk.

Climate change mitigation involves reducing greenhouse gas emissions and reducing solar radiation. The GHG emissions (i.e., CO_2, CH_4, N_2O) are related to electricity production and natural gas combustion for building cooling and heating purposes. The impacts of GHG emissions on the economy is typically measured by the social cost of carbon. The social cost of carbon estimated by Kats and Glassbrook (2016) is scaled by the ratio of direct and indirect energy savings to yield the benefits of the five strategies in reducing GHG emissions.

Elevating albedo can reduce solar radiation. Akbari et al. (2009) indicated that elevating roof albedo by 0.25 is equivalent to reducing CO_2 by 64 kg/m^2, and elevating pavement albedo by 0.15 is equivalent to reducing CO_2 by 38 kg/m^2. Menon et al. (2010) estimated a greater annual CO_2 reduction of 82 kg/m^2 and 49 kg/m^2 as roof and pavement albedos increase 0.25 and 0.15, respectively. The results of the two studies are averaged and used in this study, which yields 73kg/m^2 of CO_2 reduction per 0.25 increase in roof albedo, and 43.5 kg/m^2 of CO_2 reduction per 0.15 increase in pavement albedo. Annual CO_2 sequestration of extensive green roofs is about 2.5 kg per m^2 of roof (Kuronuma et al. 2018), which is very small and can be neglected. The social cost of carbon estimated by Kats and Glassbrook (2016) is scaled by the ratio of increased albedos to yield the benefits of the five strategies in reducing solar radiation.

The data for stormwater reduction and job creation obtained from Kats and Glassbrook (2016) are used directly. All benefit values computed above are converted to unit benefit (\$/m^2) for a comparison.

Table E2. Annual costs and benefits of five mitigation strategies (m^2) in Washington DC, 2015 dollars.

Items	Strategies				
	AR100	AP100	AP200	GR50	GR100
Analysis period	2017 – 2056	2017 – 2056	2017 – 2056	2017 – 2056	2017 – 2056
Lifespan	20 years	20 years	20 years	40 years	40 years
Annual discount rate	3%	3%	3%	3%	3%
Total costs	$2.6	$2.3	$2.3	$112.6	$112.6
First cost	$1.9	$1.2	$1.2	$77.5	$77.5
Operation and maintenance	0	0	0	$35.1	$35.1
Additional replacement	$0.7	$3.1	$6.3	0	0
Employment rating	0	0	0	$0.1	$0.1
Total benefits	$16.6	$4.7	$9.4	$215.5	$222.5
Energy	$1.6	$0.03	$0.1	$8.2	$8.5
Direct energy savings	$1.2	0	0	$7.8	$7.8
Indirect energy savings (Urban Heat Island mitigation)	$0.4	$0.03	$0.1	$0.4	$0.7

Table E2. Annual costs and benefits of five mitigation strategies (m^2) in Washington DC, 2015 dollars (Continued).

Items	Strategies				
	AR100	AP100	AP200	GR50	GR100
Stormwater	0	0	0	$190.6	$190.6
Fee discounts	0	0	0	$2.1	$2.1
Stormwater retention credits	0	0	0	$188.5	$188.5
Health	$9.5	$0.7	$1.3	$10.0	$16.6
Ozone	$7.5	$0.5	$1.1	$6.5	$11.9
PM2.5	$0.5	$0.02	$0.03	$2.3	$2.5
PM2.5 (direct energy saving)	$0.3	0	0	$2.1	$2.1
PM2.5 (indirect energy saving)	$0.2	$0.02	$0.03	$0.2	$0.4
Heat-related mortality	$1.5	$0.1	$0.2	$1.2	$2.3
Climate change	$5.4	$4.0	$8.0	$1.7	$1.8
Greenhouse gas (GHG) emissions	$0.5	$0.009	$0.02	$2.5	$2.6

Table E2. Annual costs and benefits of five mitigation strategies (m^2) in Washington DC, 2015 dollars (Continued).

Items	Strategies				
	AR100	AP100	AP200	GR50	GR100
GHG emissions (direct energy saving)	$0.4	0	0	$2.4	$2.4
GHG emissions (indirect energy saving)	$0.1	$0.009	$0.02	$0.1	$0.2
Global cooling	$4.9	$2.4	$4.9	-$0.8	-$0.8
Employment	0	0	0	$5.0	$5.0
Employee pay	0	0	0	$4.0	$4.0
Welfare payments	0	0	0	0	0
Tax revenue	0	0	0	$1.0	$1.0
Federal taxes	0	0	0	$0.9	$0.9
State/City taxes	0	0	0	$0.1	$0.1
Net benefit	$14.0	$0.8	$4.0	$102.8	$109.8
Benefit-cost-ratio	6.4	1.4	2.7	1.9	2.0

Table E3. Costs and benefits of extensive green roofs.

Study	Place	Building type	Lifespan (year)	Cost			Benefit		
				Incremental initial cost (\$/m^2)	Incremental energy consumption (kWh/m^2)	Incremental carbon emission (\$/m^2)	Annual energy saving[a] (kWh/m^2)	Annual stormwater runoff reduction (\$/m^2)	Annual carbon reduction[b] (\$/m^2)
Blackhurst et al. (2010)	Typical cities, USA	Single-family residential	30	87.5	0.40	3.17	1.05 (C)	50%	0.14 (D, I)
		Multi-family residential	30	150.7	0.64	4.78	2.83 (C)	50%	0.47 (D, I)
		Commercial	30	193.7	0.81	6.28	6.28 (C)	50%	0.61 (D, I)
Niu et al. (2010)	Washington, DC, USA	Commercial, 1795 m^2 roof areas	40	306±44.56	N/A	N/A	2.6 (C) 0.9 (H)	35% or 50%	0.049 (I) *Including CO_2, and NO_x*
		Residential, 55 m^2 roof areas	40				3.6 (C) 5.5 (H)		
		Residential, 125 m^2 roof areas	40				3.2 (C) 4.8 (H)		
		Residential, 270 m^2 roof areas	40				2.6 (C) 4.4 (H)		

Note: [a] The 'C' indicates cooling energy that is provided by electricity, and 'H' means heating energy that is relied on natural gas.

[b] The 'D' indicates direct carbon reduction caused by vegetation's absorption, and 'I' means indirect carbon reduction due to energy saving and urban heat island mitigation.

N/A=Not available.

Table E4. Costs and benefits of extensive green roofs (continued).

Study	Place	Building type	Lifespan (year)	Cost			Benefit		
				Incremental initial cost (\$/m^2)	Incremental energy consumption (kWh/m^2)	Incremental carbon emission (\$/m^2)	Annual energy saving[a] (kWh/m^2)	Annual stormwater runoff reduction(\$/m^2)	Annual carbon reduction[b] (\$/m^2)
Carter and Keeler (2008)	Athens, GA, USA	One-story, 929 m^2 roof areas	40	71.63	N/A	N/A	\$0.37/m^2	0.04	0.11 (D)
Kats and Grassbrook (2016)	Washington, DC, USA	Any	40	100–150 plus 3.1–4.6 *Annual maintenance*	N/A	N/A	\$0.171–0.198/m^2	0.041	0.051–0.067
Berardi (2016)	Toronto, Canada	School	N/A	105–120	N/A	N/A	5.8–9.6 (C, H)	N/A	N/A
Bianchini and Hewage (2012)	Any cities	Any	40	130–165 plus 0.7–13.5 *Annual maintenance*	N/A	14.06–22.20 *Including* CO_2 *and* NO_x	\$0.18–0.68/m^2 (C) \$0.22/m^2 (H)	0–0.38	0.025–0.03 (D) *Including* CO_2 *and* NO_x

Note: [a]The ‘C’ indicates cooling energy that is provided by electricity, and ‘H’ means heating energy that is relied on natural gas.

[b]The ‘D’ indicates direct carbon reduction caused by vegetation’s absorption, and ‘I’ means indirect carbon reduction due to energy saving and urban heat island mitigation.

N/A=Not available.

Table E5. Costs and benefits of cool roofs.

Study	Place	Building type	Lifespan (year)	Solar reflectance/ Albedo	Cost	Benefit	
					Incremental initial cost (\$/m^2)	Annual energy saving[a] (kWh/m^2)	Annual GHG emission reduction (kg/m^2)
Akbari et al. (2005)	California, USA	Retail store	N/A	0.80	N/A	0.6–16.4 (C)	N/A
		School	N/A	0.65–0.79	N/A	1.1–6.5 (C, H)	N/A
		Cold storage facility	N/A	0.63–0.70	N/A	4.5–7.4 (C)	N/A
Akbari (2003)	Nevada, USA	Regeneration building (communication), 14.9 m^2 roof areas	N/A	0.72–0.80	0	6.7–8.4 (C)	N/A
Kats and Grassbrook (2016)	Washington, DC, USA	Any	40	0.25–0.65 *Steep–low slope*	1.5–5.5 *Steep–low slope* plus 0 *Annual maintenance*	\$0.009–0.163/m^2 *Steep–low slope*	\$0.017–0.084/m^2 *Steep–low slope*
Xu et al. (2012)	Hyderabad, India	Commercial, 700 m^2 roof areas	N/A	0.7	N/A	20–22 (C), black roof 13–14 (C), concrete roof	11–12, concrete roof
Romeo and Zinzi (2013)	Sicily, Italy	School, 700 m^2 roof areas	N/A	0.82	N/A	4.6% (C, H), actual building 2.2% (C, H), insulated roof 13.0% (C, H), insulated building	N/A

Note: [a] The ‘C’ indicates cooling energy that is provided by electricity, and ‘H’ means heating energy that is relied on natural gas.
N/A=Not available.

Table E6. Costs and benefits of reflective pavement.

Study	Place	Type	Lifespan (year)	Cost		Benefit	
				Initial cost ($\$/m^2$)	Replacement cost ($\$/m^2$)	Annual energy saving (kWh/m^2)	Annual GHG emission reduction (kg/m^2)
Kats and Grassbrook (2016)	Washington, DC, USA	Road	40	0.02	0.33–0.38	0.06	0.19
		Parking lot	40	0.46	0.50	0.06	0.19
		Concrete sidewalk	40	0.24	0	0.03	0.09
		Brick sidewalk	40	0.52	0	0.03	0.10

Notations

B	\$	Benefit of a strategy
B_{direct}	\$	Direct benefit of a strategy
C	\$	Cost of a strategy
C_C	NA	Climate change scenario
C_S	NA	Climate stressor
C_{h2}	$W/(m^2K)$	Heat transfer coefficient at 2 meters above the surface
C_{ij}	NA	Capacity of the line *i*-*j*
F	NA	System failure
F_{ij}	s^{-2}	Power flow along the line *i*-*j*
G	NA	Generation units
H_G	W/m^2	Ground/ storage heat flux
H_L	W/m^2	Latent heat flux
H_S	W/m^2	Sensible heat flux
K_{ij}	s^{-2}	Coupling strength of two connected nodes *i* and *j*
L	\$	Net present value of loss caused by climate change
N	NA	Number of branches in an electrical network
NPV	\$	Mean net present value
O	NA	Power outage
P_i	s^{-2}	Unit quantity of power generated or consumed at the node *i*

$P(C)$	NA	Probability that a climate-change scenario occurs
$P(F_a)$	NA	Failure probability in each component of the power system, where $a = G, T\ or\ S$
$P(F_C)$	NA	Cascading failure probability
$P(F_O)$	NA	Power outage probability
$P(F\|S)$	NA	Probability of system failure when the stressor intensifies
$P(L\|F)$	NA	Probability of a loss when the system fails
$P(S\|C)$	NA	Probability that a stressor intensifies when climate changes
$P(B > C)$	NA	Probability that benefits surpass costs
$P(B_{direct} > C)$	NA	Probability that direct benefits surpass costs
PRM_i	%	Initial planning reserve margin
PRM_{crit}	%	PRM critical value for potential service interruption
R_n	W/m^2	Net radiation/ radiative flux
S	NA	Substation transformers
T	NA	Transmission lines
T_2	K	Air temperature at 2 meters above the surface
T_{mean}	°C	Mean summer daily maximum temperature
T_T	°C	Summer daily maximum temperature that causes conductor failure

T_S	°C	Summer daily maximum temperature that causes transformer failure
T_s	K	Skin surface temperature
T_{PRM}	°C	Summer daily maximum temperature at which the PRM is involved in a day
$T_{PRMcrit}$	°C	Summer daily maximum temperature at which the PRM reaches its critical value on a day
U_2	m/s	Wind speed at 2 meters above the surface
m	NA	Sum of the number of generators, transmission lines, and substations in the electrical grid
n	year	Number of years that is accounted for risk estimation
r	%	Annual discount rate
t_0	NA	Starting time point for risk estimation
t_{max}	s	Duration of cascading simulation for an electrical network
$\Delta p(F_a)$	NA	Change ratio of the failure probability in each component of the power system, where $a = G, T or\ S$
ΔR	%	Coefficient of risk reduction due to climate adaptation
Δf	Hz	Range of frequency deviation that ensures stable operation of a system

α	NA	Probability that two or more simultaneous component outages lead to power outages
β	NA	Tolerance parameter for detecting overcurrent lines
β_{GC}	NA	Loss of generation capacity of power plants per 1°C temperature increase
β_{TC}	NA	Loss of transmission capacity of power lines per 1°C temperature increase
β_{TDE}	NA	Loss of transmission efficiency of power lines per 1°C temperature increase
β_{SC}	NA	Loss of substation capacity per 1°C temperature increase
β_{G}	NA	Loss of peak generation capacity per 1°C temperature increase
β_{T}	NA	Loss of peak transmission capacity per 1°C temperature increase
β_{S}	NA	Loss of peak substation capacity per 1°C temperature increase
β_{PK}	NA	Increase of peak cooling load per 1°C temperature increase
θ	rad	Voltage phase angle
θ^*	rad	Fixed voltage phase angle at the stable state
ω	rad/s	Angular velocity

ω^*	rad/s	Fixed angular velocity at the stable state
ρ	rad^{-1}s^{-1}	Damping constant
ρ_a	kg/m^3	Air density
γ	NA	Benefit-cost ratio
μ	NA	Mean value
σ	NA	Standard deviation

Bibliography

Akbari, H. (2003). “Measured energy savings from the application of reflective roofs in two small non-residential buildings.” *Energy*, 28 (9), 953–967.

Akbari, H., and Konopacki, S. (2005). “Calculating energy-saving potentials of heat island reduction strategies.” *Energy Policy*, 33(6), 721–756.

Akbari, H., Levinson, R., and Rainer, L. (2005). “Monitoring the energy-use effects of cool roofs on California commercial buildings.” *Energy and Buildings*, 37 (10), 1007–1016.

Allen, A. R., Fernandez, S. J., Fu, J. S., and Olama, M. M. (2016). “Impacts of climate change on sub-regional electricity demand and distribution in the southern United States.” *Nature Energy*, 1, 160103.

Anderson, G. B. and Bell, M. L. (2011). “Heat Waves in the United States: Mortality Risk during Heat Waves and Effect Modification by Heat Wave Characteristics in 43 U.S. Communities.” *Environ. Health Perspect.*, 119(2), 210–218.

ASCE Committee on Adaptation to a Changing Climate. (2015). Review of Climate Science for Engineering Practice. In Adapting Infrastructure and Civil Engineering Practice to a Changing Climate. American Society of Civil Engineers, Reston, VA.

Ayyub, B. M. (2001). Elicitation of Expert Opinions for Uncertainty and Risks. CRC Press, Taylor & Francis Group, Boca Raton, FL.

Ayyub, B. M. (2014). Risk Treatment and Control Methods. In *Risk Analysis in Engineering and Economics*, *Second Edition* (pp. 450–455). CRC Press, Taylor & Francis Group, Boca Raton, FL.

Ayyub, B. M., Medina, M., Vinson, T., Walker, D., Wright, R. N., AghaKouchak, A., Barros, A. P., Cerino, A. C., Conray, R. P., Fields, R. E., Francis, O. P., Olsen, J. R., Samaras, C., and Vahedifard, F. (2018). *Climate-Resilient Infrastructure: Adaptive Design and Risk Management*. ASCE Manual of Practice 140, American Society of Civil Engineers, Reston, VA.

Baniassadi, A., Sailor, D. J., Crank, P. J., Ban-Weiss, G. A. (2018). “Direct and indirect effects of high-albedo roofs on energy consumption and thermal comfort of residential buildings.” *Energy and Buildings*, 178, 71–83.

Barsugli, J. J., Guentchev, G., Horton, R. M., Wood, A., Mearns, L. O., Liang, X. Z., Winkler, J., Dixon, K., Hayhoe, K., Rood, R., Goddard, L., Ray, A., Buja, L., and Ammann, C. (2013). “The Practitioner’s Dilemma: How to Assess the Credibility of Downscaled Climate Projections.” Eos Trans. Am. Geophys. Union, 94 (46), 424–425.

Bartos, M., and Chester, M. V. (2015). “Impacts of climate change on electric power supply in the Western United States.” *Nature Climate Change*, 5, 748–752.

Bartos, M., Chester, M., Johnson, N., Gorman, B., Eisenberg, D., Linkov, I. and Bates, M. (2016). “Impacts of rising air temperatures on electric transmission ampacity and peak electricity load in the United States.” *Environ. Res. Lett.*, 11, 114008.

Basara, J. B., Basara, H. G., Illston, B.G., and Crawford, K. C. (2010). “The impact of the urban heat island during an intense heat wave in Oklahoma City.” *Adv. Meteor.*, 2010, 230365.

Berardi, U. (2016). “The outdoor microclimate benefits and energy saving resulting from green roofs retrofits.” *Energy and Buildings*, 121, 217–229.

Bhandari, K. P., Collier, J. M., Ellingson, R. J., and Apul, D. S. (2015). “Energy payback time (EPBT) and energy return on energy invested (EROI) of solar photovoltaic systems: A systematic review and meta-analysis.” *Renewable and Sustainable Energy Reviews*, 47, 133-141.

Bianchini, F., and Hewage, K. (2012). “Probabilistic social cost-benefit analysis for green roofs: A lifecycle approach.” *Building and Environment*, 58, 152–162.

Blackhurst, M., Hendrickson, C., and Matthews, H. S. (2010). “Cost-Effectiveness of Green Roofs.” *J. Archit. Eng*., 16(4), 136–143.

BLS. (U.S. Bureau of Labor Statistics). (2019). *Average Energy Prices - Washington DC.* <https://www.bls.gov/regions/mid-atlantic/data/averageenergyprices_washingtondc_table.htm> (April 2, 2019).

BLUEFIN. (2013). *Washington D.C. Smart Roof Program*. < http://resources.cleanenergyroadmap.com/BENV_M_bluefin_smart_roofs_overview.pdf > (Jan. 5, 2019).

Bollinger, L. A., Bogmans, C. W. J., Chappin, E. J. L., Dijkema, G. P. J., Huibregtse, J. N., Maas, N., Schenk, T., Snelder, M., van Thienen, P., de Wit, S., Wols, B., Tavasszy, L. A. (2014). “Climate adaptation of interconnected infrastructures: a framework for supporting governance.” *Reg Environ Change*, 14(3), 919 – 931.

Burillo, D., Chester, M., and Ruddell, B. (2016). “Electric grid vulnerabilities to rising air temperatures in Arizona.” *Procedia Engineering*, 145, 1346 – 1353.

Carter, T. R., Parry, M. L., Harasawa, H., and Nishioka, S. (1994). *IPCC Technical Guidelines for Assessing Climate Change Impacts and Adaptations.* Report, Department of Geography, University College London, UK and the Center for Global Environmental Research, National Institute for Environmental Studies, Japan. < https://www.ipcc.ch/report/ipcc-technical-guidelines-for-assessing-climate-change-impacts-and-adaptations-2/> (April 5, 2019).

Carter, T., and Keeler, A. (2008). “Life-cycle cost–benefit analysis of extensive vegetated roof systems.” *J. Environmental Management*, 87 (3), 350-363.

Catenacci, M., and Giupponi, C. (2013). “Integrated assessment of sea-level rise adaptation strategies using a Bayesian decision network approach.” *Environmental Modelling & Software*, 44, 87 – 100.

Cavazos, T. (2000). “Using Self-Organizing Maps to Investigate Extreme Climate Events: An Application to Wintertime Precipitation in the Balkans.” *Journal of Climate*, 13(10), 1718 – 1732.

CDC (U.S. Centers for Disease Control and Prevention). (2018). “Compressed mortality file, underlying cause of death.” *CDC WONDER database*. <http://wonder.cdc.gov/mortSQL.html> (Oct. 7, 2018).

Census. (2010). “2010 Census Urban and Rural Classification and Urban Area Criteria.” <https://www.census.gov/geo/reference/ua/urban-rural-2010.html> (Nov. 3, 2016).

Census. (2018). *2016 SUSB Annual Data Tables by Establishment Industry*. <https://www.census.gov/data/tables/2016/econ/susb/2016-susb-annual.html> (May 3, 2019).

Census. (2019). *New Census Bureau Estimates Show Counties in South and West Lead Nation in Population Growth*. < https://www.census.gov/newsroom/press-releases/2019/estimates-county-metro.html#table6 > (May 30, 2019).

Chen, F., Kusaka, H., Bornstein, R., Ching, J., Grimmond, C., Grossman-Clarke, S., Loridan, T., Manning, K. Martilli, A., Miao, S., Sailor, D., Salamanca, F., Taha, H., Tewari, M., Wang, X., Wyszogrodzkia, A., and Zhang, C. (2011). “The integrated WRF/urban modelling system: development, evaluation, and applications to urban environmental problems.” *Int. J. Climatol.*, 31, 273–288.

Chen, J., Brissette, F.P., and Leconte, R. (2012). “Coupling statistical and dynamical methods for spatial downscaling of precipitation.” Clim. Change, 114 (3), 509–526.

Cowan, T., Purich, A., Perkins, S., Pezza, A., Boschat, G., and Sadler, K. (2014). “More frequent, longer, and hotter heat waves for Australia in the twenty-first century.” J.Clim., 27 (15), 5851–5871.

Dai, A. G., Rasmussen, R. M., Ikeda, K., and Liu, C. H. (2017). “A new approach to construct representative future forcing data for dynamic downscaling.” *Clim Dyn*, 43, 1 – 9.

DCOZ (DC Office of Zoning). (2016). “Zoning Regulations of 2016 Development Standards.” <https://dcoz.dc.gov/page/summary-zone-districts> (Oct. 26, 2018).

Dee, D. P., Balmaseda, M., Balsamo, G., Engelen, R., Simmons, A. J., and Thépaut, J. N. (2014). “Toward a Consistent Reanalysis of the Climate System.” *Bull. Amer. Meteor. Soc.*, 95, 1235–1248.

Dettinger, M.D., Cayan, D.R., Meyer, M.K., and Jeton, A.E. (2004). “Simulated hydrologic responses to climate variations and change in the Merced, Carson, and American river basins, Sierra Nevada, California, 1900-2099.” Clim. Change, 62, 283–317.

Diffenbaugh, N. S., Jeremy S. P., Trapp, R. J., and Giorgi, F. (2005). “Fine-scale processes regulate the response of extreme events to global climate change.” Proc. Natl. Acad. Sci., 102, 44, 15774–15778.

DOE (U.S. Department of Energy). (2013). *U.S. Energy Sector Vulnerabilities to Climate Change and Extreme Weather*. < https://www.energy.gov/sites/prod/files/2013/07/f2/20130716-Energy%20Sector%20Vulnerabilities%20Report.pdf > (May 20, 2019).

DOEE (Department of Energy and Environment). (2013). “Sustainable DC Plan.” <http://www.sustainabledc.org/about/sustainable-dc-plan/> (Dec. 30, 2018).

DOEE (U.S. Department of Energy and Environment). (2016). *Climate Ready DC*. < https://doee.dc.gov/sites/default/files/dc/sites/ddoe/service_content/attachments/CRDC-Report-FINAL-Web.pdf> (Jan. 5, 2019).

DOEE (U.S. Department of Energy and Environment). (2018). *Clean Energy DC– The District of Columbia Climate and Energy Action Plan* < https://doee.dc.gov/sites/default/files/dc/sites/ddoe/page_content/attachments/Clean%20Energy%20DC%20-%20Full%20Report_0.pdf> (Jan. 5, 2019).

Dole, R., Hoerling, M., Perlwitz, J., Eischeid, J., Pegion, P., Zhang, T., Quan, X., Xu, T., and Murray, D. (2011). “Was there a basis for anticipating the 2010 Russian heat wave?” Geophys. Res. Lett., 38, L06702.

Ebi, K.L., Helmer, M., and Vainio, J. (2008). “The health impacts of climate change: getting started on a new theme.” Prehosp. Disaster Med., 23(4), 60–64.

EIA (U.S. Energy Information Administration). (2019a). *Annual Energy Outlook 2019 with projections to 2050*. Report, U.S. Energy Information Administration Office of Energy Analysis, U.S. Department of Energy, Washington, DC.

EIA (U.S. Energy Information Administration). (2019b). *State Profile and Energy Estimates*. <https://www.eia.gov/state/?sid=DC> (Feb. 10, 2019).

EIA (U.S. Energy Information Administration). (2019c). *Hourly information on U.S. electricity supply, demand, and flows*. < https://www.eia.gov/todayinenergy/detail.php?id=27212> (Jan. 30, 2019).

Elsner, J. B., and Schmertmann, C. P. (1994). “Assessing forecast skill through cross validation.” Weather and Forecasting, 9, 619–624.

EPA (U.S. Environmental Protection Agency). (2018). *Emission Factors for Greenhouse Gas Inventories*. < https://www.epa.gov/sites/production/files/2018-03/documents/emission-factors_mar_2018_0.pdf> (May 10, 2019).

EPA (U.S. Environmental Protection Agency). (2019). *The Social Cost of Carbon*. < https://19january2017snapshot.epa.gov/climatechange/social-cost-carbon_.html> (May 10, 2019).

Eyring, V., Bony, S., Meehl, G. A., Senior, C. A., Stevens, B., Stouffer, R. J. and Taylor, K. E. (2016). "Overview of the Coupled Model Intercomparison Project Phase 6 (CMIP6) experimental design and organization." *Geosci. Model Dev.*, 9, 1937 – 1958.

Filleul, L., Cassadou, S., Médina, S., Fabres, P., Lefranc, A., Eilstein, D., Le Tertre, A., Pascal, L., Chardon, B., Blanchard, M., Declercq, C., Jusot, J. F., Prouvost, H., and Ledrans, M. (2006). "The Relation Between Temperature, Ozone, and Mortality in Nine French Cities During the Heat Wave of 2003." Environmental Health Perspectives, 114(9), 1344 – 1347.

Fischer, E. M., and Schär, C. (2010). "Consistent geographical patterns of changes in high-impact European heat waves." *Nat. Geosci.*, 3, 398–403.

Frich, P., Alexander, L.V., Della-Marta, P., Gleason, B., Haylock, M., Klein Tank, A.M.G., and Peterson, T. (2002). "Observed coherent changes in climatic extremes during the second half of the twentieth century." Clim. Research, 19, 193–212.

Fussel, H. M. (2007). "Adaptation planning for climate change: concepts, assessment approaches, and key lessons." *Sustainability Science*, 2(2), 265–275.

Gagnon, P., Margolis, R., Melius, J., Phillips, C., and Elmore, R. (2016). *Rooftop Solar Photovoltaic Technical Potential in the United States: A Detailed Assessment*. Report, National Renewable Energy Laboratory, U.S. Department of Energy, Office of Scientific and Technical Information, Oak Ridge, TN.

Gao, Y., Fu, J. S., Drake, J. B., Liu, Y., and Lamarque, J. F. (2012). "Projected changes of extreme weather events in the eastern United States based on a high resolution climate modeling system." *Environ. Res. Lett.*, 7, 044025.

González-Díaz, A., Alcaráz-Calderón, A. M., González-Díaz, M. O., Méndez-Aranda, A., Lucquiaud, M., González-Santaló, J. M. (2017). "Effect of the ambient conditions on gas turbine combined cycle power plants with post-combustion CO2 capture." *Energy*, 134, 221-233.

GRHC (Green Roofs for Healthy Cities). (2018). *2017 Green Roof Industry Survey*. <https://static1.squarespace.com/static/588221e420099e47b8fe06d8/t/5b58831170a6ad8cadd146d6/1532527379537/2017_Green_Roof_Market_Survey_Results_Media_Release.pdf> (March 30, 2019)

Grize, L., Huss, A., Thommen, O., Schindler, C. and Braun-Fahrländer, C. (2005). "Heat wave 2003 and mortality in Switzerland." Swiss Medical Weekly, 135, 200–205.

Gudmundsson, L., Bremnes, J. B., Haugen, J. E., and Engen-Skaugen, T. (2012). "Technical Note: Downscaling RCM precipitation to the station scale using statistical transformations – a comparison of methods.” Hydrol. Earth Syst. Sci., 16, 3383–3390.

Habeeb, D., Vargo, J., and Stone, B. (2015). “Rising heat wave trends in large US cities.” *Nat. Hazards*, 76, 1651–1665.

Hayhoe, K., VanDorn, J., Croley, T.C., Schlegal, N., and Wuebbles, D. (2010). “Regional climate change projections for Chicago and the US Great Lakes.” J. Great Lakes Res., 36, 7–21.

Hayhoe, K., Wake, C., Anderson, B., Liang, X., Maurer, E., Zhu, J., Bradbury, J., DeGaetano, A., Stoner, A. M., and Wuebbles, D. (2008). “Regional Climate Change Projections for the Northeast USA.” Mitigation and Adaptation Strategies for Global Change, 13, 425-436.

Homer, C.G., Dewitz, J.A., Yang, L., Jin, S., Danielson, P., Xian, G., Coulston, J., Herold, N.D., Wickham, J.D., and Megown, K. (2015). *Photogrammetric Engineering and Remote Sensing*, 81(5), 345-354.

Hsu, D., O’Donoughue, P., Fthenakis, V., Heath, G., Kim, H., Sawyer, P., Choi, J., and Turney, D. (2012). “Life Cycle Greenhouse Gas Emissions of Crystalline Silicon Photovoltaic Electricity Generation: Systematic Review and Harmonization.” *Journal of Industrial Ecology*, 16(S1), S122-S135.

Huth, R., Kysely, J., and Pokorna, L. (2000). “A GCM Simulation of Heat waves, Dry Spells, and Their Relationships to Circulation.” Clim. Change, 46, 29–60.

IPCC (Intergovernmental Panel on Climate Change). (2013). *Climate Change 2013, the Physical Science Basis*. Working Group I, Cambridge University Press, London.

IPCC (Intergovernmental Panel on Climate Change). (2014). Impacts, Adaptation, and Vulnerability: Summary for Policy Makers, Working Group II, Cambridge University Press, London.

Irfan, U., Barclay, E., and Sukumar, K. (2019). *Weather 2050.* <https://www.vox.com/a/weather-climate-change-us-cities-global-warming> (July 30, 2019).

Jaffal, I., Ouldboukhitine, S. E., and Belarbi, R. (2012). "A comprehensive study of the impact of green roofs on building energy performance." *Renewable Energy,* 43, 157–164.

Jendritzky, G., and Tinz, B. (2009). "The thermal environment of the human being on the global scale." Global Health Action, 2, 10–21.

Jin, M., and Dickinson, R.E. (2010). "Land surface skin temperature climatology: benefitting from the strengths of satellite observations." *Environ. Res. Lett*. 5, 044004.

Jones, P. G., and Thornton, P.K. (2013). "Generating downscaled weather data from a suite of climate models for agricultural modelling applications." *Agricultural Systems*, 114, 1 – 5.

Jordan, D. C. and Kurtz, S. R. (2013). "Photovoltaic Degradation Rates — An Analytical Review." *Prog. Photovoltaics,* 21, 12–29.

Kalisa, E., Fadlallah, S., Amani, M., Nahayo, L., and Habiyaremye, G. (2018). "Temperature and air pollution relationship during heatwaves in Birmingham, UK." Sustainable Cities and Society, 43, 111 – 120.

Kalnay, E., and Cai, M. (2003). “Impact of urbanization and land-use change on climate.” *Nature*, 423, 528-531.

Kats, G., and Glassbrook, K. (2016). *Achieving Urban Resilience: Washington DC.* <https://www.coolrooftoolkit.org/wp-content/uploads/2016/12/Kats-SmartsurfacesDC-FullReport.pdf> (April 10, 2019).

Kavlak, G., McNerney, J. and Trancik, J. E. (2018). “Evaluating the causes of cost reduction in photovoltaic modules.” *Energy Policy*, 123, 700–710.

Kehlhofer, P., Hannemann, F., Stirninmann, F., and Rukes, B. (2009). *Combined-cycle gas and steam turbine power plant (3rd edition)*. PennWell Corporation, Tulsa, OK.

Keith, D., Geetha, R., Tord, K., Carol, S., and Ivan, H. (2005). “Effects of Temperature and Ozone on Daily Mortality During the August 2003 Heat Wave in France.” Archives of Environmental & Occupational Health, 60(4), 205 – 212.

Kenward, A., Yawitz, D., Sanford, T., and Wang, R. (2014). *Summer in the City: Hot and Getting Hotter*. Report, Climate Central, Princeton, NJ.

Kharin, V. V., and Zwiers, F.W. (2002). "Climate predictions with multimodel ensembles." J. Climate, 15 (7), 793-799.

Kilsby, C.G., Jones, P.D., Burton, A., Ford, A.C, Fowler, H.J., Harpman, C., James, P., Smith, A. and Wilby, R.L. (2007). “A daily weather generator for use in climate change studies.” *Environmental Modelling and Software,* 22, 1705 – 1719.

Kim, Y., and Baik, J. (2005). “Spatial and temporal structure of the urban heat island in Seoul.” J. Appl. Meteorol., 44, 591–605.

Kochanek, K. D., Xu, J., Murphy, S. L., Minino, A. M., and Kung, H. C. (2012). “Deaths: Final data for 2009.” National Vital Statistics Reports, 60 (3), 1–117.

Kolokotroni, M., Ren, X., Davies, M., and Mavrogianni, A. (2012). “London’s urban heat island: Impact on current and future energy consumption in office buildings.” Energy Build., 47, 302–311.

Komurcu, M., Emanuel, K. A., Huber, M., and Acosta, R. P. (2018). “High-Resolution Climate Projections for the Northeastern United States Using Dynamical Downscaling at Convection-Permitting Scales.” *Earth Space Sci.*, 5, 801-826.

Konopacki, S., and Akbari, H., (2002). Energy savings for heat island reduction strategies in Chicago and Houston (including updates for Baton Rouge, Sacramento, and Salt Lake City), Final Report, LBNL-49638, University of California, Berkeley, CA.

Krayenhoff, E. S., Moustaoui, M., Broadbent, A. M., Gupta, V., and Georgescu, M. (2018). “Diurnal interaction between urban expansion, climate change and adaptation in US cities.” *Nature Clim. Change*, 8, 1097-1103.

Kunkel, K. E., Liang, X. Z., and Zhu, J. (2010). “Regional Climate Model Projections and Uncertainties of U.S. Summer Heat Waves.” *Journal of Climate*, 23, 4447–4458.

Kusaka, H., Kondo, H., Kikegawa, Y., and Kimura, F. (2001). “A Simple Single-Layer Urban Canopy Model for Atmospheric Models: Comparison with Multi-Layer and Slab Models.” *Boundary-Layer Meteorology*, 101, 329–358.

Laaidi, K., Zeghnoun, A., Dousset, B., Bretin, P., Vandentorren, S., Giraudet, E., and Beaudeau, P. (2012). “The Impact of Heat Islands on Mortality in Paris during the August 2003 Heat Wave.” *Environmental Health Perspectives*, 120(2), 254–259.

Larsen, P.H. Boehlert, B. J. Hamachi-LaCommare, Eto, Martinich, K. Rennels, J. L. (2018). “Projecting future costs to U.S. electric utility customers from power interruptions.” *Energy*, 147, 1256–1277.

Larsen, P.H. Boehlert, B. J. Hamachi-LaCommare, Eto, Martinich, K. Rennels, J. L. (2018). “Projecting future costs to U.S. electric utility customers from power interruptions.” *Energy*, 147, 1256–1277.

Lau, N., and Jo Nath, M. (2012). “A Model Study of Heat Waves over North America: Meteorological Aspects and Projections for the Twenty-First Century.” J. Clim., 25, 4761–4784.

Leung, L.R., and Gustafson, WI. Jr. (2005). “Potential regional climate and implications to U.S. air quality.” Geophys. Res. Lett., 32, L16711.

Li, D., and Bou-Zeid, E. (2013). “Synergistic Interactions between Urban Heat Islands and Heat Waves: The Impact in Cities Is Larger than the Sum of Its Parts.” *J. Appl. Meteorol. Climatol.*, 52, 2051–2064.

Li, D., and Bou-Zeid, E. (2014). “Quality and sensitivity of high-resolution numerical simulation of urban heat islands.” *Environ. Res. Lett.*, 9, 055001.

Li, D., Bou-Zeid, E., and Oppenheimer, M. (2014). “The effectiveness of cool and green roofs as Urban heat island mitigation strategies.” *Environ. Res. Lett.*, 9, 055002.

Li, X., Mazur, R., Allen, D., and Swatek, D. (2005). “Specifying transformer winter and summer peak-load limits.” *IEEE Transactions on Power Delivery*, 20, 185–190.

LLNL (Lawrence Livermore National Laboratory). (2016). “Downscaled CMIP3 and CMIP5 Climate and Hydrology Projections.” <http://gdodcp.ucllnl.org/downscaled_cmip_projections/dcpInterface.html#Projections:%20Complete%20Archives> (Sep 30, 2016).

Lombardo, F. T., and Ayyub, B. M. (2015). “Analysis of Washington, DC, Wind and Temperature Extremes with Examination of Climate Change for Engineering Applications.” *ASCE-ASME J. Risk Uncertainty Eng. Syst., Part A: Civ. Eng.*, 04014005.

Magee, N., Curtis, J., and Wendler. G. (1999). “The urban heat island effect at Fairbanks, Alaska.” Theor. Appl. Climatol., 64, 39–47.

Maloney, E. D., Camargo, S. J., Chang, E., Colle, B., Fu, R., Geil, K. L., Hu, Q., Jinag, X., Johnson, N., Karnauskas, K. B., and Kinter, J., Kirtman, B., Kumar, S., Langenbrunner, B., Lombardo, K., Long, L. N., Mariotti, A., Meyerson, J., E., Mo, K. C., Neelin, J. D., Pan, Z., Seager, R., Serra, Y., Seth, A., Sheffield, J., Stroeve, J., Thibeault, J., Xie, S. P., Wang, C., Wyman, B., and Zhao, M. (2014). “North American climate in CMIP5 experiments: Part III: Assessment of twenty-first-century projections.” J. Clim., 27 (6), 2230–2270.

Martilli, A., Clarke, S.G, Tewari, M., and Manning, K.W. (2009). *Description of the Modifications Made in WRF.3.1 and Short User's Manual of BEP*. National Center for Atmospheric Research, Boulder, CO.

Matzarakis, A., and Amelung, B. (2008). "Physiological equivalent temperature as indicator for impacts of climate change on thermal comfort of humans." Adv. Global Change Res., 30, 161–172.

Maulbetsch, J. S., and DiFilippo, M. N. (2006). *Cost and Value of Water Use at Combined-Cycle Power Plants.* Project report, California Energy Commission, PIER Energy-Related Environmental Research, Sacramento, CA.

McEvoy, D., Ahmed, I., and Mullett, J. (2012). "The impact of the 2009 heat wave on Melbourne's critical infrastructure." Local Environment, 17(8), 783 – 796.

Meehl, G.A., and Tebaldi, C. (2004). "More intense, more frequent, and longer lasting heat waves in the 21st century." *Science*, 305(5686), 994–997.

Memon, R.A, Leung, Y.C., and Liu, C.H. (2008). "A review on the generation, determination and mitigation of urban heat island." J. Environ. Sci., 20, 120–128.

Michaelsen J. (1987). "Cross-validation in statistical climate forecast models." J. Climate Appl. Meteorol., 26, 1589–1600.

Monaghan, A. J., Steinhoff, D. F., Bruyere, C. L., and Yates, D. (2014). "NCAR CESM Global Bias-Corrected CMIP5 Output to Support WRF/MPAS Research." *National Center for Atmospheric Research, Computational and Information Systems Laboratory*. <

https://rda.ucar.edu/datasets/ds316.1/index.html#metadata/detailed.html?_do=y> (Oct. 1, 2017).

Monteiro, A., Carvalho,V., Oliveira, T., and Sousa, C. (2013). “Excess mortality and morbidity during the July 2006 heat wave in Porto. Portugal.” Int. J. Biometeorol., 57, 155–167.

Munaretto, S., Siciliano, G., and Turvani, M. E. (2014). “Integrating adaptive governance and participatory multicriteria methods: a framework for climate adaptation governance.” *Ecology and Society*, 19(2): 74.

National Research Council of the National Academies. (2012). Chapter 3: Strategies for Developing Climate Models: Model Hierarchy, Resolution, and Complexity. In *A National Strategy for Advancing Climate Modeling*. The National Academies Press, Washington DC.

NCAR (National Center for Atmospheric Research). (2017). “ARW Version 3 Modeling System User’s Guide.” *Mesoscale & Microscale Meteorology Division* <http://www2.mmm.ucar.edu/wrf/users/docs/user_guide_V3/contents.html> (Oct. 1, 2017).

NERC (North American Electric Reliability Corporation). (2018). *2018 Summer Reliability Assessment.* <https://www.nerc.com/pa/RAPA/ra/Reliability%20Assessments%20DL/NERC_SRA_05252018_Final.pdf > (April 22, 2019).

NOAA (National Oceanic and Atmospheric Administration). (2017). “Data Tools: Find a Station.” *National Center for Environmental Information,* <http://www.ncdc.noaa.gov/cdo-web/datatools/findstation> (May. 30, 2017).

NOAA (National Oceanic and Atmospheric Administration). (2019). *Degree Day Outlook for Major United States Cities*. < https://www.cpc.ncep.noaa.gov/pacdir/DDdir/INT1.html > (June 1, 2019).

NREL (National Renewable Energy Laboratory). (2012). *Life Cycle Greenhouse Gas Emissions from Solar Photovoltaics*. <https://www.nrel.gov/docs/fy13osti/56487.pdf> (June 30, 2019).

NWS (National Weather Service). (1994). Excessive heat watch, warning and advisory heat index criteria, Regional Operations Manual Letter E-5-94, Eastern Region, NWS, Bohemia, NY.

NWS (National Weather Service). (1995). Natural disaster survey report: July 1995 heat wave. National Oceanic and Atmospheric Administration, NWS, Washington, DC.

NWS (National Weather Service). (2016). “Heat index.” <http://www.srh.noaa.gov/jetstream/global/hi.html> (Dec.30, 2016).

Ortiz, L. E., González, J. E., Horton, R., Lin, W., Wu, W., Ramamurthy, P., Arend, M., and Bornstein, R. D. (2019). “High-resolution projections of extreme heat in New York City.” *Int. J. Clmatol.* 2019, 1–15.

Osborne, A., and McKeown, C. (2009). Inquiry into the factors leading to and causes of failure in the provision of metropolitan and V/Line train services. Select Committee on Train Services, Melbourne, Australia.

PCMDI (Program for Climate Model Diagnosis and Intercomparison). (2016). “CMIP5 Coupled Model Intercomparison Project.” < http://cmip-pcmdi.llnl.gov/cmip5/availability.html > (Feb. 8, 2017).

Perkins, S.E., and Alexander, L.V. (2012). “On the Measurement of Heat Waves.” J. Clim., 26, 4500–4517.

Phillips, C., and Melius, J. (2016). *U.S. PV-Suitable Rooftop Resources*. < https://www.osti.gov/biblio/1258436 > (May 4, 2019).

Pierce, D. W., Barnett, T. P., Santer, B. D. and Gleckler, P. J. (2009). “Selecting climate models for regional climate change studies.” Proc. Natl. Acad. Sci., 106, 8441–8446.

PJM. (2017). *2017 PJM Reserve Requirement Study*. < https://www.pjm.com/-/media/committees-groups/committees/pc/20171012/20171012-item-03a-2017-pjm-reserve-requirement-study.ashx> (April 10, 2019).

Pu, X., Wang, T. J., Huang, X., Melas, D., Zanis, P., Papanastasiou, D. K., and Poupkou, A. (2017). “Enhanced surface ozone during the heat wave of 2013 in Yangtze River Delta region, China.” Science of The Total Environment, 603–604(15), 807 – 816.

Qin, Y. (2015). “Urban canyon albedo and its implication on the use of reflective cool pavements.” *Energy and Building*, 96, 86–94.

Riahi, K., Rao, S., Krey, V. Cho, C., Chirkov, V., Fischer, G., Kindermann, G., Nakicenovic, N., and Rafaj, P. (2011). “RCP 8.5—A scenario of comparatively high greenhouse gas emissions.” Clim. Change, 109, 33–57.

Riahi, K., van Vuuren, D. P., Kriegler, E., …, and Tavoni, M. (2017). “The Shared Socioeconomic Pathways and their energy, land use, and greenhouse gas emissions implications: An overview.” *Global Environmental Change*, 42, 153 – 168.

Richardson, C.W., and Wright, D.A. (1984). *WGEN: A Model for Generating Daily Weather Variables*. US Dept. of Agriculture, 83, AR5e8.

Robinson, P. J. (2001). “On the Definition of a Heat Wave.” *J. Appl. Meteorol.*, 40, 762–774.

Romeo, C. and Zinzi, M. (2013). “Impact of a cool roof application on the energy and comfort performance in an existing non-residential building. A Sicilian case study.” *Energy and Buildings*, 67, 647–657.

Russo, S., Dosio, A., Graversen, R. G., Sillmann, J., Carrao, H., Dunbar, M. B., Singleton, A., Montagna, P., Barbola, P., and Vogt, J. V. (2014). “Magnitude of extreme heat waves in present climate and their projection in a warming world.” *Journal of Geography Research: Atmosphere,* 119, 12500–12512.

Sanderson, B. M., Wehner, M., and Knutti, R. (2017). “Skill and independence weighting for multi-model assessments.” *Geosci. Model Dev.*, 10, 2379–2395.

Santamouris, M. (2014a). “Cooling the cities – A review of reflective and green roof mitigation technologies to fight heat island and improve comfort in urban environments.” *Solar Energy*, 103, 682–703.

Santamouris, M. (2014b). “On the energy impact of urban heat island and global warming on buildings.” *Energy and Buildings*, 82, 100 – 113.

Santamouris, M., Cartalis, C., Synnefa, A., and Kolokotsa, D. (2015). "On the impact of urban heat island and global warming on the power demand and electricity consumption of buildings—A review." *Energy and Buildings,* 98, 119–124.

Santamouris, M., Papanikolaou, N., Livada, I., Koronakis, I., Georgakis, C., Argiriou, A., And Assimakopoulos, D. N. (2001). "On the Impact of Urban Climate on the Energy Consumption of Buildings." *Solar Energy*, 70(3), 201–216.

Santamouris, M., Synnefa, A., and Karlessi, T. (2011). "Using advanced cool materials in the urban built environment to mitigate heat islands and improve thermal comfort conditions." *Solar Energy,* 85, 3085–3102.

Santamourisa, M., Gaitania, N., Spanoua, A., Saliaria, M., Giannopouloua, K., Vasilakopouloua, K., and Kardomateasb, T. (2012). "Using cool paving materials to improve microclimate of urban areas – Design realization and results of the flisvos project." *Building and Environment,* 53, 128–136.

Sarrat, C., Lemonsu, A., Masson, V., and Guedalia, D. (2006). "Impact of urban heat island on regional atmospheric pollution." *Atmospheric Environment,* 40(10), 1743 – 1758.

Sathaye, J. A., Dale, L. L., Larsen, P. H., Fitts, G. A., Koy, K., Lewis, S. M., de Lucena, A. F. P. (2013). "Estimating impacts of warming temperatures on California's electricity system." *Glob. Environ. Change*, 23, 499−511.

Schafer, B., Witthaut, D., Timme, M., and Latora, V. (2018). "Dynamically induced cascading failures in power grids." *Nat. Commun.*, 9, 1975.

Schoetter, R., Cattiaux, J., and Douville, H. (2015). “Changes of western European heat wave characteristics projected by the CMIP5 ensemble.” Clim. Dyn., 45 (5), 1601–1616.

Schwarz, C. (2015). *Green roof energy balances for native grasses and sedum.* Thesis, University of Nebraska, Lincoln, Nebraska.

Scott, A. A., Waugh, D. W., and Zaitchik, B. F. (2018). “Reduced Urban Heat Island intensity under warmer conditions.” *Environmental Research Letters*, 13, 064003.

Semenov, M. (2012). *LARS-WG stochastic weather generator*. Department of Computational and Systems Biology, UK.

Sen, G., Nil, M., Mamur, H., Doğan, H., Karamolla, M., Karacor, M., Kuyucuoğlu, F., Yörükeren, N., and Bhuiyan, M. R. A. (2018). “The effect of ambient temperature on electric power generation in natural gas combined cycle power plant—A case study.” *Energy Report*, 4, 682-690.

Sheffield, J., Barrett, A. P., Colle, B., Fernando, D. N., Fu, R., Geil, K. L., Hu, Q., Kinter, J., Kumar, S., Langenbrunner, B., Lombardo, K., Long, L. N., Maloney, E., Mariotti, A., Meyerson, J. E., Mo, K. C., Neelin, J. D., Nigam, S., Pan, Z., Ren, T., Ruiz-Barradas, A., Serra, Y. L., Seth, A., Thibeault, J. M., Stroeve, J. C., Yang, Z., and Yin, L. (2013a). “North American climate in CMIP5 experiments. Part I: Evaluation of historical simulations of continental and regional climatology.” J. Clim., 26(23), 9209–9245.

Sheffield, J., Camargo, S. J., Fu, R., Hu, Q., Jiang, X., Johnson, N., Karnauskas, K. B., Kim, S. T., Kinter, J., Kumar, S., Langenbrunner, B., Maloney, E., Mariotti, A., Meyerson, J. E., Neelin, J. D., Nigam, S., Pan, Z., Ruiz-Barradas, A., Seager, R., Serra, Y. L., Sun, D. Z., Wang, C., Xie, S. P., Yu, J. Y., Zhang, T., and Zhao, M. (2013b). "North American climate in CMIP5 experiments. Part II: evaluation of historical simulations of intraseasonal to decadal variability." J. Clim., 26(23), 9247–9290.

Sillmann, J., Kharin, V. V., Zwiers, F. W., Zhang, X., and Bronaugh, D. (2013a). "Climate extremes indices in the CMIP5 multi-model ensemble. Part 1: Model evaluation in the present climate." J. Geophys. Res., 118(4), 1716–1733.

Sillmann, J., Kharin, V. V., Zwiers, F. W., Zhang, X., and Bronaugh, D. (2013b). "Climate extremes indices in the CMIP5 multi-model ensemble. Part 2: Future projections." J. Geophys. Res., 118(6), 2473–2493.

Skamarock, W. C., Klemp, J. B., Dudhia, J., Gill, D. O., Barker, D. M., Duda, M. G., Huang, X. Y., Wang, W., and Powers, J. G. (2008). *A Description of the Advanced Research WRF Version 3*. Technical note, National Center for Atmospheric Research, Boulder, CO.

Song, J., Cotilla-Sanchez, E., Ghanavati, G., and Hines, P. D. H. (2016). "Dynamic modeling of cascading failure in power systems." *IEEE Trans. Power Syst.*, 31(2), 1360–1368.

Stewart, M. G., and Deng, X. (2015). "Climate Impact Risks and Climate Adaptation Engineering for Built Infrastructure." ASCE-ASME J. Risk Uncertainty Eng. Syst., Part A: Civ. Eng., 1(1), 04014001.

Stocker, B. D., Roth, R., Joos, F., Spahni, R., Steinacher, M., Zaehle, S., Bouwman, L., and Xu, R. (2013). "Supplementary Information: Multiple greenhouse-gas feedbacks from the land biosphere under future climate change scenarios." Nat. Clim. Change, 3, 666–672.

Stone, B., Vargo, J., and Habbeb, D. (2013). "Managing climate change in cities: Will climate action plans work?" *Landscape and Urban Planning*, 107(3), 263-271.

Stoner, A. M., K., Hayhoe, K., Yang, X. and Wuebbles, D. J. (2013). An asynchronous regional regression model for statistical downscaling of daily climate variables. Int. J. Climatol., 33, 2473–2494.

Sullivan, M. J., Schellenberg, J., and Blundell, M. (2015). *Updated Value of Service Reliability Estimates for Electric Utility Customers in the United States*. Report, Nexant, Inc., San Francisco, CA.

Tan, J., Zheng, Y., Tang, X., Guo, C., Li, L., Song, G., Zhen, X., Yuan, D., Kalkstein, A.J., Li, F., and Chen, H. (2010). "The urban heat island and its impact on heat waves and human health in Shanghai." Int. J. Biometeorol., 54, 75–84.

Taylor, K. E., Stouffer, R. J., and Meehl, G. A. (2012). "An overview of CMIP5 and the experiment design." Bull. Am. Meteorol. Soc., 93, 485–498.

Testa, J., and Krarti, M. (2017). "A review of benefits and limitations of static and switchable cool roof systems." *Renewable and Sustainable Energy Reviews*, 77, 451–460.

Tewari, M., Chen, F., Kusaka, H., Miao, S. (2007). *Coupled WRF/Unified Noah/Urban-Canopy Modeling System*. WRF Documentation, National Center for Atmospheric Research, Boulder, CO.

Themeßl, M. J., Gobiet, A., and Heinrich, G. (2011). “Empirical-statistical downscaling and error correction of regional climate models and its impact on the climate change signal.” Clim. Change, 112 (2), 449–468.

Tsoutsos, T., Frantzeskaki, N., and Gekas, V. (2005). “Environmental impacts from the solar energy technologies.” *Energy Policy*, 33, 289–296.

UNFCCC (United Nations Framework Convention on Climate Change). (2016). *The Paris Agreement.* <https://unfccc.int/process-and-meetings/the-paris-agreement/the-paris-agreement> (July 31, 2019).

United Nations. (1992). Article 1: Definition in United Nations Framework Convention on Climate Change <https://unfccc.int/files/essential_background/background_publications_htmlpdf/application/pdf/conveng.pdf> (July 17, 2019).

USGCRP (U.S. Global Change Research Program). (2014). *Third National Climate Assessment, Climate change impacts in the United States.* Washington DC.

USGCRP (U.S. Global Change Research Program). (2017). “Climate Science Special Report: Fourth National Climate Assessment, Volume I.” < https://science2017.globalchange.gov/> (Dec. 1, 2017).

USGCRP (U.S. Global Change Research Program). (2018). *Fourth National Climate Assessment, Volume I.* Washington, DC.

Velazquez-Lozada, A., Gonzalez, J. E., and Winter, A. (2006). “Urban Heat island effect analysis for San Juan, Puerto Rico.” Atmo. Environ., 40, 1731–1741.

Wang, H., and Chen, Q. (2014). “Impact of climate change heating and cooling energy use in buildings in the United States.” *Energy and Buildings*, 82, 428–436.

White, R. H., and Toumi, R. (2013). “The limitations of bias correcting regional climate model inputs.” *Geophys Res Lett*, 40, 2907 – 2912.

Wilby, R. L. (2003). “Past and projected trends in London’s urban heat island.” Weather, 58, 251-260.

Wilby, R.L., Troni, J., Biot, Y., Tedd, L., Hewitson, B.C., Smith, D.M. and Sutton, R.T. (2009). “A review of climate risk information for adaptation and development planning.” *Int. J. Climatol.*, 29, 1193 – 1215.

Wuebbles, D., Wuebbles, D., Meehl, G., Hayhoe, K., Karl, T. R., Kunkel, K., Santer, B., and Sun, L. (2014). “CMIP5 climate model analyses climate extremes in the United States.” Bull. Am. Meteorol. Soc., 95(4), 571–583.

Xian, G., Homer, C., Dewitz, J., Fry, J., Hossain, N., and Wickham, J. (2011). “The change of impervious surface area between 2001 and 2006 in the conterminous United States.” *Photogrammetric Engineering and Remote Sensing*, 77(8), 758-762.

Xu, T., Sathaye, J., Akbari, H., Garg, V., and Tetali, S. (2012). “Quantifying the direct benefits of cool roofs in an urban setting: Reduced cooling energy use and lowered greenhouse gas emissions.” *Energy and Buildings*, 48, 1–6.

Xu, Z., Han, Y., and Yang, Z. (2019). “Dynamical downscaling of regional climate: A review of methods and limitations.” *Earth Sciences*, 62(2), 365 – 375.

Yin, C. (2011). *Applications of self-organizing maps to statistical downscaling of major regional climate variables*. PhD dissertation, University of Waikato, Hamilton, New Zealand.

Zhang, Y., and Ayyub, B. (2018). “Urban Heat Projections in a Changing Climate: Washington, DC, Case Study.” *ASCE-ASME Journal of Risk and Uncertainty in Engineering Systems, Part A: Civil Engineering*, 4(4): 04018032.

Zhao, L., Oppenheimer, M., Zhu, Q., Baldwin, J. W., Ebi, K. L., Bou-Zeid, E., Guan, K., and Liu, X. (2018). “Interactions between urban heat islands and heat waves.” *Environmental Research Letters*, 13, 034003.

Zhou, Y., and Shepherd, J. M. (2010). “Atlanta’s urban heat island under extreme heat conditions and potential mitigation strategies.” Nat. Hazards, 52, 639–668.

Zuo, J., Pullen, S., Palmer, J., Bennetts, H., Chileshe, N., and Ma, T. (2015). “Impacts of heat waves and corresponding measures: a review.” *J. Cleaner Production*, 92, 1-12.